Università Ca'Foscari Venezia

PhD Degree

in computer science

Final Thesis

In-line industrial computed tomography applications and developments

Supervisor
Ch. Prof. Andrea Albarelli

Graduand
Enrico Ursella
Matricolation number 956372

Academic Year
2019 / 2020

Abstract

The use of computed tomography to scan all objects passing through an industrial production line enables a wide range of practical applications. Over the years there has been a steady increase in demand for automatic non-contact inspection systems in all industrial production lines, applying sensors of various types, particularly camera-based systems. Computed tomography is a non-destructive investigation method that has spread to many industries but only in rare cases has been applied to in-line inspection in production processes. This work deals with the development and improvement of industrial tomography systems applied to the woodworking and food processing industries. Two types of scanners with different characteristics suitable for the two types of applications have been developed. Physical and mathematical reasons leading to artifacts in reconstructions have been analysed and methods for their reduction tested or developed. Some applied methods for automatic analysis of images produced in various applications are also presented. In the case of wood industry, the entire production line can be modified from the information acquired with a CT scanner, in line with the principles of Industry 4.0.

Index

Published papers and patents on the subject

F. Giudiceandrea, E. Ursella and E. Vicario, “A high speed CT scanner for the sawmill industry,” in *Proceedings of the 17th international non destructive testing and evaluation of wood symposium*, 2011.

E. Ursella, F. Giudiceandrea and M. Boschetti, “A Fast and Continuous CT scanner for the optimization of logs in a sawmill,” in *8th Conference on Industrial Computed Tomography*, Wels,Austria, 2018.

S. Giovannini, D. Boschetto, E. Vicario, M. Cossi, M. Busatto, S. Ghidoni and E. Ursella, “Improving knot segmentation using Deep Learning techniques,” in *21st International Nondestructive Testing and Evaluation of Wood Symposium*, Freiburg, Baden-Württemberg, Germany, 2019.

A. Gasparetto, D. Ressi, F. Bergamasco, M. Pistellato, L. Cosmo, M. Boschetti, E. Ursella and A. Albarelli, “Cross-Dataset Data Augmentation for Convolutional Neural Networks Training . Int. Conf. on Pattern Recognition,” in *Int. Conf. on Pattern Recognition, (ICPR2018)*, 2018.

F. Giudiceandrea and E. Ursella, “Method for grading food products able to roll on their outer surface, such as certain fruits and vegetables”. European Patent EP2261643B1, 2014.

E. Ursella and E. Vicario, “Method and apparatus for non-destructive inspection of a log to identify inner zones that are free of bluestain”. European Patent EP3396374B1, 11 09 2019.

A. Rais, E. Ursella, E. Vicario and F. Giudiceandrea, “The use of the first industrial X-ray CT scanner increases the lumber recovery value: case study on visually strength-graded Douglas-fir timber,” *Annals of Forest Science,* vol. 74, p. 28, 2017.

E. Ursella, F. Giudiceandrea and M. Bacher, “Testa di lavorazione per macchina forestale”. Italian requested PatentIT102020000025426, 27 10 2020.

J. M. Leban, B. Kerfriden, F. Longuetaud, F. Mothe, E. Ursella, Jacquin P., F. Giudiceandrea, P. Siat, Daquitaine R., “La tomographie RX, des exemples d'innovations pour les scieries et pour la comptabilité du carbone forestier,” in *8 ièmes journées du GDR 3544 Sciences du BoisAt: ENSTIB, Campus Bois, EPINAL*, 18-21 november 2019 Epinal Franve.

E. Ursella, “Metodo e dispositivo per misurare una o più componenti di moto di un tronco”. Italian Patent IT10201700012024, 16 01 2020.

E. Ursella, E. Vicario and M. Bacher, “Metodo per stabilire una corrispondenza a posteriori tra un pezzo di legno ed un tronco da cui il pezzo di legno era stato ottenuto”. Italian Patent IT102018000003506, 26 03 2020.

F. Giudiceandrea, A. Katsevich and E. Ursella, “A reconstruction algorithm is a key enabling technology for a new ultrafast CT scanner,” *SIAM News,* vol. 49, p. 1–11, 2016.

A. Giudiceandrea, E. Ursella and G. Zane, “Apparecchiatura tomografica industriale e metodo per controllare l’integrità di prodotti industriali”. italian patent request IT102020000019819, 07 08 2020.

J. Peller, J. Ruizendaal, A. Mencarelli, E. Ursella, K. Winkler and H. Helsen, “Detection of Codling Moth Larvae in Apples using X-ray Computed Tomography,” *submitted to Post Harvest Biology and Technology,* 2021.

K. Tschurtchentaler, E. Ursella and D. Bambi, “Metodo e apparato per la formatura di manufatti di polveri”. Italian Patent IT201600093579A1, 22 02 2019.

E. Ursella, “Schermo per raggi X”. Italian Patent IT102018000004206, 20 04 2020.

E. Ursella, M. Boschetti, “Tunnel CT Scanner”. European patent request EP3690429A1, 05 08 2020.

M. Boschetti, S. Faccini, E. Ursella and G. Zane, “Method and apparatus for non-destructive inspection of fruits having an axis of rotational symmetry”. European Patent EP3521812B1, 15 07 2020.

E. Ursella and F. Giudiceandrea, “Metodo e apparecchiatura per l'esecuzione di un esame tomografico di un oggetto”. Italian patent request IT 102019000019454, 21 10 2019.

E. Ursella, “Apparecchiatura e metodo per eseguire una tomografia computerizzata di un oggetto che presenti forma allungata, in particolare tavole di legno”. Italian patent request Patent IT102020000004246, 28 02 2020.

T. Prenn and E. Ursella, “Tomografo computerizzato a tunnel e metodo per l’esecuzione di una tomografia computerizzata di un oggetto”. Italian patent request IT102020000014239, 15 06 2020.

Chapter 1

Introduction

From the moment it was invented, computed tomography (CT) quickly became a technology of great relevance so that it earned its inventors, Godfrey Hounsfield and Allan Cormak, the Nobel Prize. Originally conceived for use in the medical field, it has found applications in very different fields. This thesis presents the work carried out at the company Microtec Srl Gmbh for the research, development and realization of tomographs in a field that was not deeply explored so far: the industrial in-line tomography. It is the result of my work in cooperation of many people in Microtec and other universities, research centers and customers.

1.1 The X-ray computed tomography

The idea of being able to see inside an object as if it was transparent is certainly fascinating. The discovery of X-rays has opened great opportunities in this field but the image produced is only the projection on two dimensions of the scanned object. Through the combination of X-ray projections acquired from different directions, tomographic reconstruction makes it possible to obtain a distinct value for each point of the space being measured. Instead of a two-dimensional image subdivided into rectangles called pixels, we obtain a three-dimensional image subdivided into parallelepipeds called voxels.

In Figure 1.1 it is shown the comparison of the image obtained with an X-ray projection compared to one of the sections of a tomographic reconstruction. The figure shows an example taken from the most classic application, namely that in the medical field, compared to an example of industrial computed tomography applied to a wooden log.

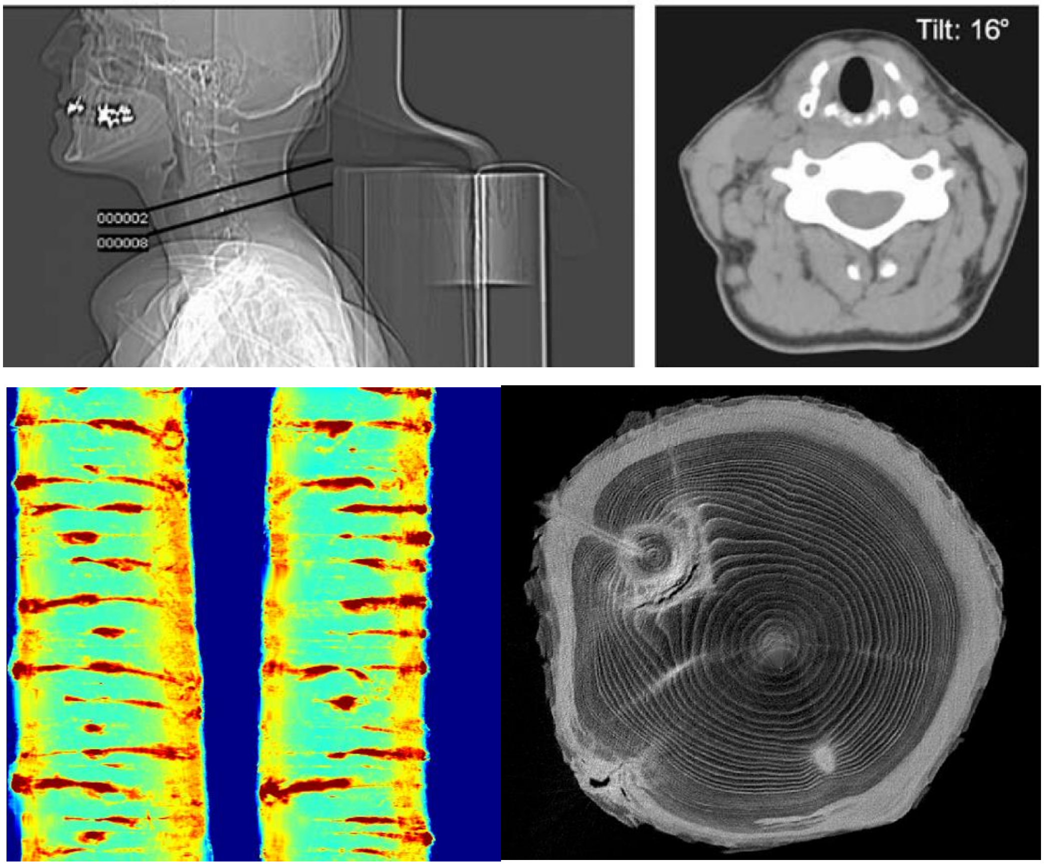

Figure 1.1Comparison of X-ray images (top left) and CT slice (top right) in human body (top) [1]. X-ray scan of a log with Microtec Logeye 302 double view (bottom left) and CT reconstruction with Microtec Mito 500 at Luleå University of Technology (bottom right).

1.2 Applications of X-ray tomography

It is possible to create a tomographic reconstruction from signals measured in different ways, for example magnetic resonance, gamma-ray, ultra-sound, electrical capacitance, electromagnetic induction. In this work I focused on ray tomography because it has the advantage of allowing fast measurements without the need for contact with the object.

The **medical field** has definitely been the one where there has been the greatest diffusion of the technology. The worldwide market for CT scanners in the medical field has been estimated at about $5.53 million [2] and it is the area where there has been the most research. One of the specific requirements of this type of application is the need to reduce as much as possible the X-ray dose received by the patient during the examination. This implies a series of attentions not necessary in other applications, for example that the quality of the sensors must be very high, able to use every single photon that passes through the patient under examination. Another particular feature of medical tomographs is that usually measurement sessions lasting a few seconds are interspersed with breaks of several minutes in which the patient is positioned or leaves the examination area. This allows the use of rotating anode X-ray tubes [1] that can operate at very high currents for a short time, provided they have a long pause time to cool down before further use. Rotating anode tubes are not used in most other application areas where scan times are much longer or even continuous. The maximal speed that can be reached by this type of scanner is typically 16 m/min [3], a typical power of the X-ray tube 100kW.

Figure 1.2 An industrial Microtec Mito 500 CT scanner (left) and a medical CT Siemens Somatom Emotion (right) installed at Luleå University of Technology for scientific use.

The increase in terrorist attacks since 2001 has increased the use of **baggage CT scanners** at airports [4]. These types of tomographs need to work continuously, without the breaks that would allow cooling of the rotating anode. For this reason the currents in the X-ray tubes must be lower, thus images have higher noise. For example the Rapiscan 920 CT has an X-ray tube with the maximal power of 800W an scan speed of 9 m/min [5].

An industrial application of tomography is the **process tomography**. These are mainly applications in which tomography measures fluids during their transport in pipes or during a reaction [6].

In the industrial field the usage of **microtomography** is increasing for metrology verification [7], especially in additive manufacturing [8]. This type of scanners is usually placed near a production line in order to test a limited number of samples. The resolution is higher than other applications but the scan of a sample requires usually many minutes. In order to automatize the process, some scanner is mounted with a robotic arm which loads and unloads the samples from the scanner.

Only few CT scanners are used for **inline application** and verification of 100% of the production [9]. Waygate technologies proposes a solution with a helical scanner on a conveyor belt at a maximum speed of 3.7 m/min [10] .

The aim of this work is the development of scanners that can be used for the analysis of all products on production line with speed up to 100 times faster. Microtec core business is in the production of scanners for the sawmill industry, where a typical speed for a log measurement is 160 m/min and up to 1000 m/min for boards inspection. Another important market for Microtec, with its division Biometic, is the food industry where the speed of the lines is typically between 5 and 60 m/min.

In Figure 1.2 an example of a medical scanner and an industrial scanner installed at Luleå University of Technology.

1.3 Characteristics required for inline CT scanners

As explained previously, the speed of scan is one of the main differences required respect to other type of existing systems. There are many features influencing the speed, among them the power of the X-ray tube, the resolution and the sensitivity of the sensors, the dimension of the sensors, the cone angle, the reconstruction algorithm, the rotational speed of the gantry.

The required speed is between 5 m/min and 1000 m/min depending on the application. In this work I will present two solutions already developed: CT Log for the sawmill industry, that can reach 180 m/min, and Mito at 40 m/min.

The resolution required for the applications considered is lower respect to other application. The biological features developed in a wood log are mainly oriented along the main growth direction, for this reason we evaluated that the target resolution was 10mm in the main direction and 1mm in the other directions. For food application the requests was 0.5mm in every direction.

Many industries work on 3 shifts, so that the production never stops. An industrial scanner has to be able to work in these condition.

The work environment is an important feature for a scanner that have to work in production. Sawmills are often in cold countries where external temperature goes below -30°C and the logs passing through the scanner are dirty and can be wet from rain. In the food industry the devices have to be washable for sanity reason so that in many application the external parts must be waterproof and built with certain materials allowed by law.

In order to produce correct CT reconstructions, the products have to be stable on the conveyor without unwanted movements. This requires special precautions for example when transporting olives or wood logs.

In many applications the tomographic data related to the scanning of an object are first acquired and, in a second step, processed to obtain the tomographic reconstruction. Analysis of the reconstruction can be performed during a further step. In an industrial application it is often necessary that, within few seconds from the passage of the product in the scanner, the measured data is acquired, reconstructed, analysed and decisions are taken for subsequent automations. For example, in asawmill is necessary to control within ten seconds the optimal cut of a log according to its internal characteristics.

1.4 Structure of the thesis

The content of this thesis concerns the development of industrial tomographs by Microtec over the last few decades. The initial idea and all the development started from the founder and current president of Microtec Federico Giudiceandrea. Over the years I have been responsible for the development of tomographs and research at various stages of the company's growth. This thesis presents both the initial developments and the latest versions of image processing and traceability of CT Log, the development of Mito and the new innovative solutions that have been addressed in recent years during my PhD.

In chapter 2, the general principles of tomography will be explained together with some solutions I have adopted to improve the quality of tomographic reconstructions. Chapter 3 will explain CT Log in its operation and application as a tool to improve the production of sawmills. The development of CT Log not only involved the creation of a tomograph with innovative features, but it required researches in different areas. In particular, I had to select and implement the appropriate tomographic reconstruction algorithm (3.2), develop specific computer vision algorithms for the automatic detection of many features (3.3-3.8) and develop methods for the use of biometric data in traceability and cut control (3.10). I demonstrate how a CT scanner is not simply an inspection tool for the quality control, but a disruptive technology that allows to get more value from the raw material (3.9) and change the industrial process in the spirit of Industry 4.0 (3.10).

After the development of CT Log, I considered the development of a CT scanner more flexible and less expensive that could be used in a wider range of applications. For this purpose I started the development a new CT scanner called Mito, presented in chapter 4. The details of the design of Mito are omitted in this thesis but I present the performance measured in the application more exploited so far: the food industry.

In chapter 5, I present some solutions I developed for innovative CT scanners that could be produced in the future and applied in a wider range of industrial processes.

For industrial secrecy reasons, many details of the solutions adopted are not presented in this thesis and I have produced a limited number of scientific publications whose content has been reported in whole or in part in this thesis. On the other hand, many patents have been obtained or are still under evaluation and a brief presentation of many of these has been included in the corresponding chapters.

Chapter 2

CT basics and technology

2.1 Tomographic reconstruction

Tomography is a technique for representing the internal characteristics of a sample in a way that makes it easy to analyse. There are many methods of measuring physical quantities relating to the internal parts of a body, including electrical and sound conduction and transparency to electromagnetic radiation. These measurements provide a signal according to the characteristics of an entire sample area. For example, the measurement of the absorption of a light beam will depend on all parts of the sample interposed between the source and the sensor.

Tomography uses these types of signals to produce images that represent the properties of individual parts of space rather than the whole object. In the same way that a planar image captured by a camera is represented by pixels, the spatially representative image produced by a tomograph is divided into voxels.

From a mathematical point of view, the aim of tomography is to produce a function $f(x)$ representing an area of space of coordinates $x = (X, Y, Z)$ from a series of measurements $p(s)$ that are related to the value of $f(x)$ in a certain area of the body.

In the most common case, the measurement $p(s)$ is simply the integral of the function$f(x)$ along a straight line s:

$$p(s) = \int_s f(x)dx \tag{2.1}$$

The problem of tomographic inversion consists therefore in calculating the function$f(x)$ from the measurements $p(s)$ called projections. The projections are measured at different angles rotating a pair source-sensor around the measured sample, or rotating the sample around an axis between the source and the sensor. This allows to have projections passing through every measured voxel from different directions.

In the paragraph 2.2 I will indicate methods to invert the function (2.1), in the paragraph 2.4 and 2.5 I will treat how to reduce some of the effects due to the fact that the X-ray measurements respect only in first approximation the definition of projection used. The differences between the ideal reconstruction of the space function and the result obtained are called artifacts.

2.2 Tomographic reconstruction algorithms

2.2.1 Parallel beam geometry

The reconstruction algorithm depend on the geometry, which is defined by the line integrals available. The simplest geometry is called parallel beam and is illustrated in Figure 2.1. Each projection consists of a number of integrals computed along parallel lines at different distance from the origin. The different projections are acquired rotating the beams direction respect to the object of an angle α.

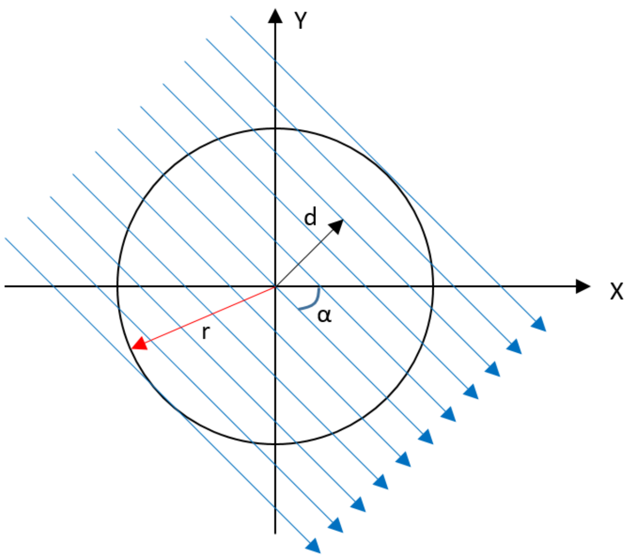

Figure 2.1 Representation of line integrals in a parallel beam tomography. In blue the lines defined by their distance from the origin d and angle α.

The projection can be written as

$$p(d,\alpha) = \int_{-r}^{r} f(t \cdot \cos\alpha - d \cdot sin\alpha\,, t \cdot \sin\alpha + d \cdot cos\alpha)dt \qquad (2.2)$$

The projection is computed with $d \in \{-r, r\}, \alpha \in \{0, \pi\}$. The circle with radius r is called field of view and is the intersection of the areas covered by the line integrals measured at different angles. Most reconstruction algorithms require that the measured object is inside the field of view and no other object affect the projections. This constraint increase the complexity of the scan when the information of a small part of a body is needed and often requires that the structure used to support the scanned sample is included in the field of view.

The Fourier slice theorem gives a simple way to solve the problem ([1]p.163, [11]p. 57). Consider $F(u,v)$ Fourier transform of $f(X,Y)$ and $P_\alpha(w)$ Fourier transform of the projection at angle α. $F(u,0)$ is equal to the Fourier transform of the integral of $f(X,Y)$ along the direction Y. Similarly

$$F(w \cdot sin(\alpha), w \cdot \cos(\alpha)) = P_\alpha(w) \tag{2.3}$$

If a sufficient number of projections are taken, then the function $F(u,v)$ can be assessed in a sufficiently dense amount of points and the inverse Fourier transform can be applied to get the tomographic reconstruction function f(X, Y).

In practice the Fourier slice theorem is not used and techniques based on backprojection are more common. Backprojection is an operation where for each voxel is computed the sum of all the integral lines passing though that voxel. Filtered backprojection (FBP) is based on the backprojection of the projections convolved with a high-pass kernel $k(d)$ [11]:

$$f(X,Y) = \int_0^\pi pk(Ycos\alpha - Xsin\alpha, \alpha)d\alpha \tag{2.4}$$

$$pk(t) \triangleq p(t) * k(t) \tag{2.5}$$

2.2.2 Fan-beam geometry

In X-ray tomography, the beams generated from an X-ray source are not parallel but divergent from a single point. To manage the tomographic reconstruction, a different geometry has to be considered. In Figure 2.2 and on the left side of Figure 2.3 is represented an example of fan-beam geometry. All the beams start from the focal spot (FS) of the source and are directed to a sensor S. The pair source-sensor rotates around the center of rotation O in order to obtain projections at different angles α. The dimension of the sensor defines the fan angle φ, the fan angle and the FS-center distance R defines the radius of the field of view r. Each beam is specified by its angular position on the sensor γ.

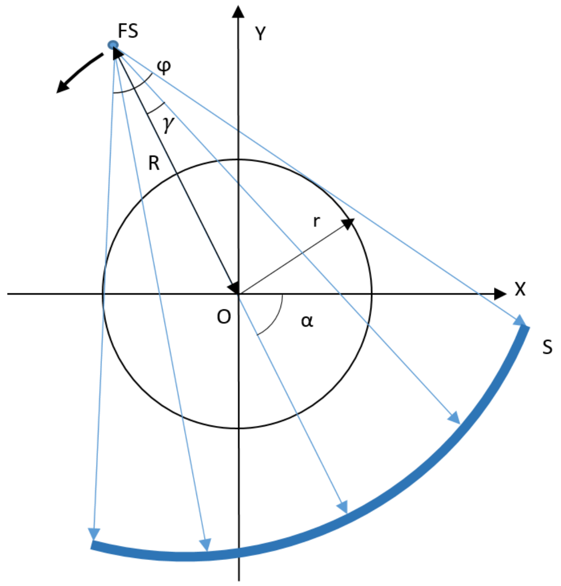

Figure 2.2 Fan beam geometry. The blue arrows indicates the X-ray beams from the focal spot of the generator (FS) to the sensor S.

One common formula for the tomographic inversion in fan-beam geometry is based on FBP [12]:

$$f(X,Y) = \int_0^{2\pi} \frac{R^2}{L(X,Y,\alpha)^2} pf\big(\alpha,\gamma(X,Y,\alpha)\big) d\alpha \tag{2.6}$$

$$L(X,Y,\alpha) \triangleq \sqrt{(R + xcos\alpha + ysin\alpha)^2 + (-xsin\alpha + ycos\alpha)^2)} \tag{2.7}$$

$$pf(\alpha,\gamma) \triangleq (p(\alpha,\gamma) \cdot cos\gamma) * kf(\gamma) \tag{2.8}$$

$$\gamma(X,Y,\alpha) = \arctan \frac{-x \cdot sin\alpha + y \cdot cos\alpha}{R + x \cdot cos\alpha + y \cdot sin\alpha} \tag{2.9}$$

where is $kf(\gamma)$ is an adapt high-pass filter. Different version of a discretized version of the highpass filter $kf(\gamma)$ have been proposed [1]. In formula (2.6) the projections on a whole 2π revolution are required. In reality it is possible to use a reduced number of projections on a rotation on an angle $\pi + \varphi$.

The limit of fan-beam geometry is that it requires more than half revolution for the scan of each slice of the object. In order to have the reconstruction of a volume, after each slice reconstruction the object (or the scanner) must be moved in the Z direction and the measurement of a new slice accomplished. This procedure is very slow and not applicable to inline industrial tomography applications.

2.2.3 Cone-beam geometry

An X-ray source emits beams from the focal spots in different direction, not only on a plane as in fan-beam and the possibility of using projections on a wider volume is at the basis of cone-beam geometry. On the right side of Figure 2.3 is illustrated a cone-beam geometry with a 2D sensor in front of the source. In addition to fan-angle (which is the beam opening in the direction orthogonal to the axis of rotation) cone-beam tomography also includes cone-angle (which is the beam opening in the direction parallel to the axis of rotation).

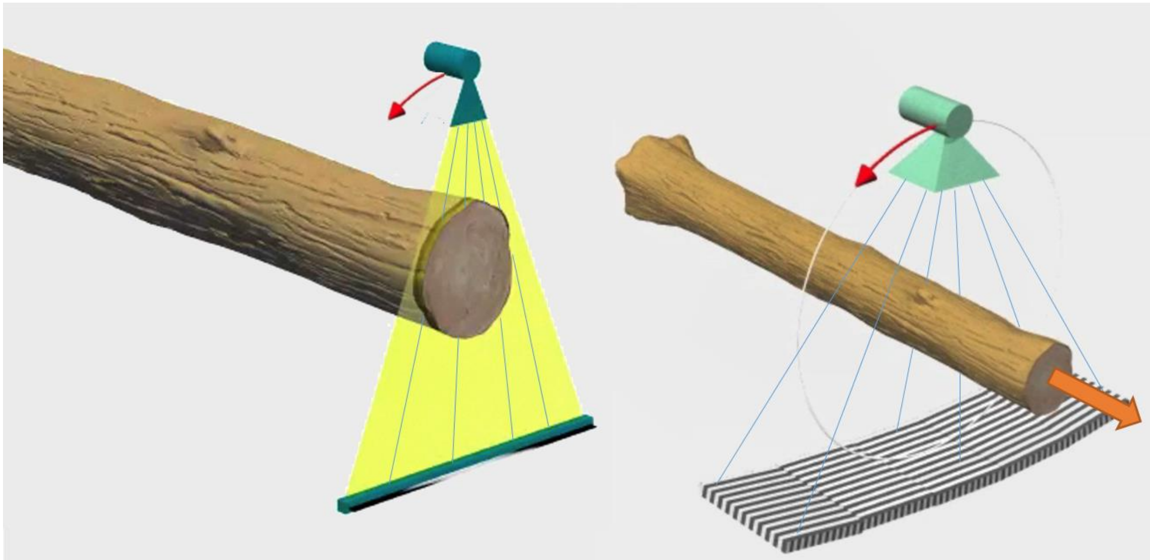

Figure 2.3 On the left picture example of fan-beam geometry: a linear sensor collect only the beam on a plane. On the right picture a cone-beam geometry with a bi-dimensional sensor.

In 1984 Feldkamp, Davis and Kress [13] proposed an approximated solution for FBP cone-beam tomographic inversion, still widely used even if artifacts appear in the reconstruction when the cone angle is wide. In 2002 Katsevich [14] [15] [16] introduced an exact formula for the reconstruction of cone-beam tomography. Other approaches are based on iterative reconstruction [17], mathematical methods that iteratively solve the projection equation. The advantage of iterative methods is the fact that can be applied in a very wide range of trajectories and can reduce the effect of different artifacts. The disadvantage of iterative reconstruction is in the computational cost needed to converge to an accurate solution. In industrial tomography this is a limit because the scan are continuous and the result have to be available quickly after the measurement. In the last years, many proposed algorithms are based on deep learning [18].

There are two main reasons why cone-beam with large cone angle is important for inline industrial tomography. The first reason is the speed of scan. Typically in an inline process the scans are acquired using a helical trajectory. As illustrated in Figure 2.3 right, while the source and the sensor rotate around an axis of rotation, the object moves along a direction parallel to the axis of rotation. This results in a helical trajectory of the source respect to the object. The helical pitch is the movement of the object during one revolution of the source. In order to have a correct reconstruction the helical pitch cannot exceed a certain length dependent on the cone angle of the scanner. As the rotation speed of the sensor is limited by mechanical reasons, the maximum speed of a scanner depends mainly on the helical pitch and thus on the width of the cone angle.

The second reason of the importance of large cone beam in in-line tomography is the efficiency of the source. In X-ray tomography the noise present in the projection images is dependent mainly on the number of photons collected by the sensors. The X-ray sources emit photons on a wide solid angle which is often almost symmetric in the two directions. In order to produce a fan beam or a small cone beam, most of the beams are stopped by a lead shield called collimator. For this reason most of the photons produced are not used and the efficiency of the X-ray source is strongly reduced.

The disadvantages of large cone-beam are the need of bigger sensors and the more complicate reconstruction algorithms. Bigger sensors are more expensive, require the transfer of bigger amount of data and are mechanically more complicate. The complexity of reconstruction is not only related to the need of implementing a more complex algorithm, but also to the need for more computing power and to deal with stronger cone-beam and scatter artifacts. The management of some of these difficulties will be treated in the next chapters.

2.3 X-ray generation and interaction with matter

The most common way to produce X-rays is vacuum tubes. As shown in Figure 2.4, in a vacuum tube the electrons are accelerated to hit a metal anode, typically made of tungsten or molybdenum. The electrons interact with the matter in the anode and 99% of the energy is converted into heat. The remaining 1% is converted in X-ray photons [11].

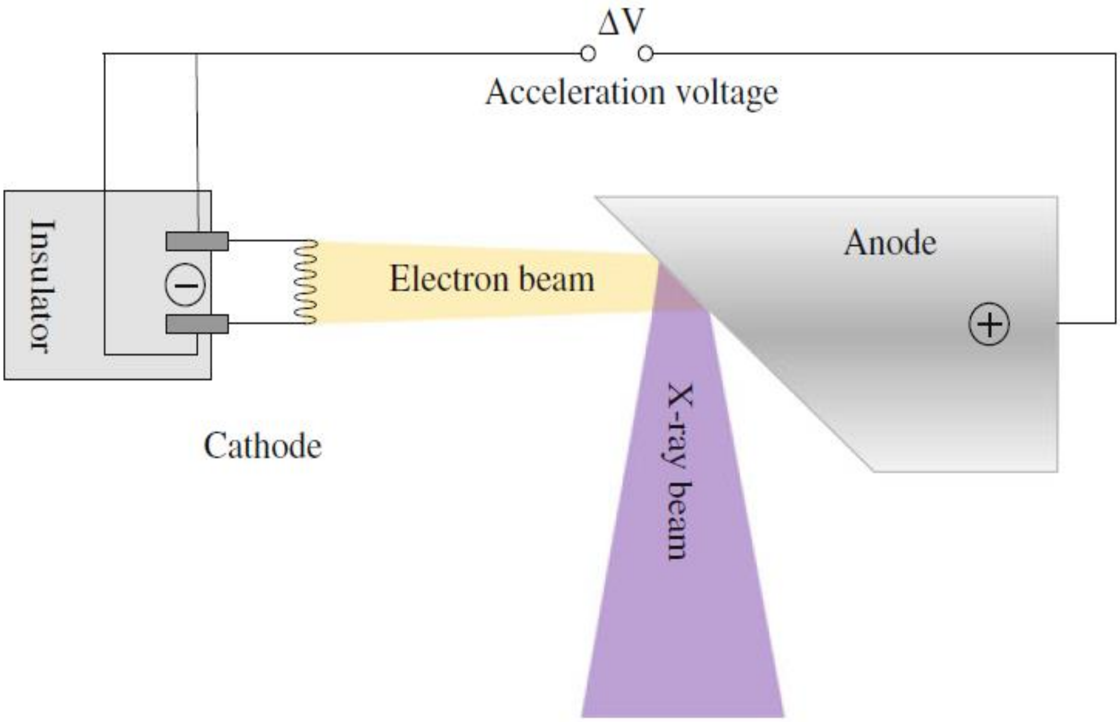

Figure 2.4 Representation of an X-ray tube [11]

In Figure 2.5 it is reported the distribution of the energy of the photons emitted by a tube with different acceleration voltage. The maximal energy of the photons correspond to the acceleration voltage but most of the photons have a lower energy. The number of photons is linearly function of the current passing through the tube and is limited by the ability of the tube to dissipate the heat generated in the anode.

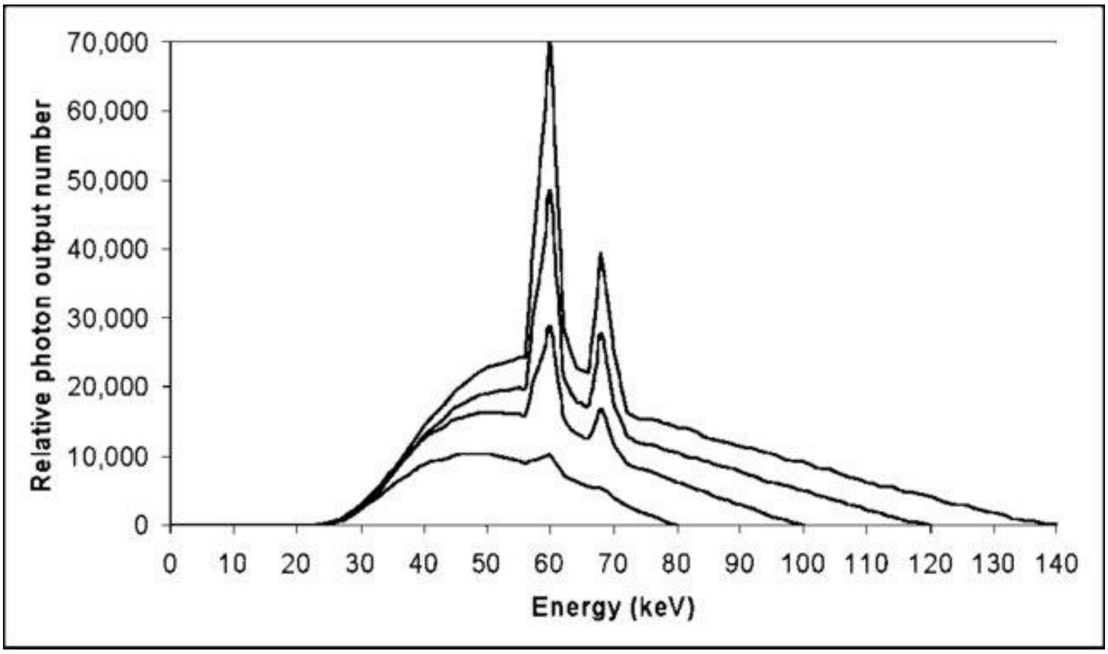

Figure 2.5 Example of typical emission spectra from an X-ray tube [5].

In order to produce images with a good resolution, the electrons have to be focused on a small focal spot so that all X-ray photons are generated almost on the same point. Smaller focal spots mean that the heat is concentrated in a smaller area and is therefore more difficult to dissipate. For this reason, the maximal current in a tube is linearly dependent on the diameter of the focal spot.

When the photons pass through the matter, part of them interact with the matter so that they don't reach the sensor along the original direction. There are multiple possible interactions but they can all be modelled as an attenuation factor that decreases the amount of photons:

$$\frac{dI}{dx} = -\mu(x) \cdot I(x) \tag{2.10}$$

Where x is the position in the space, $I(x)$ is the amount of photons reaching that point, $\mu(x)$ is the attenuation factor of matter in the area. Integrating the differential equation it is possible to obtain the Lambert –Beer law that allows to compute the number of photons reaching the sensor $I(s)$, given the initial number of photons I_o and the attenuation of the matter $\mu(x)$ along the line s between the source and the sensor:

$$I(s) = I_0 \cdot e^{-\int_s \mu(x)dx} \tag{2.11}$$

The attenuation coefficient μ depend on the energy of the photons and the density and composition of the matter.

Another important component of X-ray measurement are the sensors, which convert X-ray photons hitting a specific area in electric signals. In modern applicationa one of the common technology is based on scintillators. Some doped material like Cadmium Tungstanate or Gadolinium emit photons in the visible spectrum when struck by X-ray photons. The visible photons are then detected with photodiodes or other electronic sensors. The signal measured by detectors is dependent on many factors like the area covered, the distance from the source, the efficiency of the scintillator and the photodetector, but in general it is linearly dependent on the number of photons reaching the sensitive area.

In the hypothesis that all the photons have the same energy, equation (2.11) can be used in order to obtain projections according to definition (2.1). I_o can also be seen as the amount of photons reching the sensor when no matter is interposed between the source and the sensor. It is then possible to compute the signal absorption as

$$a(s) \triangleq -\ln\left(\frac{I(s)}{I_0}\right)=\int_s \mu(x)dx \tag{2.12}$$

Where the second part of the equation is derived from (2.11). The possibility of measuring an attenuation $a(s)$, which respects the definition of projection (2.1), allows to apply all the tomographic inversion techniques described in paragraph 2.2.

2.4 Beam hardening artifact correction

In the practical case some of the assumptions required for equation (2.12) are not valid and this fact creates differences in the reconstructed CT image $f(x)$ called artifacts.

In this paragraph I will consider the beam hardening artifacts, which arise because of the multi-energetic nature of the X-ray beams generated by an X-ray tube. In the next paragraph, I will consider the fact that the photons interacting with matter do not disappear but they often simply change energy and direction.

2.4.1 Description of the beam hardening artifact

The attenuation of X-ray photons by different matters is expressed by the attenuation coefficient μ. The attenuation coefficient depends on density, composition of the sample and energy of the photons. For this reason, equation (2.11) requires that the X-ray beam is monochromatic, i.e. all photons have the same energy so that the attenuation coefficient of a point of matter does not depend on the direction of the line integral. For a polychromatic source, i.e. an X-ray source emitting photons with more than one energy, the measured energy becomes:

$$I(s) = \int_{E_{\min}}^{E_{\max}} S(E) \cdot e^{-\int_s \mu(x,E)dx} \, dE \tag{2.13}$$

where E is the photon energy, $S(E)$ is the photon energy spectrum, i.e. the fraction of total energy carried by photons with energy E, and the integral is computed on all energies of photons emitted by the X-ray source. Typical examples of X-ray source spectra can be found in Figure 2.5. We can define I_0 in the same way by removing the effect of attenuation, so that

$$I_0 = \int_{E_{\min}}^{E_{\max}} S(E)\, dE \tag{2.14}$$

then $a(s)$ is no longer equal to the line integral of μ, therefore the tomographic reconstruction cannot give the attenuation coefficient as an output. Lower energy photons are absorbed more than high energy ones. For this reason, photons with different energies are removed in a different fraction from the primary source X-ray beam, and the composition of the X-ray beam at a given point in space depends on the amount of matter passed. This problem is called “beam hardening”, as the resulting photon energy spectrum results “harder” than the primary one, i.e. the average energy of X-rays is shifted towards higher values. It is also worth noticing that beam hardening depends on the specific integral line s due to the effect of material composition and distribution in space.

2.4.2 Attenuation coefficients for polychromatic X-ray beams

It is possible to describe the attenuation properties of a material in terms of its mass attenuation coefficient $\kappa = \mu/\rho$, where ρ is the material density, being then a property of the matter dependent on its chemical composition [1]. In [19] it is possible to find the mass attenuation coefficients of all elemental media, in [20] for many compound and mixtures. Figure 2.6 reports, as an example, the mass attenuation coefficients for carbon and water. In general the mass attenuation coefficient of a mixture or compound can be calculated as the weighted average of the mass attenuation coefficients of the composing atoms weighted by the number of atoms present [21]. For example, the mass attenuation coefficient of water can be obtained as:

$$\kappa_{\mathrm{H_2O}} = \frac{2 \cdot \kappa_{\mathrm{H}} + \kappa_{\mathrm{O}}}{2 + 1} \tag{2.15}$$

where κ_{H} and κ_{O} are the mass attenuation coefficients of hydrogen and oxygen respectively.

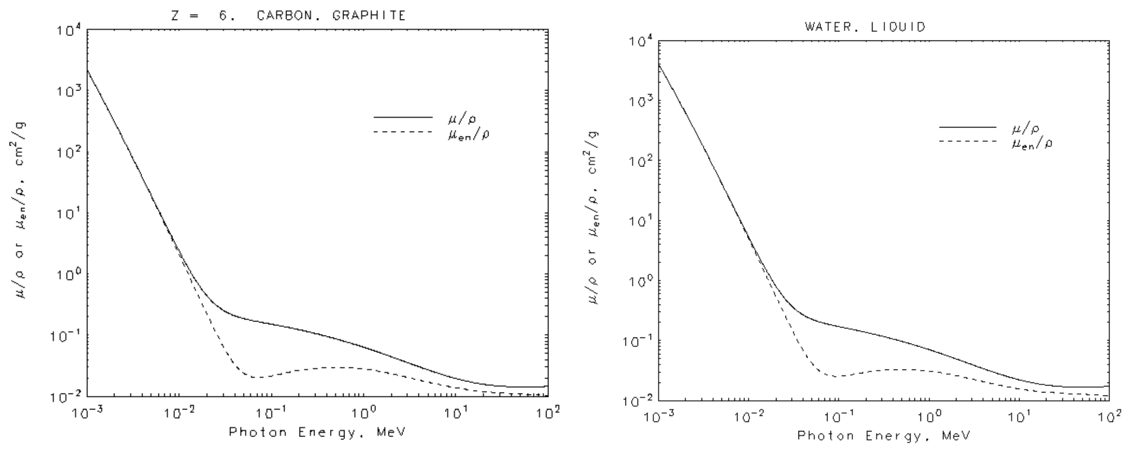

Figure 2.6 Mass attenuation coefficient of carbon (left) and water (right) [19] [20]

2.4.3 Mitigation of beam hardening in tomographic reconstruction

One common way to override the problem of multi-energy equation (2.13) is to introduce a linearization and a total effective linear attenuation coefficient μ_{eff} so that equation (2.13) can be substituted with

$$I(s) = I_0 \cdot e^{-\int_s \mu_{\text{eff}}(x)dx} \tag{2.16}$$

as described in [22] and [23], so that $a(s)$ can be used for a tomographic reconstruction that gives $\mu_{\text{eff}}(x)$ as output. The limitation of this approach is that in reality the linearization done with the introduction of $\mu_{\text{eff}}(x)$ is valid only in certain cases where the amount of mass passed is very small. In other words, it is not possible to associate a unique μ_{eff} to each point in space because the attenuation depends also on the direction of the beam passing through a given volume, and the same volume of the sample can produce different attenuations along different projection lines. Other approaches are presented e.g. in [22].

2.4.4 Beam hardening for constant mass attenuation coefficient

Another possible simplification that can be used is based on the fact that the spectrum of the mass attenuation of many organic compounds are very similar. In Figure 2.7 (right) it is shown that the ratio between the mass attenuation coefficient of water and the mass attenuation coefficient of carbon, cellulose and polyethylene is almost constant in the range 60-200 kV. This observation has no application in medicine, where there are parts like bones containing matter with different attenuation spectrum, but it can have interesting application scanning wood or most of food products.

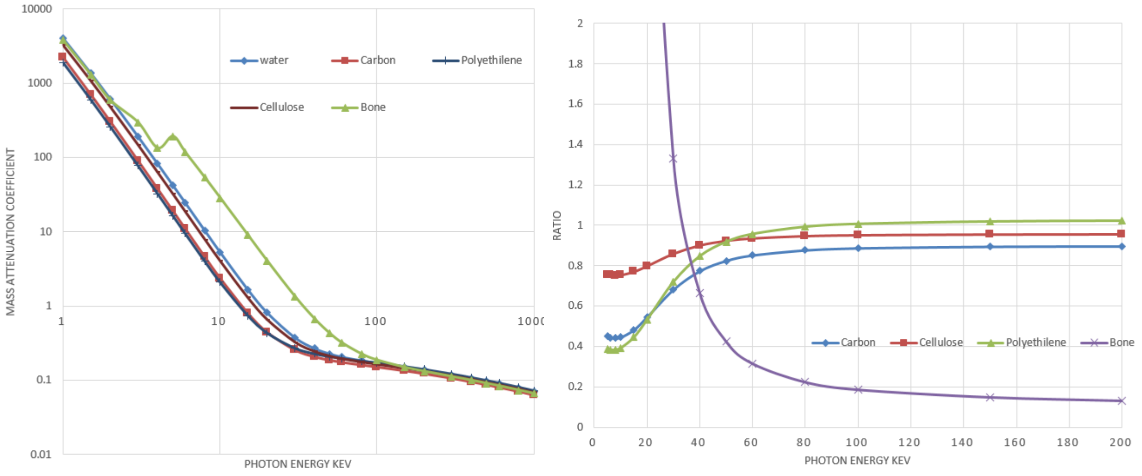

Figure 2.7 . Mass attenuation coefficient of water, carbon, polyethylene and cellulose (left) and ratio respect to water values (right). Computed using data from [20].

Scanning objects containing this type of materials, it is possible to simplify the problem by assuming that all materials have the same mass attenuation coefficient $\kappa(E)$ and are discriminated only by their density $\rho(x)$. With this assumption, equation (4) becomes

$$I(s) = \int_{E_{\min}}^{E_{\max}} S(E) \cdot e^{-\int_s \kappa(E)\rho(x)dx} \, dE \tag{2.17}$$

$$= \int_{E_{\min}}^{E_{\max}} S(E) \cdot e^{-\kappa(E)\int_s \rho(x)dx} \, dE$$

It is then possible to define the mass line integral $p'(s)$, analogously to (1), as

$$p'(s) = \int_s \rho(x)dx \tag{2.18}$$

and to introduce the function

$$B(p') = -\ln\left(\frac{\int S(E) \cdot e^{-\kappa(E)\,p'} dE}{\int S(E)dE}\right) \tag{2.19}$$

Then it is possible to express the signal absorption along a line s as

$$a(s) = -\ln\left(\frac{I(s)}{I_0}\right) = -\ln\left(\frac{\int S(E) \cdot e^{-\kappa(E)\,p'(s)} dE}{\int S(E)dE}\right) = B\big(p'(s)\big) \tag{2.20}$$

where the function $B(p')$ depends only on the energy spectrum of the source and on the mass attenuation coefficient of the measured material, so that it needs to be computed only once for a scanner configuration. Therefore, the function $B(p')$ that maps the mass line integral $p'(s)$ to the absorption $a(s)$ is monotonically increasing, which means it is possible to invert it and compute its inverse function $B^{-1}(a)$, so that $B^{-1}(a) =$

$B^{-1}(B(p')) = p'$ for every $a > 0$. In this way, it is possible to obtain an adjusted absorption $a'(s)$

$$a'(s) = B^{-1}(a(s)) = B^{-1}\left(-\ln\left(\frac{I(s)}{I_0}\right)\right) \tag{2.21}$$

so that a tomographic reconstruction based on $a'(s)$ can be converted into a map of the material density $\rho(x)$, since $a'(s)$ is proportional to $p'(s)$.

In general I showed that it is possible to have a tomographic reconstruction that gives the density of the object if all the objects in the field of view have the similar mass attenuation spectrum and no other artifacts are present (e.g. scatter). For many applications involving water and organic compounds this hypothesis allows to reduce the beam hardening artifact in an efficient way.

2.4.5 Derivation of the beam hardening compensation function

Figure 4 shows a typical behaviour of the function $B(p')$; it can be measured empirically simply measuring the absorption $a(s)$ for different objects with known density integral.

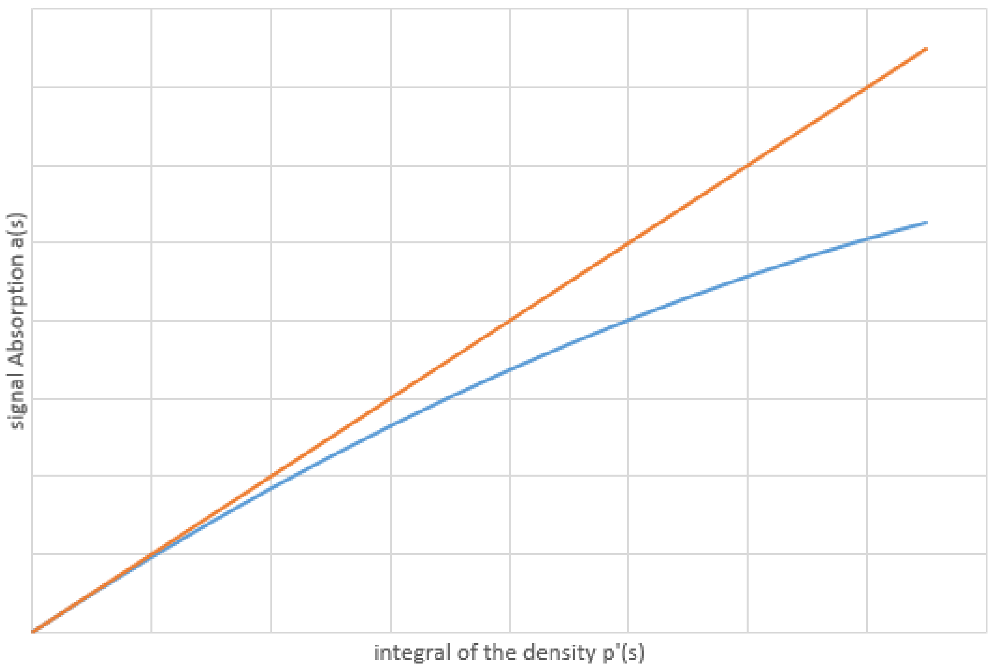

Figure 2.8 Typical trend of the B(p') function shown in blue. The orange line represents the ideal case when no beam hardening arises.

It is possible to approximate the inverse function $B^{-1}(a)$ with a polynomial, which is reduced to a parabola when considering only the first two terms in the Taylor expansion, taking the following form

$$B^{-1}(a) = c_1 \cdot (a + c_2 \cdot a^2) \tag{2.22}$$

Another simpler way to calibrate the parameters is by computing the tomographic reconstruction of an object with constant density and attenuation coefficient, for example a can of water. If the beam hardening correction function B^{-1} is not correct, the reconstructed density map is not uniform, with lower values in the innermost regions of the object volume, resulting in the so-called "cupping" artifact. The parameter c_1 defines the overall resulting density scale and it can be adjusted to assign the average value. The parameter c_2 controls the deviations in the central region of the reconstructed volume: an underestimated value of c_2 results in an underestimated density and vice-versa.

2.5 Scatter artifacts

There can be different types of interaction between X photons and the matter they pass through. As can be seen in Figure 2.9, in the case of photons in the 40kV-3MV range interacting with water, the main phenomenon is Compton scattering: the photon colliding the atom loses energy and its direction is changed depending on its initial energy.

Most tomographic reconstruction algorithms rely on the fact that photons are attenuated as they travel but they are not deflected. The fact that a certain amount of the scattered photons can still reach the sensors creates artifacts in the reconstruction. Different methods were proposed for their reduction [24] [25].

2.5.1 Scanner design for scatter reduction

In order to reduce the effect of the scatter, it is possible to adopt different solutions in the scanner design. All of them are based on the fact that scattered photons can be distinguished from direct photon because of their direction and energy.

A first method to reduce the effects of scatter is to produce as few of them as possible. A scanner that emits a very wide cone of radiation hits a larger area of matter and therefore a greater amount of scatter in proportion to the direct beams. Clearly this method is not feasible in case of high speed scanners where the emission cone must be wide.

A second method consists in placing near the sensors anti-scatter grids, i.e. structures made of thin plates of absorbing material (e.g. lead or tin) positioned parallel to the direction of the direct rays. In this way the direct rays arrive at the sensors without being attenuated while those originating from scatter, which have a different angle of origin, are attenuated while they pass through the lamellas.

A lot of medical scanners use lamellas only along one direction but wide cone scanners require grids capable of stopping photons from both directions.

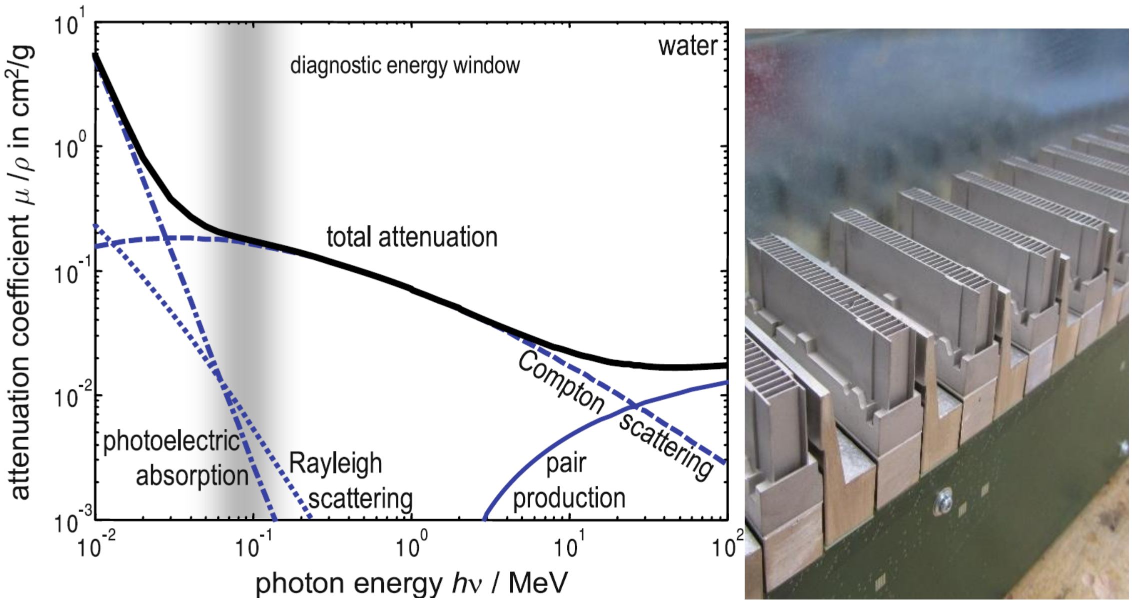

Figure 2.9 distribution of the attenuation coefficient due to different X-ray photon interaction with water [1](left) . Example of Microtec anti-scatter grid prototype (right).

Other methods rely on the possibility of placing the sensor at high distance from the scanned object or placing a sheet of aluminium in front of the sensor in order to absorb the scattered photons which have lower energy respect to the direct photons. Both approaches require a sensible reduction of the performance of the scanner, reducing the field of view or the number of photons reaching the sensors.

2.5.2 Scatter compensation algorithms

In literature tests have been done to improve scans made with a cone beam scanner (CBCT), affected by major artifacts, by means of a previous scan made with a tomograph of higher quality (CT), often passing through a virtual CT (vCT). The latter is done assuming that between the two scans (CBCT and CT) there were only small displacements of the various parts scanned, so that the vCT is made by a displacement or a deformable image registration (DIR) of the CT reconstruction. By having both CBCT and vCT available, it is possible to directly correct the CBCT [26]. In many cases the machine learning part is done by means of neural networks [27] [28]. Other methods use CBCT projections and as ground-truth the projections obtained by forward projection of vCT reconstructions [29]. More often, both input and ground-truth are obtained by simulation. The Monte Carlo method is considered a standard for being able to simulate all physical effects and thus being able to generate both input and output data for training a network. Neural networks based on Monte Carlo simulations are for example presented by [30].

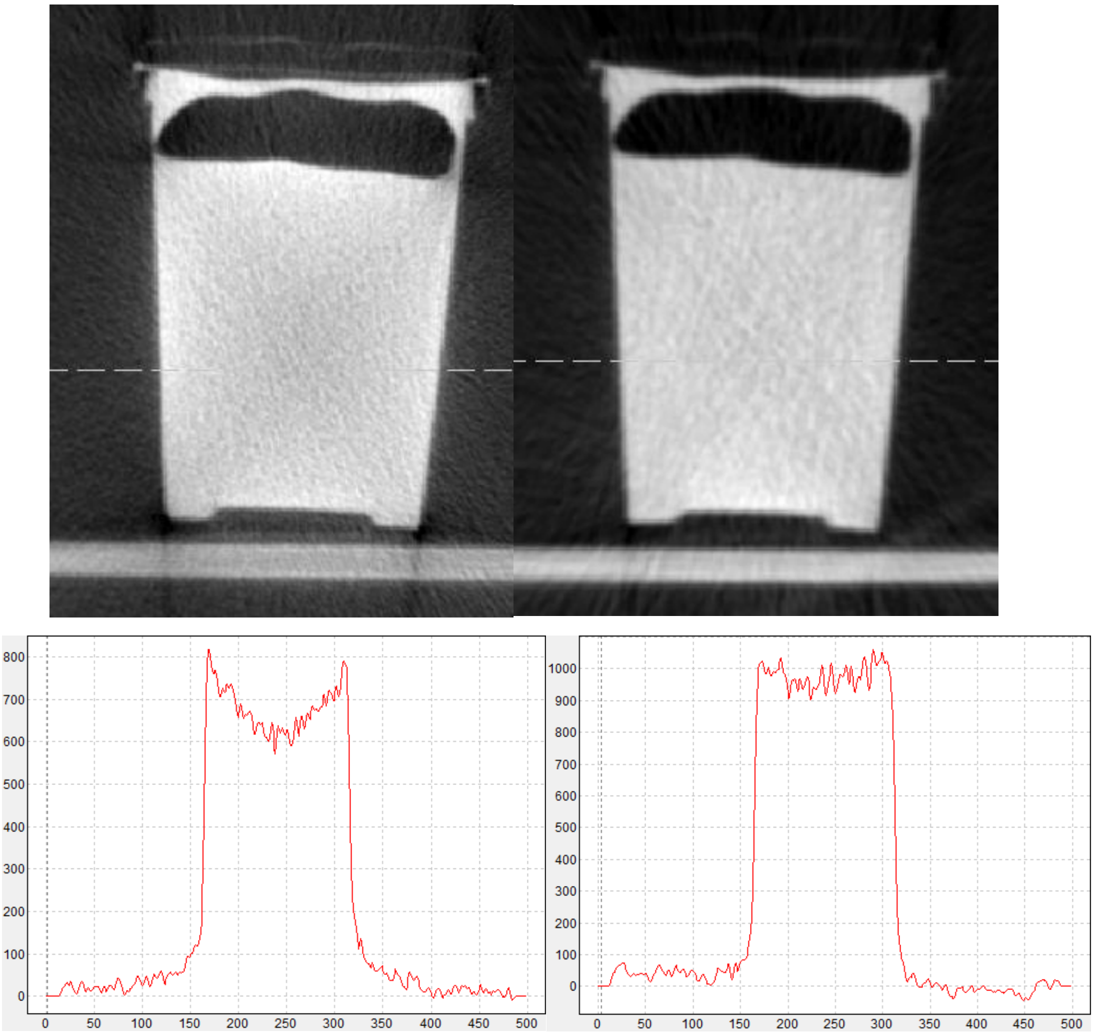

Figure 2.10 Scan of a yogurt can without scatter and beam hardening compensation (left) and with the compensation (right). Density profile (bottom) measured along the dotted line in the reconstruction (top).

A similar method relies on scanning known objects so that ideal projections can be recreated from knowledge of the scanned object [31]. In one experiment I tested the algorithm in order to compensate for beam hardening and scatter artifacts. In Figure 2.10

it is shown the result, where it is clearly visible the cupping artefact in the original reconstruction (left) that is removed after the application of the algorithm (right).

Chapter 3

Industrial tomography in the sawmill industry

3.1 Introduction[1]

Computed tomography has always been the dream of the sawmill industry. Since a few years after its introduction into medicine in 1972, the first tests on samples of wood were carried out. The composition of wood, mainly carbon chains, make the results of computed tomography very similar to those obtained in medicine in the analysis of internal parts of the human body. Just like the Computer Tomography revolutionized medical diagnosis, it was believed that knowledge of the internal structures of logs would revolutionize the primary breakdown. The first tests were carried out on logs in the early eighties [32] [33]. Even if the scan speed was very low and the quality of the images was low (Figure 3.1), the potential of the technology made clear that it would be possible to have a complete reconstruction of the internal details of each log during sawmill processing and that it would open many new opportunities of segregation, valorization and cutting optimization.

A lot of studies were done in the direction of automatic analysis of CT images and optimization (for a review e.g. [34]) and a database of CT scanned logs have been created in Sweden [35].

Since the nineties, the most advanced sawmills started using static X-ray scanners to determine inner properties of logs. The X-ray scanners are typically based on discrete X-ray scanning in 1-4 directions while the log is fed through the scanner [36] [37]. Discrete X-ray scanners provide information of properties such as heartwood content, strength, density, knot volumes, distance between whorls and annual ring width ([38] [39] [40]).

[1] Part of the content of this paragraph was published in [41]

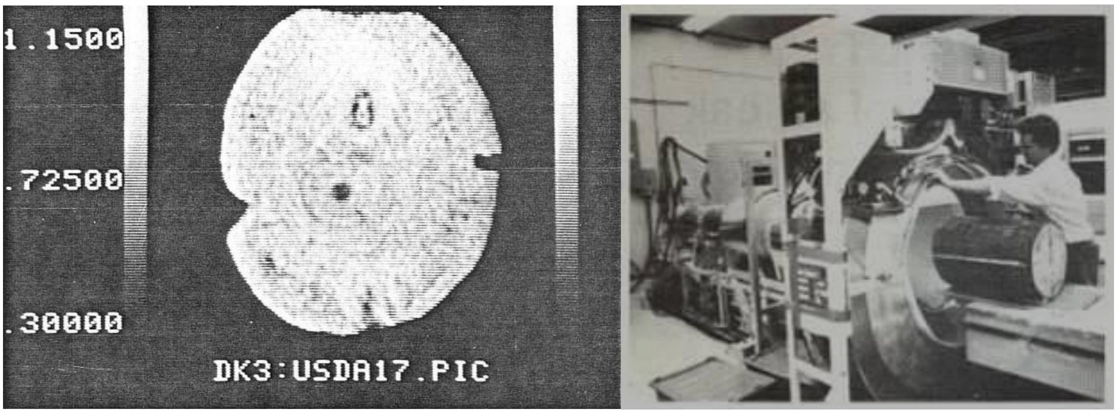

Figure 3.1 First scans of logs in 1984 [32] (left).One of the fist scan of logs at Imatron.(right).

The different amount of information measurable with a CT scanner respect to a static X-ray scanner was always clear but the possibility of building a system usable in an industrial sawmill seemed not feasible until the first decade of 2000 [34].

In 2008 Microtec began a project with the goal of building a CT scanner with the characteristics required for the industrial process and the ability to optimize the sawing process of each single log based on its internal features [41] [42].

A sawmill is a somewhat unusual industrial production plant because it has to produce different goods from one type of raw material with inhomogeneous characteristics. Moreover, the cost of the raw material has a high impact on the production costs, typically 64% in Sweden [43]. Each log can be sawn in different ways and, depending on its internal characteristics, different products will be obtained. For example, if a log containing many knots is sawn into thin boards for aesthetic purposes, all the boards produced will be discarded in subsequent quality control steps because a big amount of knots is usually not accepted. If, on the other hand, the same log is cut for large structural boards, their selling price will be lower than the value expected for aesthetic boards but they will not be discarded in the subsequent phases and therefore the revenue generated will be much higher.

A first benefit of the introduction of a CT scanner in sawmills is therefore the optimization of the cutting pattern of each log according to its internal characteristics. In sawmills, typically 20-30 logs are processed per minute, so all the operations of the process must be automatic. Figure 3.2 shows the automatic processing steps of the scanner data. The x-ray images are collected (1), transformed into tomographic images (2), the images are analysed to measure the internal characteristics of the log (3), the optimal cutting pattern is chosen by simulating various solutions and choosing the one that provides the maximum product value (4). Chapters 3.2-3.9 are dedicated to the presentation of the implementation of these steps. More advanced solutions will be presented in chapter 3.10.

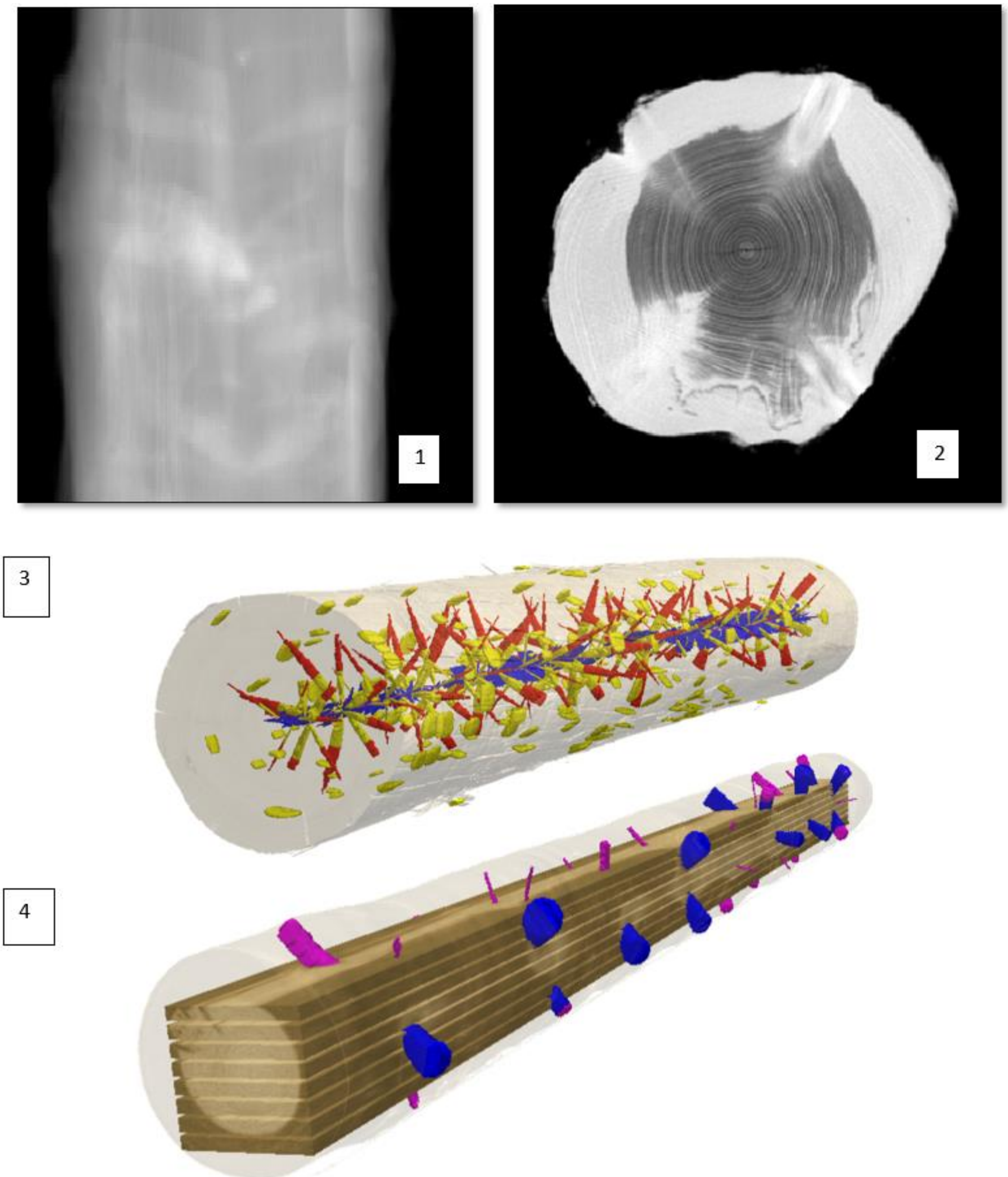

Figure 3.2 Steps for the automatic cutting pattern optimization. X-ray images (1) are transformed in CT images (2) then processed to analyze the internal features (3) and compute the optima cutting pattern (4).

3.2 Characteristics of CT Log[2]

The speed of a big sawmill for softwood can often reach 160m/min and most of the logs are smaller than 70cm in diameter, but sometimes they are not straight so the tunnel of transportation must be even bigger. For these reasons the main geometrical constraints required for this kind of scanner are a field of view of 90cm and a transportation speed of 160 m/min.

To achieve this speed we have realized a cylindrical array of sensors with length of 752mm and width of 1670mm. One advantage of the application is the relatively low resolution needed, especially in the longitudinal direction. Most of the internal features of a log are, in fact, built along its longitudinal axis, meaning that a high resolution in that direction is not strictly needed. Our design goal was to build an array of sensors with a pitch of 2.2mm in transversal direction and 16mm in longitudinal direction.

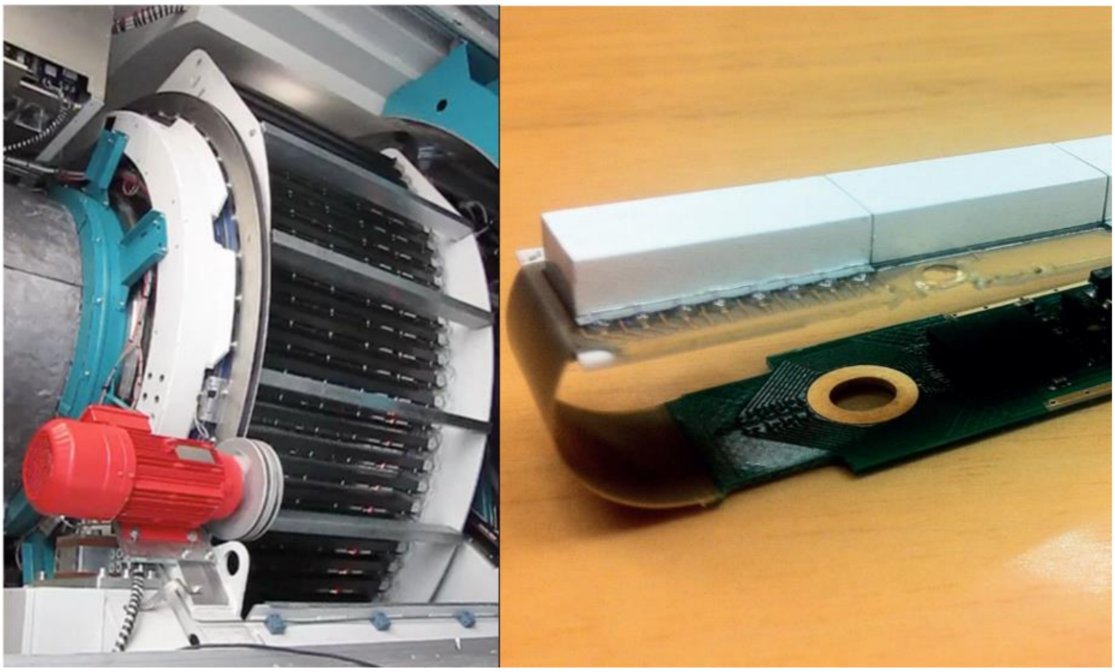

Figure 3.3 Internal view of the scanner, with the sensors mounted on the black bars in the gantry (left); one of the sensor modules developed by Microtec (right).

The solution was found in building single modules with 32 X-ray sensors each with lead collimators mounted. Every module of 32 X-ray sensors is made of a crystal scintillator array for X-ray to light conversion, a photodiodes array for light to current conversion and 24-bit ADCs for the digitalization of the analogue signals. The maximum sampling frequency is 3000 Hz. The digital data are collected by a two-level hierarchy of

[2] Part of the content of this paragraph was published in [42]

electronic boards and transmitted by a contactless data transmission link to the stationary part. The sensor boards and collector boards were all developed in house. The sensor matrix is constituted of 1081 modules with 32 sensors each. The sensors are mounted on a gantry rotating at 240rpm.

Scan speed	60-160 m/minute (1-2.7 m/sec)
Operating times	24/7
Maximal scan diameter of the log	70cm(depending on wood density)
X-ray tube voltage and current	200kV 14mA
Field of view	90cm
Transversal resolution	1 mm
Longitudinal resolution	1 cm
Cone beam angle	25°
Centrifugal force at the X-ray tube	64g
Maximal rpm of the gantry	240

Table 1: technical specification of CT Log.

The data is sent to a computer, which applies to the projections the beam hardening compensation, adaptive filters to reduce the noise when needed and the reconstruction algorithm. The beam hardening compensation is easier when scanning wood with respect to other applications thanks to the fact that wood is mainly made of carbon and water, which have a very similar absorption spectrum in the used range of energies (see 2.4).

Due to the high amount of data, a compression schema was required in order to cope with the limited bandwidth of the contactless data link. The control board firmware does the dark compensation on the attenuation signal, computes the logarithm and then send the value encoded as 12 bit floating point number. This simple algorithm achieves a compression factor of 40% without any visible artifact on the reconstructed image.

Since the main requirement was the implementation of a reconstruction algorithm sufficiently accurate and fast, the Katsevich algorithm [44] has been chosen for this. In the specific case it is not possible to expect a perfect spiral trajectory of the scanner, the first reason is that the speed of the conveyor cannot be assumed constant , while the speed of the gantry cannot change quickly due to the inertia. A second reason is that sometimes the logs are not sufficiently stable on the conveyor and sideway movements are possible during the scan.

For these reasons I chose to implement the version proposed in [16], where different trajectories of the scanner can be applied. In particular, the trajectory can be modeled as a standard spiral movement plus a rigid body motion with 6 degrees of freedom. The computational complexity of the reconstruction is very similar to the standard helix if the rigid body motion is limited to 4 degrees of freedom, assuming that the only possible rotations are along the axis of the scanner. Since this is the typical situation for a log moving on a belt conveyor, I implemented a reconstruction algorithm considering only translation in the 3 possible directions and rotation along one axis.

Usually a CT scanner acquires all the data of a scan and does the reconstruction of the whole volume when all the data is available. In order to reduce the space needed between the scanner and the sawing line this was not an optimal solution because it required to wait for the whole log to pass through the scanner before starting the reconstruction. In my implementation I preferred to create a continuous reconstruction scheme where the projections enter in the system, are filtered and back-projected. As soon as a new slice of reconstructed volume is ready (i.e. does not need any more back-projections), it is passed to the next stage of the system for the elaboration. In this way, we have a continuous stream of projections that are received from the sensors and a continuous stream of reconstructed slices that is sent to the image processing stage. In such a way, logs can be continuously processed even if they only have a small gap between them in the conveyor.

Figure 3.4 Installation of CT Log in a sawmill

The filtration and back-projection of each new projection requires the knowledge of the past and future trajectories of the scanner/object system. In a simple helical trajectory, this can be assumed as known but in the general case the filtration of one projection cannot start until the acquisition of the future positions is complete. The amount of rotation needed is between half revolution and a full revolution: more precisely the minimal rotation is $\boldsymbol{\pi} + \mathbf{2} \cdot \mathbf{asin}\left(\frac{\boldsymbol{r}}{\boldsymbol{R}}\right)$ where r is the radius of the field of view and R is the distance between the source and the axis of rotation. One slice of volume is complete when all the needed projections are backprojected, i.e. all the voxels with a certain z coordinate do not project any more in the Tam-Daniellson window [44] (we assume the z axis parallel to the axis of rotation). This requires always less than one revolution from the moment when the voxels had the same z coordinate of the source. Therefore we can always be sure that one slice of reconstructed volume is ready after 2 revolutions of the gantry from the moment when the slice passed the center of the gantry.

The algorithm was implemented on a computer with 3 Nvidia GTX1080 GPUs in order to do the filtered back-projection at 1600 projections per second. At the translational speed of 160m/min and rotational speed of 240rpm the helical pitch is 666mm, which means that each slice of the volume is reconstructed about 1.3 m after it passes the center of the scanner, equivalent to 0.5sec.

In Table 2 it is reported the time needed for the different computational steps needed in one application of CT Log.

Step	Time (s)	Space (m)
Passage of the log with maximal length	2.25	6
Tomographic reconstruction	0.5	1.33
Image processing	2.3	6.13
Cutting pattern optimization	1	2.66
Total	6.05	16.1

Table 2 time and space needed between the scanner and the final optimization of a log at 160m/min.

3.3 Log features automatic detection: pith and sapwood[3]

Typically a sawmill processes about 20-30 logs per minute: it is therefore impossible for an operator to analyze manually the CT images and decide the best solution. For this reason, algorithms for the automatic detection of the main features of a log where developed by exploiting state-of-the art approaches [40] [45] [46] [47]. Nevertheless, the

[3] Part of the content of this paragraph was published in [42]

increasing demand in precision of different features detection lead us to improvements in most directions.

Most of the structure of a log is built around the pith, the center of the year ring. For example, the knots and most of the cracks start from the pith and are oriented in radial direction, while the year rings, the ring shakes, and the resin pockets are oriented along circles around the pith. The detection of the pith position is done by applying a Hough transform on each slice (see Figure 3.5). Additional regularization filters forcing the continuity along the axial direction of the log are applied in order to consider that the pith is usually a regular curve with the exception of specific points where the top of the tree was broken [48].

In some case the pith position is not in the center of the tree, or the trajectory of the pith is not straight. The automatic detection of this cases is very important because it is an indicator of the presence of other features such as compression wood.

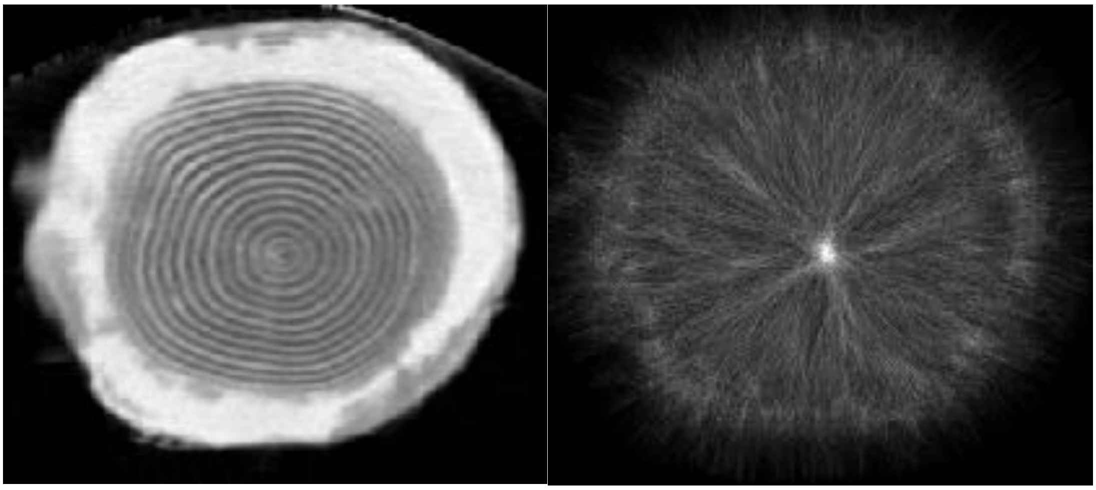

Figure 3.5Example of Hough transform used to estimate the position of the pith. On the original image (left), the gradient is calculated around each pixel. Along the direction of the gradient, a line is plotted on the map with an intensity proportional to the magnitude of the gradient. The accumulation of all the lines creates the map on the right, where the pith position is easily detectable.

In resinous wood trees, the wood in divided in an outer area with high water content, called sapwood, and an inner area called heartwood where moisture content is lower. For this reason the detection of the sapwood-heartwood boundary can be easily done in fresh wood. In order to simplify the further computation, a polar version of the CT images is computed.

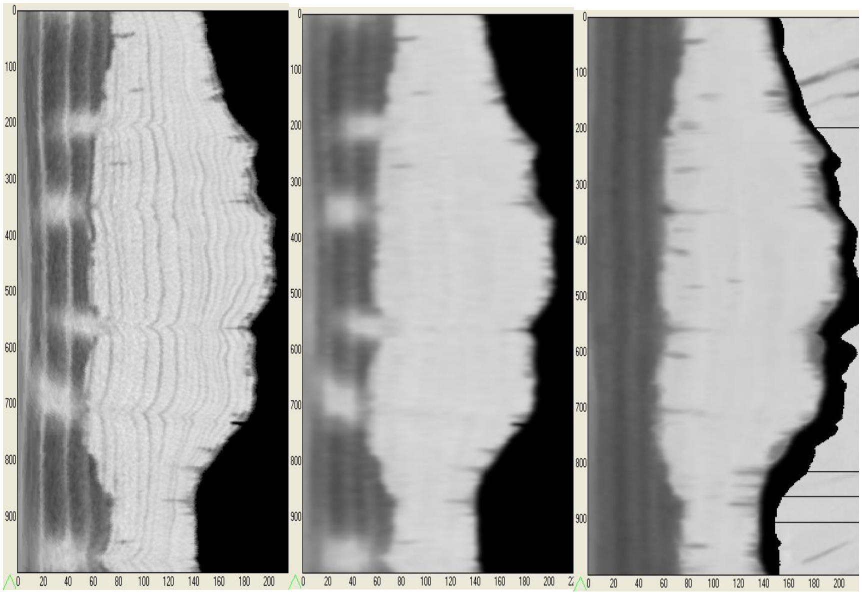

Figure 3.6 Polar representation of a CT slice, in the abscissae the distance from the pith and in the ordinates the angular position (left) effect of horizontal median filter (center) effect of median filter in the longitudinal direction (i.e. with adjacent slices) (right)

As visible on the left image of Figure 3.6, each slice is converted in a format having in the abscissae the distance from the pith and in the ordinates the angular position. A median filter in the radial and longitudinal direction removes the grain and knots from the images leaving almost only the signal due to the sapwood/heartwood difference. Computing the first gradient above a threshold and regularizing the positions allows to compute the border between the two areas of the log.

3.4 Log features automatic detection: Knot detection[4]

The most important feature in each log is the knots detection, localization and estimation. The knots are the part of the branches that are included in the log during its growth and can be roughly described as cones with the top on the pith extending radially toward the outer surface of the log. In the central part of the log (*heartwood*), the density of the knots is higher than the sound wood. In the external part of the log (*sapwood*), the density of knots and sound wood is very similar but the texture of the image is often different.

The dead knot border is the point that divides the part of knot that is sound from the one where the knot is dead. On the dead part of a knot, a thin bark layer divides the knot

[4] Part of the content of this paragraph was published in [49]

from the rest of the wood: therefore, the mechanical connection with the rest of the wood is lower, sometimes causing the knot to fall off the board. Also the structure of the fiber around the dead and sound part is different. For this reason a clear estimation of the point where a knot becomes dead is very important in order to be able to optimize the cutting pattern and produce boards with higher quality.

The automatic detection of the internal features of a log from CT images has been addressed by many works, especially for knots detection [50] [51] [52] [53] [46]. Only a few of them [54] [47] addressed the problem of the detection of the dead knot border. In [54] the coefficient of determination of the linear regression between the predicted and measured percentage of sound knots on each board was measured to be R^2=0.72. In [47] the detection was accomplished measuring the point where the diameter of each knot stops growing. The RMSE of the dead knot border estimation on Pine logs was of 12mm.

Convolutional Neural Networks (CNN) were applied in order to improve the detection of knots from CT images. The detection was performed in two steps: the first step applies a semantic segmentation on the whole log in order to define the position of each knot. In the second step, an area around each knot is analyzed in order to calculate its properties, and in particular the measurement of the dead knot border.

The neural network in charge of the semantic segmentation is a fully convolutional network that performs 2D convolutions on volumes of consecutive slices of CT images to produce probability maps expressing the likelihood that each pixel is part of a knot. The second network has the purpose of classifying volumes of knots as sound or dead and of identifying the right dead knot border position.

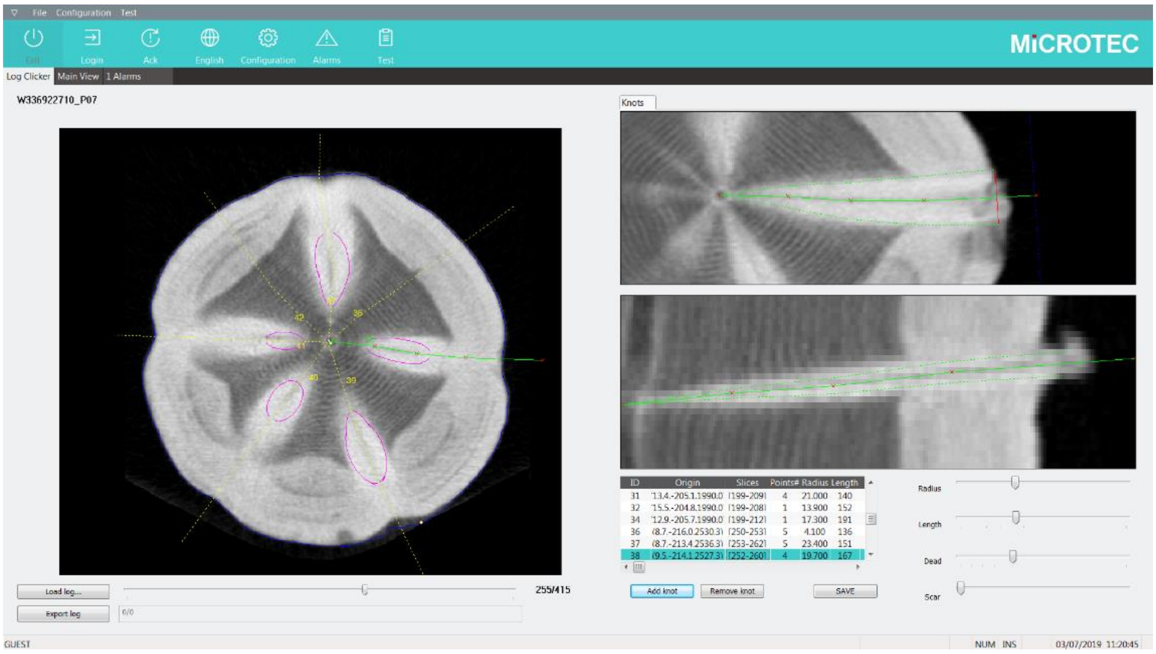

Figure 3.7 Visualization of the software for the manual labelling of the knots. Different views of the same area are shown in order to help a precise definition of the positions.

Even if in another work we introduced techniques for data augmentation in case of insufficient amount of training samples [55] , one of the important requirements of using deep learning is that a big number of samples must be collected and labelled with accurate information to correctly train the system. The correct labelling requires a lot of work from trained people but also a correct procedure. For this reason, a specific software was developed for labelling the dataset by visual inspection of CT images. The definition of the dead knot border from CT images was a hard task for our graders, therefore we chose to use measurements taken directly on the surface of the boards after the logs were sawn, since the status of a knot is clearly visible on the surface of a board but not as clearly interpretable from CT images.

3.4.1 Step 1: Knot identification

CT Log produces 3D images where each voxel has the dimension of 1x1 mm in transversal direction and 10 mm along the axis of the log. In the remainder of this paper we will call x and y the first two coordinates of the CT images, transversal to the axis of the log, and z the third coordinate.

In order to visualize and label in 3D each knot, we developed a software shown in Figure 3.7 where different views of the same part of the log were presented in the same screen in order to label the starting point, end point, dead knot border and diameter profile of the knots. It was also possible to define any number of intermediate points along the trajectory of the axis of the knot.

The CT images of 75 Scots Pine logs (Pinus Sylvestris) that were scanned in different sawmills in Europe were collected in order to create a database. The knots of those logs were manually marked with the software described before and a total of 10.118 knots were collected.

The parametric labelling was transformed to produce a 3D volume of voxels indicating whether each voxel belongs to a knot (voxel value = 1) or is not part of a knot (voxel value = 0). Each slice was scaled in order to have consistent slices dimension (128 x 128 pixels) on all logs. Then, as network input, groups of images composed of 5 adjacent slices were created.

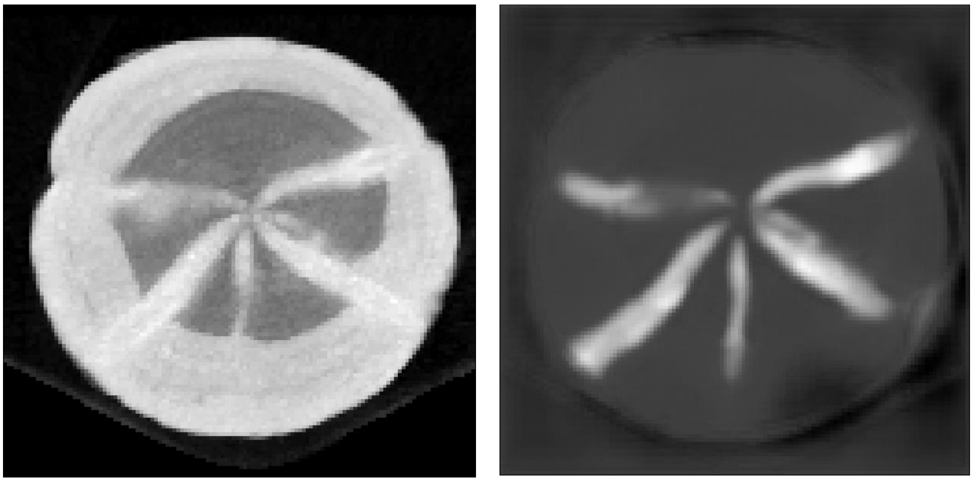

Figure 3.8 The original image scaled at 128x128 pixels (left), the CNN segmentation (right)

The CNN was then able to produce a 3D image of the same size of the input were each voxel expresses the probability of it being part of a knot, as shown in Figure 3.8.

In order to identify the position and the bounding box of each knot, a special version of the Hough transform [56] was implemented. One strong simplification of the model comes from the fact that almost all knots in a log start from the pith, since epicormic knots are very rare in forests. The position of the pith along the log can be easily calculated (e.g., [48]): a set of values xPith(z) and yPith(z) is therefore obtained. The axis of a knot can then be parametrized with 3 parameters:

- zStart: the z coordinate of the position where the knot starts
- Orientation: the angle of the direction of the knot in the x,y plane;
- Slope: the inclination of the direction of the knot in the z direction with respect to x-y plane.

The algorithm creates a 3D Hough map based on the 3 parameters by looping on a range of possible values of slope between -30% and 30% at step of 2%. Given the slope, for every voxel a unique knot axis passing through both it and the pith exists. So, it is possible to compute the pith position in which the knot starts zStart(x,y,z,slope), where x,y,z are the position of a generic voxel. Then we can calculate the orientation of the knot as orientation(x,y,z)=atan2(yPith(zStart),xPith(zStart)). With this functions it is possible to calculate for every slope and x,y,z voxel, the correspondent zStart,orientation coordinate in the Hough map and add the probability value calculated with the CNN in order to compute the probability of a knot with the given parameters. Choosing the best local maxima of the map allows to create a list of axes of the knots. An example of two layers of a Hough map is shown in Figure 3.9.

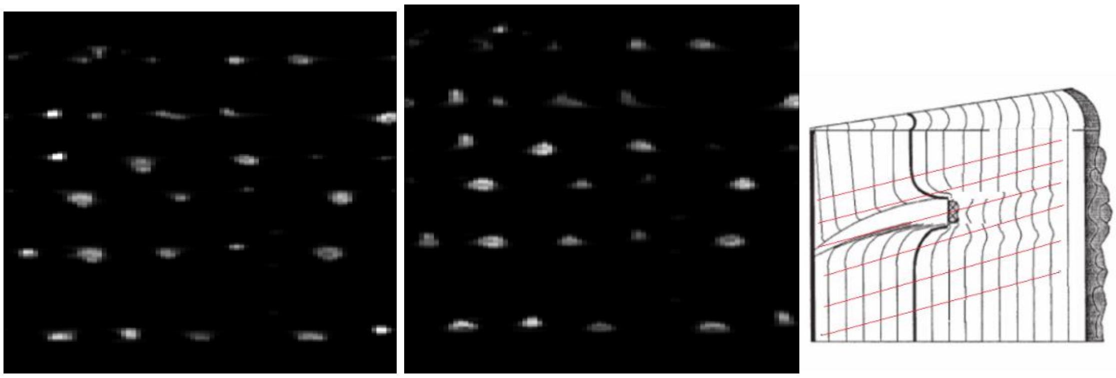

Figure 3.9 The Hough map of the knots: the orientation in the horizontal axis, zStart in the vertical axis. On the left image the plane with slope=0% is shown, on the central image the plane with slope=4%. On the right side a sketch of the sloped lines of integration.

3.4.2 Step 2 knot area analysis

Once the axis of each knot has been identified, a 3D volume of voxels is extracted. We define the 3 directions of the extracted boxes as:

- radial direction (r): along the orientation of the knot in the x-y plane
- tangential direction (t) orthogonal to r and z directions
- z direction

The extracted voxels groups are volumes with fixed dimension of 160 x 80 x 80 in the r, t, z directions, respectively. A different scale factor is applied to the three directions in order to optimally fit each knot in a volume, depending on the radius of the log, the maximum expected diameter and the slope. We obtain volumes as in Figure 3.10(top).

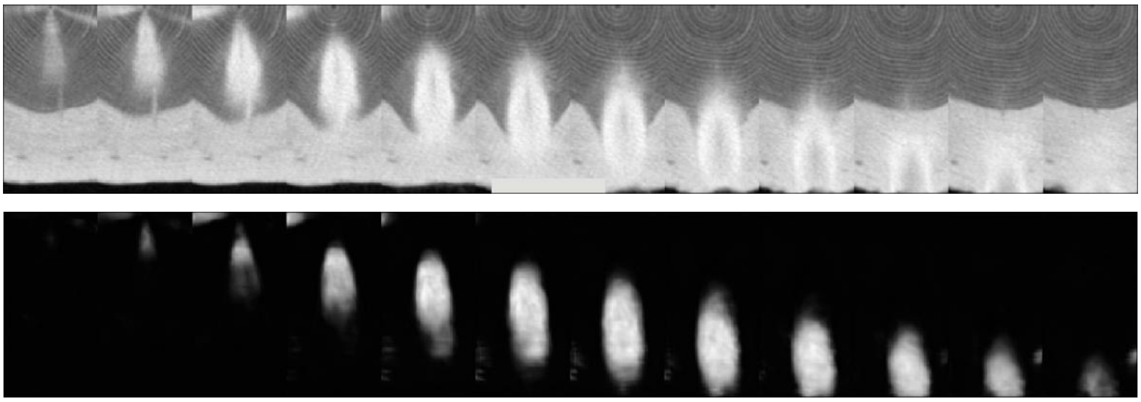

Figure 3.10 The block of pixels around a knot. Original image (top) and result of CNN for semantic segmentation (bottom)

One possible solution is to perform a new semantic segmentation on these knot blocks. The analysis of the dimension and center of the segmented voxels along the r direction allowed to compute the direction, dimension and length. The dead knot border is calculated as the point where the dimension of the knot stops growing along the r direction.

In order to improve performances specifically on the detection of the dead knot border and knot diameter, a more reliable ground truth, specific to these two metrics, is needed. The only way to extract reliable ground truth on those metrics was to check the appearance of the knots on board surfaces instead of using CT images. 13 logs of Scots Pine were scanned with a CT Log scanner, sawn in thin boards 15mm thick and the knots were manually measured on the surface of the boards. A reference was taken on the logs by drilling some holes so that it was possible to compute the position of a knot in the CT image given the measured position on the board and vice versa. On the 13 logs, 2412 knots were measured on the surface of the boards.

In Figure 3.11 (right) the original CT images are visible with the position of the boards and the measure of the knots taken manually superimposed. In particular, the minimal, maximal diameter, position and dead/sound status were annotated. The information related to each knot was reported in the reference system of the specific block of voxels extracted in order to train a neural network.

The problem is that the requested information (dead knot border and diameter profile) would require a dense ground truth along the radial direction, while only a few manual measurements are available depending on the thickness of the boards and their angle with respect to the knot axis. It was not possible to train a network on the whole knot volume when the ground truth was valid only for a few points along its length (only 1 or 2 points).

Figure 3.11 An example of reference taken on a log that is CT-scanned and then sawn in boards (left), the manual measurements superimposed on the CT image (right).

To correctly train the network we decided to extract sub-blocks of 11 slices along the r direction around positions where the ground truth was available. Two different networks were trained: one to compute the dead/sound status, the other for the computation of the diameter of the knot.

During the training of the sound/dead network it was possible to extend the ground-truth information also to other points of the knot. If a knot was marked as sound at a certain coordinate r_alive, for obvious biological reasons the knot was alive also at all r<r_alive. For the same reason, if a knot was marked as dead at a certain point, all the subsequent slices have to be marked as dead. This allowed to create a dataset with a high number of samples. At this point the network is able to classify the single slice of a knot to either dead or sound, but it is obviously faster to infer this information by comparing the actual distance of a slice from the pith with the dead knot border value of that knot. To find a knot’s dead knot boder, for computational time constraints, one slice every six was tested. Once the point where the status passes from sound to dead is found, we then refine the detection to pinpoint the exact slice. After the calculation of the dead knot border we verified the performance of the system by comparing the predicted status with the status of the knots in the sawn boards.

As ground truth for the computation of the diameter we decided to use as training set only the slices of knots where there was a manual measurement. An interpolation of the measured diameter in the slices between two consecutive measurements were possible, but it could have reduced the precision of the system. As long as we can consider that branches are not elliptical, we use the minimal diameter measured on the board as the diameter of the knot in the 3D image.

3.4.3 Results of knots segmentation

To design and train the networks, we used a computer running Windows 10 Pro, Keras 2.2.4 with Tensorflow 1.13.1 as backend. The first network, aimed at semantic segmentation, has a total of 1.962.913 parameters. It follows the U-Net architecture [57] with skip connections and convolutional blocks consisting of 2 consecutive convolutional layers. The first layer interprets the channel axis as a depth axis. Starting from an image size of 128x128 with 5 channels, it compresses the image to a size of 8x8 with 256 channels in the center. Then, in the so-called “upward path” of U-Net, the image is upscaled to the original resolution with 1 output class as channel (the probability of a pixel part of the central slice to be part of a knot). Each convolutional layer applies 3x3 kernels, and for the optimization the Adam optimizer has been used with a learning rate of 0.0002 with binary crossentropy as the default loss function. Early stopping and learning rate reduction on plateau have been used during the training process. The inference time for the computation of a log 4.2 m long was 650 ms. All computation times were measured on a computer using an RTX 2080 GPU on an Intel Core i7-4770 3.4GHz.

3.4.4 Results of dead knot border detection

In total the 13 logs presented 634 knots. Each knot intersected one or more boards, the manual measurement were taken at those intersections. The 634 knots intersected the boards in 2412 measured points. 1835 knot intersections were randomly chosen for training and validation set (75% for training and 25% for validation). They generated 34917 knot slices with known dead/sound status and used for training and validation of the neural network. 577 knots intersections, belonging to 158 knots, were used for the test of the detection of the final algorithm estimating the dead knot border.

The test of the performance was done comparing the status of the knots manually measured on the boards with the expected status based on the estimated dead knot border. The results are presented in Table 3.

		predicted	
		Sound	dead
actual	sound	301 (88.5%)	39 (16.4%)
	dead	39 (11.4%)	198 (83.5%)

Table 3 Confusion matrix of the classification of the sound/dead knot classification

The inference of a single slice of the network used for the dead/sound classification required 0.42 ms. Every knot required the inference of 23 knot slices, so in total the computation time for the dead knot border of a knot was 10 ms.

3.4.5 Results of knot diameter measurement

For the training and validation of the network, 1776 intersections of the knots with boards were used (75% for training and 25% for validation), while 564 were used for the test.

The standard deviation of the difference between the manual measurement and the predicted value of the diameter was 3.2 mm, the average -0.1mm. In Figure 3.12 a comparison of measured and predicted diameters is shown.

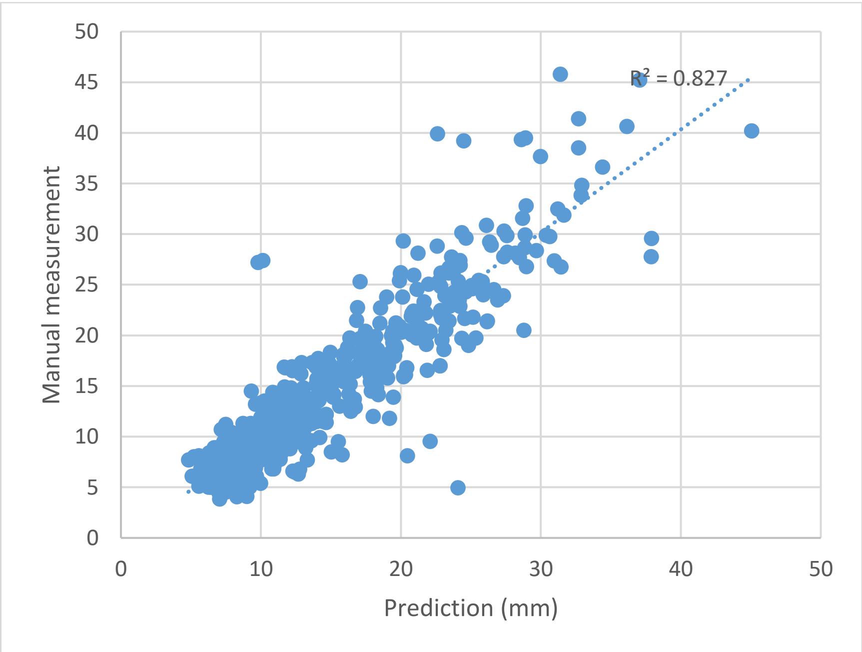

Figure 3.12 Comparison of the diameter estimation of the knots

The inference of a single slice of the network for the diameter estimation required 0.58 ms. In total, 12 volumes needed to be inferred in order to compute the diameter along each knot, requiring 6.7 ms per knot.

In total, the computation time for a 4.2 m long log with 50 knots was 1450 ms on a single computer with one GPU [49].

3.4.6 Extension of the concept of training from cut pieces

Addressing the problem of knots feature detection, we realized that in general the idea of cutting logs to obtain a ground truth for a neural network could be extended to other applications, I described in details the idea in a patent [58]. It is possible to use tomographic data to create ground-truth for training board scanners for features that can be accurately measured with a CT (e.g., the pith position). In particular it is interesting that the process of cutting logs is already done in each sawmill and connecting the data of the boards with the correspondent log can be done automatically using the concept of board fingerprint (see 3.10.5). In this way, a large database of CT Log images and scanned boards that can be used as training set for machine learning applications, can be created automatically during a normal sawmill production.

3.5 Log features automatic detection: blue stain

An important characteristic from an aesthetic point of view is the discoloration due to fungal attack. Some species of fungi attacking the sapwood area are important because of the blue coloration they give to wood.

Maintaining moisture in the outer part of the log (sapwood) or drying it out prevents the development of these fungi in cut logs [59]. In living logs sometimes fungi causing blues stain can develop, especially in association with insects attack. In these cases the first effect is the drying of the part of sapwood attacked by the fungi [60]. In Figure 3.13 two examples of blue stained wood.

In both cases (attack on live or cut trees) the sapwood attacked by fungi has a lower percentage of moisture than normal.

According to what has just been said, and as validated by our experience, the bluing is never present in the parts of the trunk where the sapwood moisture has remained at the normal value. There are, however, logs with abnormal moisture content (which would therefore be highly exposed to fungal attack) but still healthy, for example because they are not exposed to contagion.

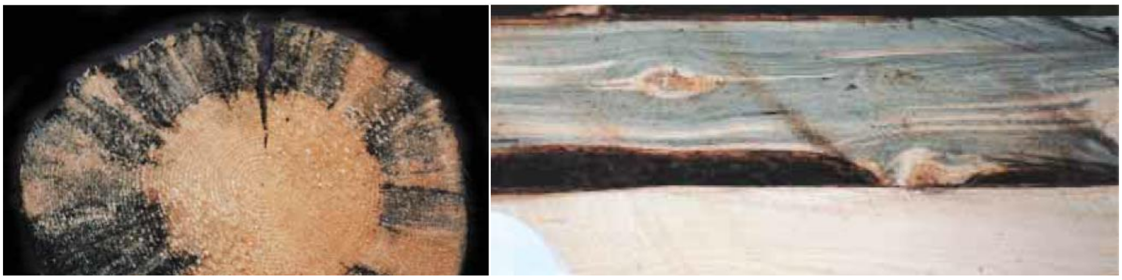

Figure 3.13 Heavy blue stain discoloration on a log (left) and a board (right) [59]

One common practice to produce bluing-free boards consists in keeping cut logs wet during warm seasons. During the cutting of the logs the potentially stained logs are dedicated to productions where the aesthetic value is not important. This is done through visual analysis of the operators or simply by suspending in the warmer months the production of wood for applications where the aesthetic value is important. Measurement of decay attack with microtomography was tested [61].

In literature I found papers on measurement of decay attack with microtomography [61] but none related to automatic detection of blue stain from tomographic image, so that I developed with a colleague a method presented in patent [62] capable of automatically detecting if a log is free of blue stain by measuring the percentage of moisture. The system is also able to detect parts of the log that are definitely healthy so as to cut products for aesthetic use from those areas and products without aesthetic value in the potentially attacked areas.

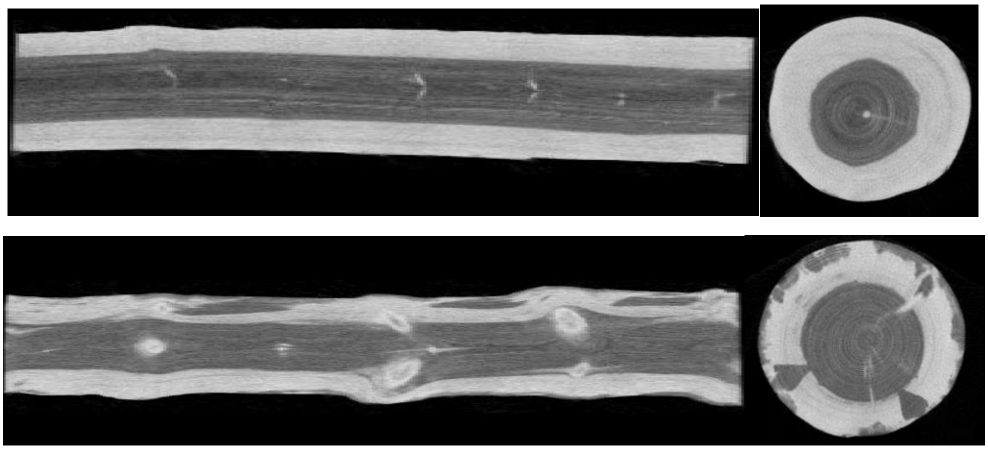

Figure 3.14Tomographic images of a longitudinal section (left) and transversal slice (right) of a fresh log (top) and a log partially dried (bottom). The darker central area is the lowest density and moisture content heartwood.

The logs of resinous species have a clear division into an inner part called heartwood and an outer part called sapwood. The density of the dry part of the wood in the two parts is usually very similar and varies little in logs of the same species; while the moisture content of a freshly cut healthy tree is about 30% in the heartwood and 100% in the sapwood. Starting from the density of the various parts of the sapwood, and possibly correcting with the average density of the heartwood, it is therefore possible to estimate with good accuracy the percentage of moisture.

In the case of a CT scanner, it is possible to distinguish in a first step the heartwood zone from the sapwood as the central zone with lower density, in a second step the dry sapwood zones due to the lower density.

In Figure 3.14 CT images of a fresh and dried log are visible. Even when the log is partially dry it is still possible to distinguish the central part of heartwood because the log tends to dry from the outside to the inside, so the edge heartwood / sapwood remains clearly visible. When the drying covers the entire thickness of the sapwood, it becomes difficult to distinguish the two parts of the log but it can easily be said that the whole section is exposed to the attack of fungi.

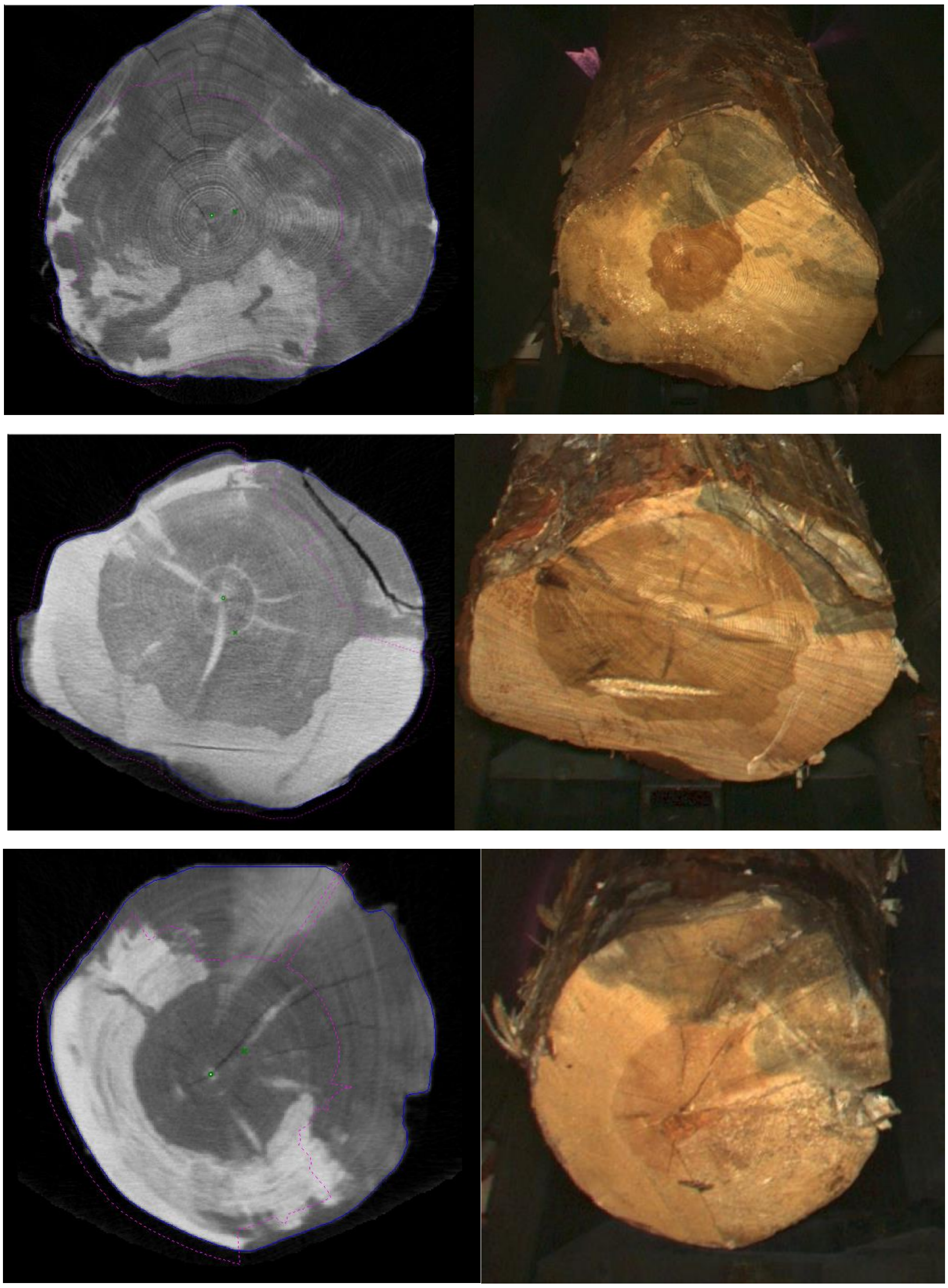

Figure 3.15 Examples of color pictures of logs with blue stain in one end (right) and correspondent CT slice (left). In purple is highlighted the areas of sapwood with low density that are exposed to blue stain fungi attack.

In Figure 3.15 some examples of CT and colour images of logs with blue stain. In purple it is visible the areas detected as dry. Not all the dry areas (dark areas in the CT image) are discoloured, but all areas where the moisture is high are sound.

3.6 Log features automatic detection: insect infection

In specific condition some trees are attacked by insects depositing their eggs inside the log. The larvae, before exiting the log, dig tunnels into the wood that degrade its quality. Some work in literature assess the possibility of using microtomography or terahertz tomography for detecting larvae infections [63] [64] but I found no work related to automatic detection algorithm or performance. I decided to develop an algorithm based on CNN.

As visible in Figure 3.16,the tunnels created by the larvae are not always easy to see in the CT images for the following reason:

1. Sometimes the channel are empty (so they are dark in the image), other times are full of sawdust (so they are white).
2. The density of the wood is not constant so that many parts have a texture similar to the tunnels due to drying, annual rings, pitch pockets, cracks or bark.
3. The resolution is very different in the 3 dimensions: on each slice the transversal resolution is 1mm, while between the slices is 10mm. For this reason, when the tunnels are parallel to the slices they often become invisible due to lack of resolution.
4. Often the tunnels are recognizable only when a number of slices are analysed at the same time.

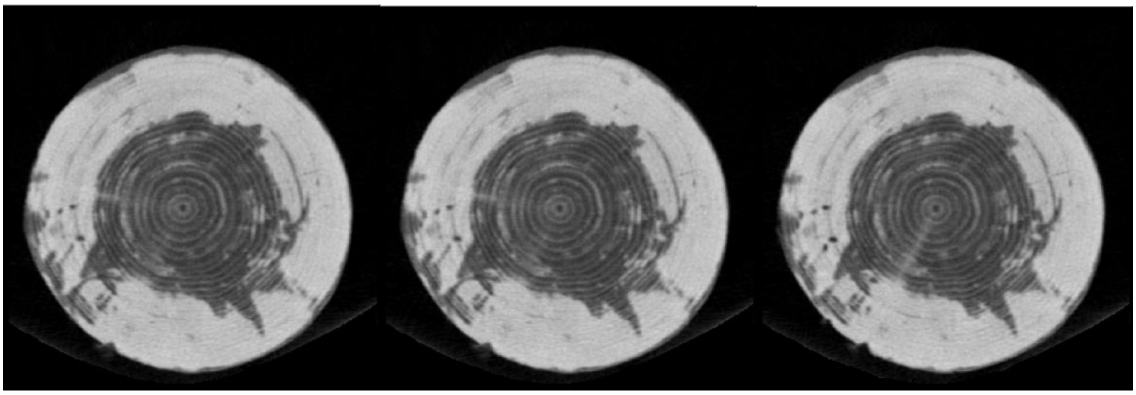

Figure 3.16 slices of the same area infected, each slice is taken at 10mm from the other.

In the algorithm I implemented, the volume was divided in sub-regions and each region classified independently with a 3D CNN. The input of the network are images of dimensions 8x32x32 voxels (8 in the direction of the axis of the log, 32 in the others). In the rest of the description they will be called blocks instead of images, in order to avoid confusion with 2D images.

The blocks are extracted from the 3D volume of the tomographic scan with an overlap so that the spacing between the blocks is 4x15x15. The blocks out of the log or too close to the center were not considered as long as the insects cannot attack the center of the log.

The position of the block respect to the center of the log is important in order to detect a tunnel: resin pockets are always along the year rings while the tunnels are typically orthogonal. The blocks extracted would not have that information unless they are able to identity automatically the year rings (which are not always visible). For this reason the blocks were rotated in order to have the radial direction parallel to the first axis.

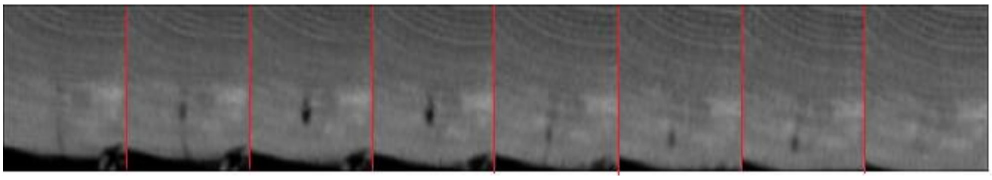

Figure 3.17 Representation of the 3D voxels of one input block. Red lines divide the 2D images in the stack.

49 logs were selected for manual annotation. Infected and sound areas were manually clicked and the blocks close to the marked points were saved as sound or infected. In total 5480 sound blocks and 11477 infected blocks were saved. In addition, 99 logs was verified to be completely sound and 16732 blocks were randomly extracted from those logs.

Figure 3.18 Software for the manual annotation

1960 samples were used for initial test, 3920 for validation and 56019 for training. The design and train of the network have been done on a computer running Windows 7 Ultimate, Keras 2.2.4 with Tensorflow 1.13.1.

The structure of the network is simple and tuned in order to have small errors but also a fast computation time. The input layer has dimension 8x32x32 with one channel. In order to deal with 3D images, the usual conv and max_pooling layers are substituted with conv3d and max_pooling3d layers. Groups of two convolutional 3x3x3 layers followed by max pooling are repeated 4 times. The results are then flattened and passed to a dense layer. An Adam optimizer was used and binary cross entropy as loss function. The trainable parameters were 110,825 the non-trainable 480.

After 45 epochs of training the loss and accuracy were

	Loss	accuracy
Training set	0.0927	0.9794
Validation set	0.1541	0.9607
Test set	0.117	0.9617

Table 4 Results of the training of the network

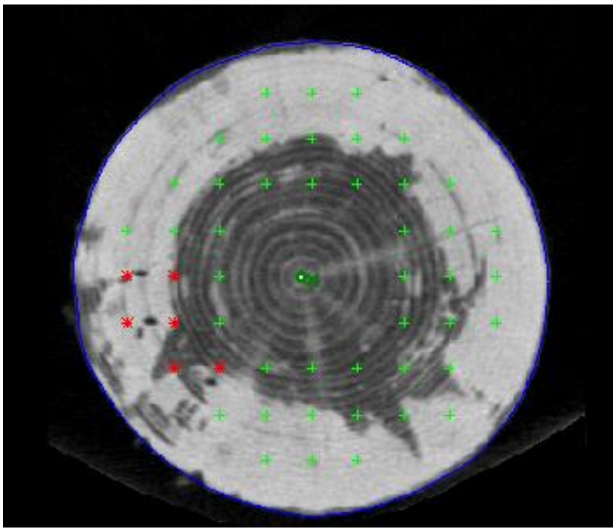

Figure 3.19 Example of results of the inference, in red the blocks with result >0.9 in green the others

3.7 Log features automatic detection: spiral grain

Often the tree grain grow in spiral direction and the mechanical properties are affected. In Figure 3.20 an example of tree affected by spiral grain and a sketch showing the different angles present at different distance from the pith. Different studies has been done on the analysis and detection of the phenomena [65] [66] [67].

Figure 3.20 Example of tree with spiral grain (left) and sketch of typical spiral grain in a tree (right) [66]

Detecting the logs with such a features is important to sort correctly or treat the boards accordingly. “A common problem that often arises when dealing with wood with spiral grain is warping, defined as the distortion of the original. When it is caused by spiral grain, it happens along the length of the plane and it’s called twist. This issue is particularly relevant during the drying procedure and there are a few methods to monitor it: increase the boards width, increase the ratio between width and thickness, keep high temperatures during drying, use reinforcements to induce a reverse twist (easy if the twist is moderate but can lead to breaking if the needed force is too high) and keep any change in moisture down to the minimum (shipping wood to different locations can be a problem). Another trick is to choose wisely the position of the boards that form the pile, avoiding to put them all in the same direction but rather in some way that compensates an existing twist. An efficient drying process, following the guide lines listed above, will minimise the problem of twisting. Underestimating spiral grain would bring later problems to the final product made with the deviated wood. Warping would keep going and the probability of seasoning checks (separations of the wood along the grain) would increase” [68] [69].

I developed a first version of software for the automatic detection of spiral grain angle from CT images and installed it in the CT Log solution at the sawmill Norra Timber in Sweden. The software was based on the evaluation of the energy of concentric images around the pith where filters with different angle were applied. To verify the physical properties measured, we did a test in a collaboration with Norra Timber and Olof Broman and Johan Oja from Luleå University of Technology.

The first part of the test verified the correlation between the spiral grain angle detected with CT Log and the grain angle of the sawn boards. The grain direction was measured in the laboratories of Luleå University of Technology with a device based on tracheid effect as shown in Figure 3.21 (left). In Figure 3.21 (right) it is shown the correlation between the two measurements.

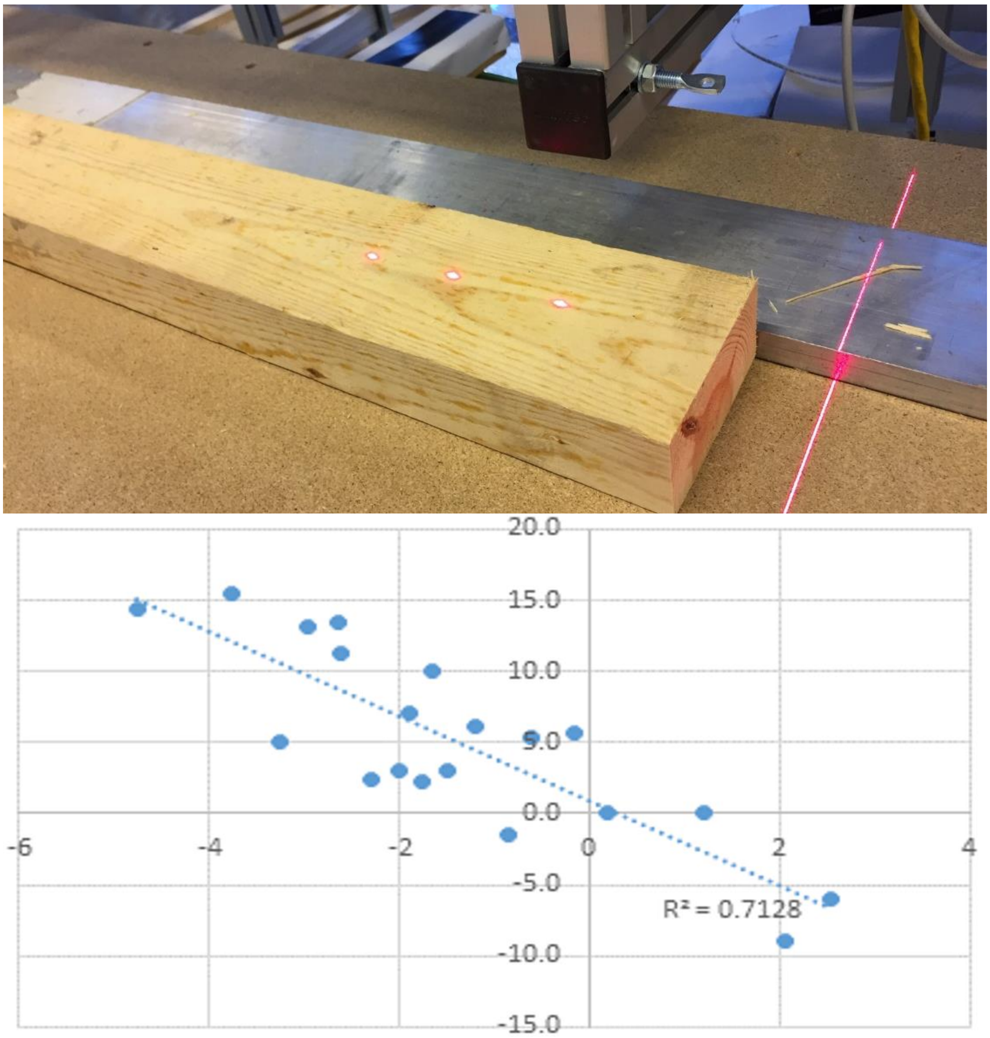

Figure 3.21 Lab setup for the measurement on the boards (top). On the bottom picture: correlation between the angle measured with CT Log (ordinate) and tracheid (abscissa).

A second test was done at the Norra Timber sawmill, where 50x100mm boards produced from Spruce logs were separated in two groups based on the spiral grain angle measured by CT Log. This first group had boards coming from logs with more than 15° spiral grain angle and was about 5% of the samples. The boards were dried to 16%, three layers in the top of the package without pressure frame. Boards from the two groups were mixed in the same layers. As visible in Figure 3.22 right, the boards of the group with higher spiral grain measured with CT Log had higher skewness after drying.

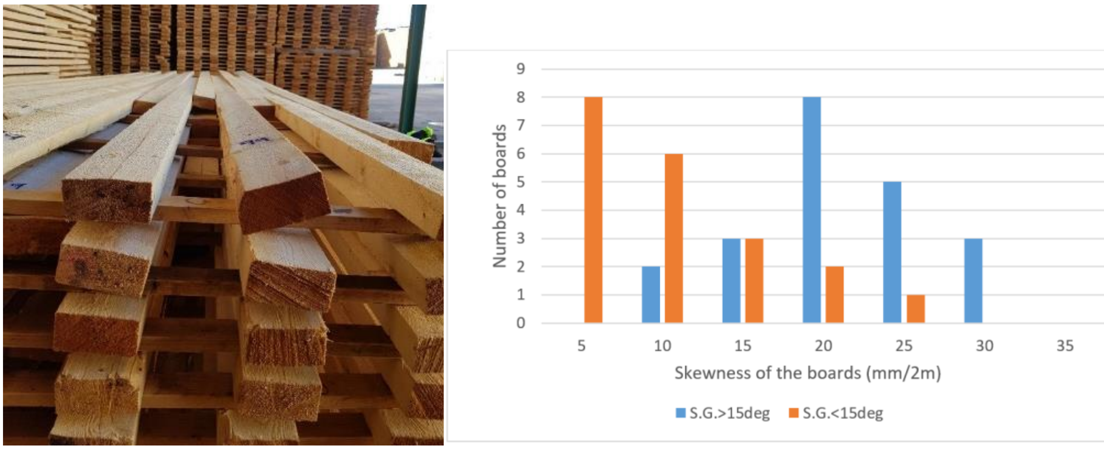

Figure 3.22 Pictures of the dried boards of the test (left) Distribution of the skewness of the boards coming from logs with low spiral grain (orange) and high spiral grain angle (blue) (right).

In order to improve the precision of the measurement, we decided to start the development of a new version of software based on CNN able to measure the angle at different distance from the pith. The work was part of a master thesis where I was co-advisor [68] .

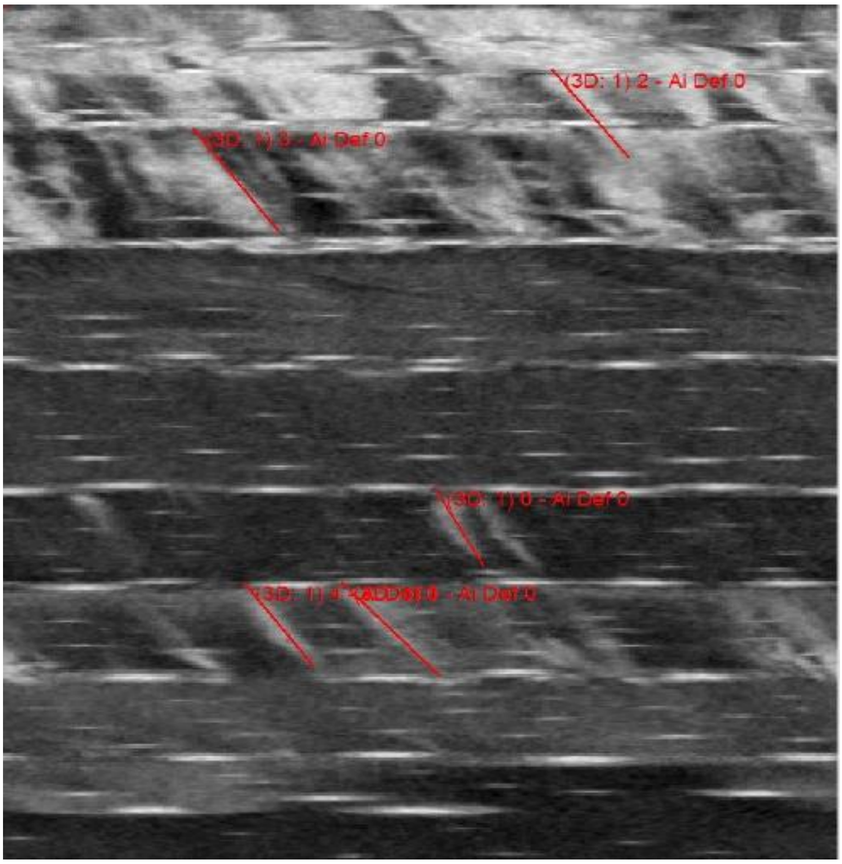

Figure 3.23 manual annotation of the grain direction in a concentric surface of a log.

The CT scans of 146 logs were used to produce multiple images along concentric surfaces at a fixed distance from the pith. Where the fiber angle was visible in the concentric images, the angle was manually annotated (Figure 3.23). In some areas, no indication of the fiber direction was visible, so that no annotation was done.

The concentric surfaces were divided in patches with a fixed dimension and used to train two convolutional neural networks. A first classification network was trained to predict which images contained information on the direction of the grain and which images had insufficient information. A second regression CNN was trained to predict the average angle of the fiber on the image. Only the images with sufficient information on the fiber angle were used for the training of the second network. 130 logs were used for training, 8 for test and 8 for validation. The regression network was trained to predict the fiber angle of the image.

For each log different images were produced in different position and distance respect to the pith, all the images were passed to the first network to decide if the fiber angle on that image was measurable or not. Only the images that were considered useful at the first step was passed to the second network.

The results of all images passed to the second network was used to fit a model. The angle of the fiber is expected to change linearly with the distance from the pith, so that a model with 2 parameters is fit to all measurements to get a global description for each log.

A final test have been done on additional 50 logs. The verification have been done comparing the spiral angle at a distance from the pith equal to 1/3 and 2/3 of the radius of the log (Figure 3.24).

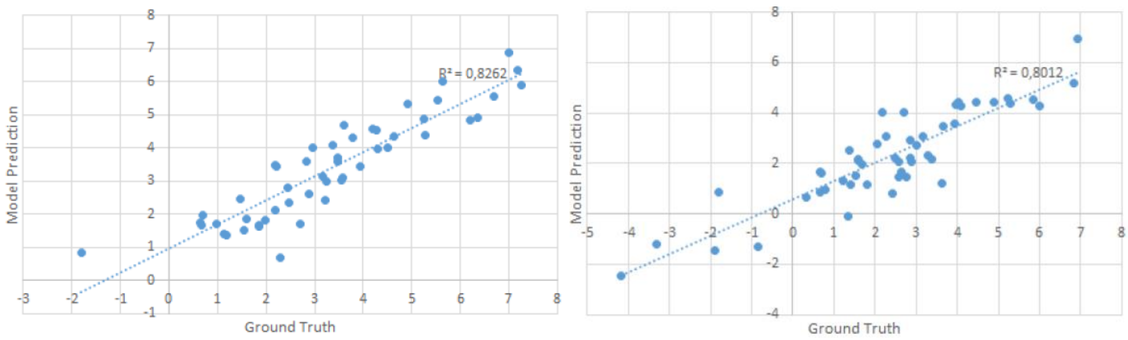

Figure 3.24 Correlation between predicted and manually measured angle of the fiber at 1/3(left) and 2/3(right) of the radius of the log.

3.8 Log features automatic detection: others

Other detection features have been developed but not described in detail in this work. In particular cracks, resin pockets, rot, metals, annual rings, bark enclosures, species recognition, under bark measurement.

3.9 Cutting pattern optimization

The automatic detection of all feature allows to create the concept of virtual board as illustrated in Figure 3.25. Intersecting the volume of the log with the position of any possible board it is possible to predict the presence of each feature on the virtual board, allowing to know its expected quality.

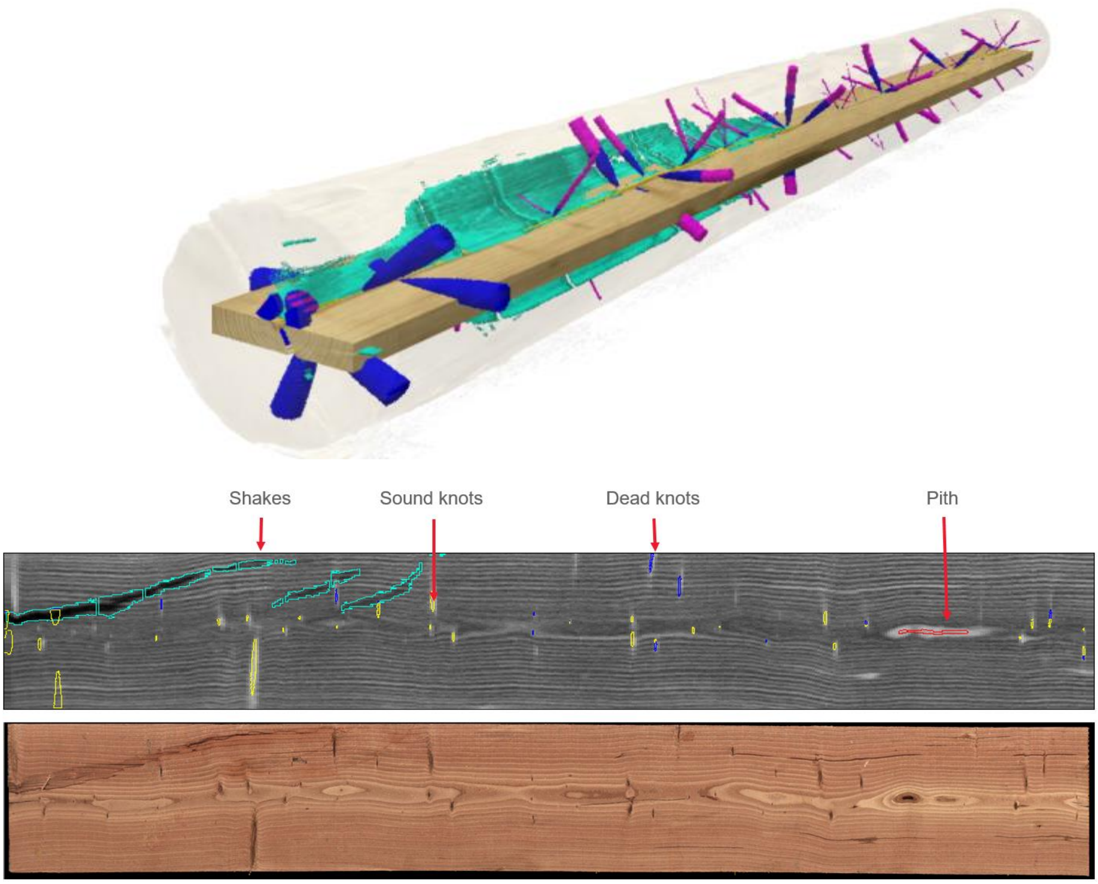

Figure 3.25 Example of virtual board. Visualization of a log with its features extracted from CT images and a board placed in an arbitrary position (top). The top surface of the virtual board computed with the density of the CT image and the position of the features (middle). Picture of the real board sawn in the same position.

The concept of virtual boards allows to simulate different possible production strategies for each single log and evaluating the best one with high precision.

Microtec developed Interopt and Maxicut-pro, two software that can optimize the bucking and sawing process of a log in very short time.

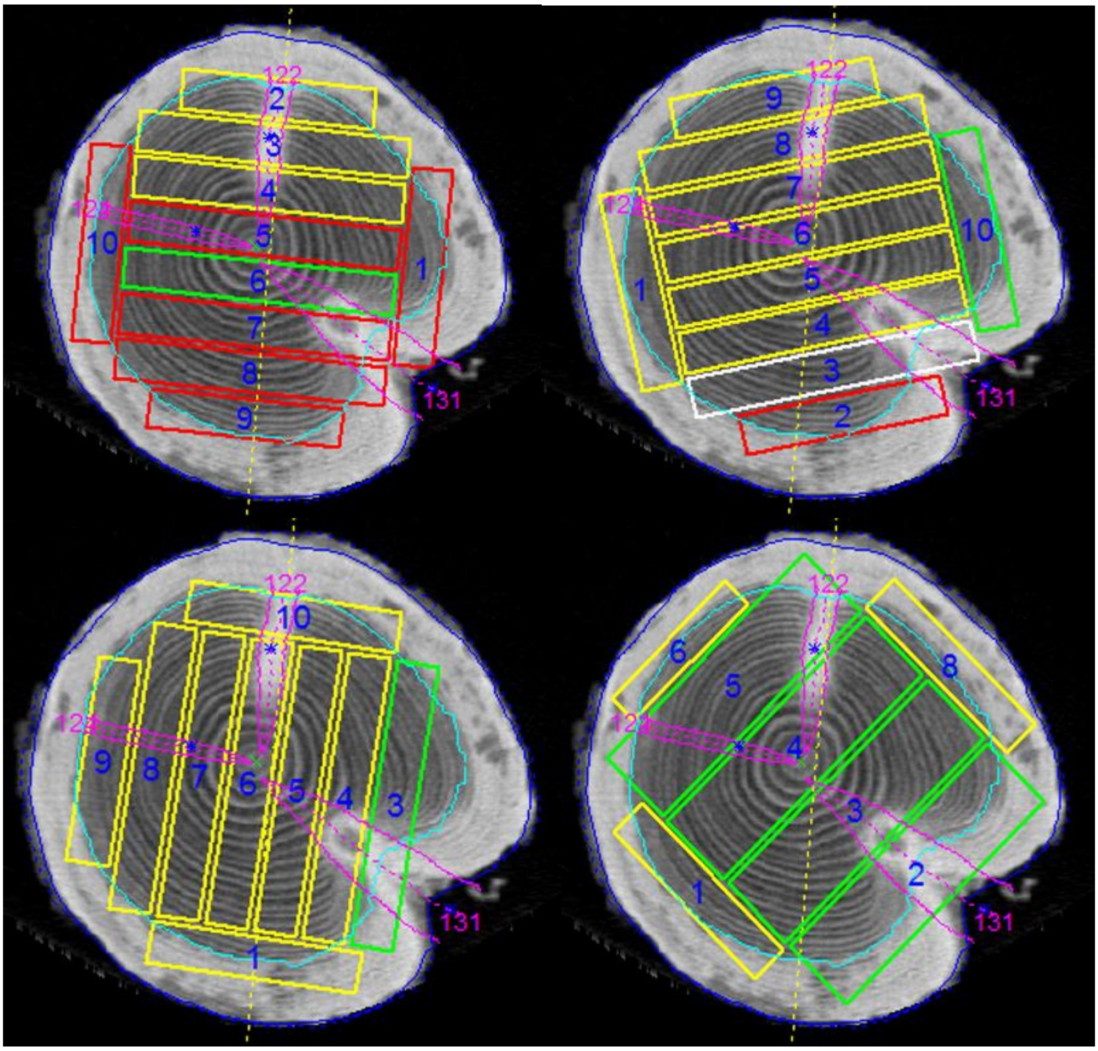

Figure 3.26 Different cutting pattern solution proposed by the optimizer. The colors indicate the quality of the boards estimated from the internal features measured with CT data.

In Figure 3.26 an example of cutting pattern optimization. In maxicut-pro we specified the possible dimension of different products, their prices and the rules to define the quality. The quality estimated by CT Log was reported in green, yellow, red for quality A,B,C respectively. The solution in the top-left is the one proposed by a software optimizing the cutting pattern only based on 3D shape of the log with the angle of rotation decided in function of the curvature of the log (horns-down). In the solution on the top-right the angle was chosen but no internal information was available. In the bottom-left the angle was chosen by the optimizer taking into account the internal quality. In the bottom-right another dimension of product was automatically chosen because it allowed bigger knots in class A, so that for that specific log more advantageous.

Based on the simulation, the sum of the value of the boards in the four solution were respectively 29.11€, 30.53€, 33.81€, 35.36€ with an increment of 21%.

In one study we demonstrated that an increase of value between 4% and 20% can be expected optimizing the rotation angle of the cutting pattern [70]. Other studies [71] observed a mean value increase of about 13% for both Scots pine (*Pinus sylvestris* L.) and Norway spruce (*Picea abies*), if the rotation angle was optimized. The horns-up position served again as the reference. Other studies focused on hardwood and found also an increase of sawmill yield [72] [73]. Other investigations have dealt with the optimal rotational position based on CT data [74] [75] .

Optimization of the rotation angle is definitely only one of the possible optimizations; as explained in the next paragraph, the biometric information present on the raw material allows to use the CT data in order to optimize the whole production chain.

3.10 Production traceability and sawmill 4.0

The internal images of logs acquired with a CT scanner allows also the possibility of a complete traceability of the products along the production line. The idea is to acquire a biometric fingerprint in different points of the line and compare with others to match the correspondent ones [76] [77].

In Figure 3.27 it is sketched the typical production chain in a sawmill. The stems arrive from the forest and bucked into short logs. The logs are sorted in bins with similar characteristics. The logs can remain in the log yard for some weeks until the production requires a specific type of raw material. The logs are sawn into cants and then boards which are sorted according to their quality and stacked to be dried in kilns. After the drying process, the boards are verified for the final grading and trimmed when needed.

The biological diversity of each tree allows to implement a full traceability without the need of any additional tag or label to the products. The CT data acquired when the raw material arrive at the sawmill allows to follow the path of each log and board produced until the final stage.

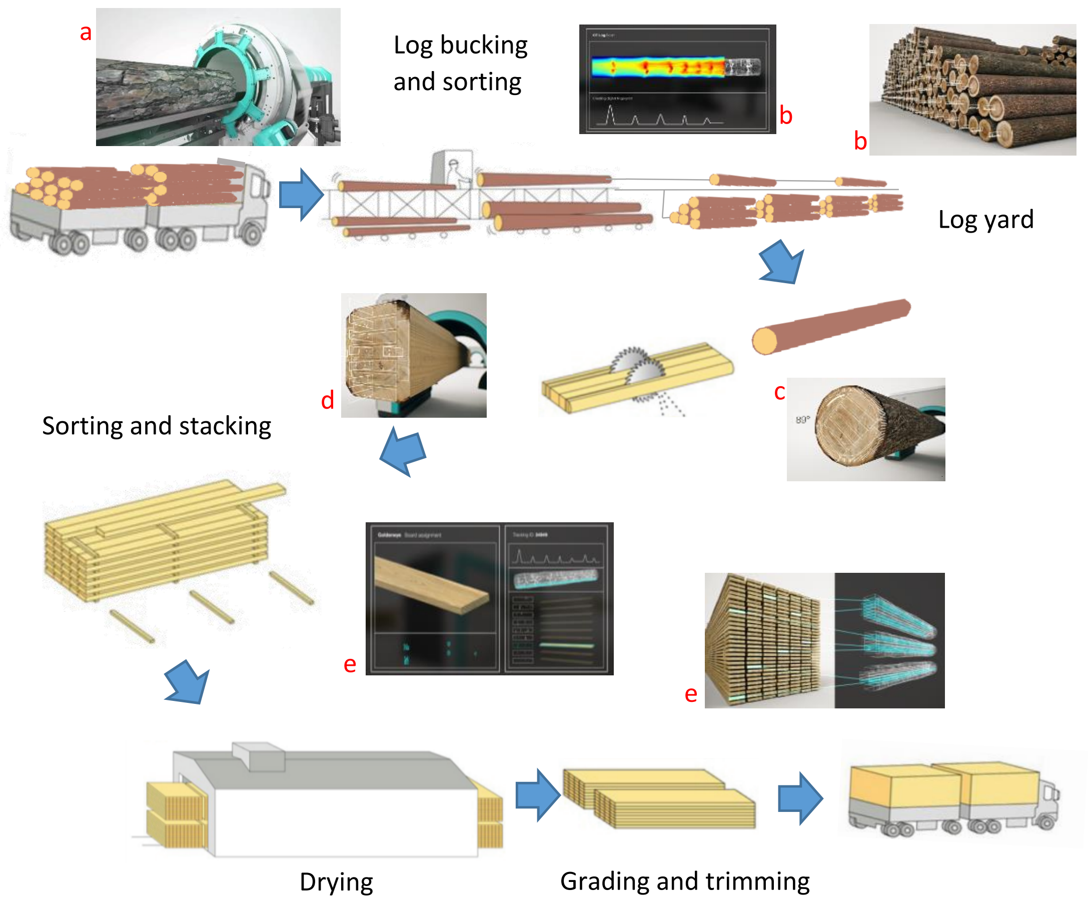

Figure 3.27 Sketch of a sawmill production line with the traceability tools developed in Microtec. Part of the image adapted from Swedish forest industries federation.

When a log is scanned with CT Log (a), a fingerprint of the log is computed, containing the ID of the log and its angular position at the moment of the scan (b). Then the log reaches the sawing line, the log ID and its angle are recognized to cut it as optimized previously (c). After the sawing, the real cutting pattern achieved is verified in order to produce a correct fingerprint for each sawn board (d). The boards are then compared and recognized according to their ID (e).

We are also developing the possibility of using the unique information present on the position of the branches on each tree in order to track the logs from the forest to the sawmill. The information in the forest can be measured with 3D scanners or with suitable devices mounted on the harvesters [78].

Thanks to the full tracking, a lot of final customers buying a furniture could be interested in knowing the exact piece of forest where the wood they bought come from. But the main goal is the optimization of the whole production as suggested by Industry 4.0 and smart production principles. The possibility of simulating different cutting patterns and production strategies in conjunction with the complete traceability of the products gives enormous possibilities. Some examples are:

- Correct evaluation of the raw material: paying correctly the logs for the real final value they produce.
- Evaluating the characteristics of trees from different regions [79], improving the forest management and giving feedback on the best production region or best forest managements in function or the real quality of the products.
- Creating a database of the real content of material at stock allows to do simulations to get the best match between the customer requests and material at stock in order to optimize the production schedule.
- Correct evaluation of the cost of different products in function of the production cost, the availability of the raw material, the amount of waste produced (e.g. board sawn with a specific dimension or dried at a specific moisture content that cannot be sold because they don’t respect the required quality).
- Decision of developing new products in function of the real costs and market value.
- Evaluate and correct the point of the process where the value is lost, e.g. twisted boards for incorrect drying or boars with wane for imprecise positioning at the saws.
- Tuning and optimization of devices with continuous feedback on the quality of the process.
- Improvement of the precision of the scanners. The parameters of the grading and sorting can be tuned in function of the real request of the production or customers.

With respect to the last point, Microtec is participating to the research project “Sawmill 4.0” with Luleå University of Technology (Sweden) Finscan Oy (Finland) and Norra Timber (Sweden). One of the goals of this project is demonstrating how it is possible to reduce the production costs and increase the customer satisfaction introducing a different concept of grading of the wood products. The definition of the characteristics needed for a product of a specific quality is usually defined by rules. Most countries have defined rules to define the maximal knots dimension, wane, pitch pockets and so on are acceptable for a specific quality. In principle the rule-based approach could be substituted by a customer preference-based approach where the customers defines the required quality standard from the selection of a number of sample. The proposed approach would create a stronger link between the customer request and the production simply by asking the customer to grade a number of final products and training the production line to get what is needed [80]

3.10.1 Logs recognition

In a typical sawmill plant, the CT scanner could be placed in the log yard. When logs arrive from the forest, they are measured with a CT Log in order to optimize and pre-sort them in a correct bin. The same CT images are used to create a digital fingerprint containing the ID and the position of the log at the moment of the scan. To recognize the log, a single-source X-ray scanner is used.

The patented procedure [81] consists in using the CT reconstruction in order to compute with ray-tracing the image that would be created by a static X-ray scanner at different angles. As illustrated in Figure 3.28, it is possible to simulate the different rotational position in which the log will pass through the static X-ray scanner.

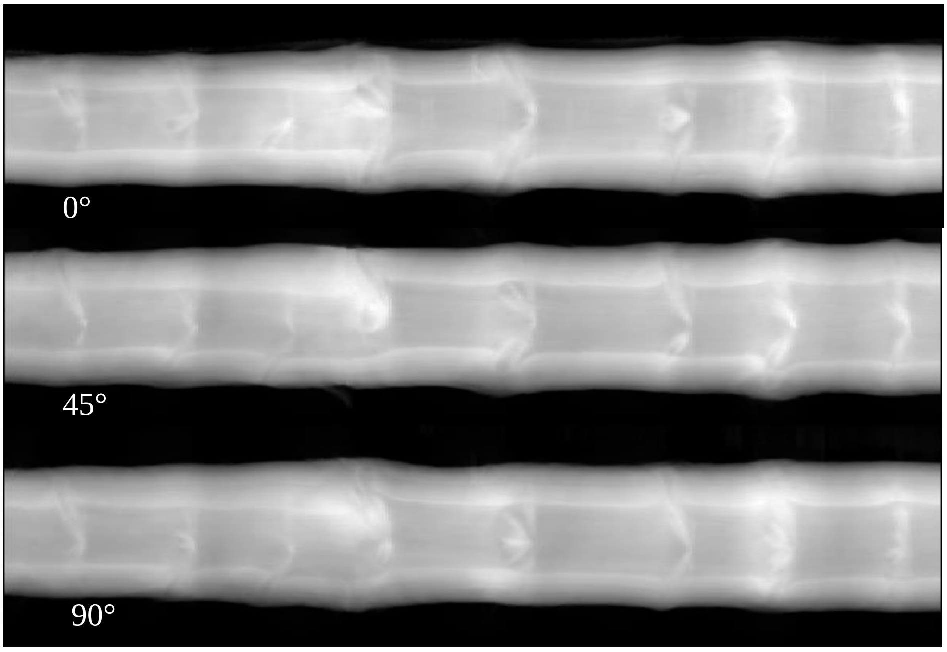

Figure 3.28 example of attenuation obtained from ray tracing of the CT reconstruction at different angles, simulating a static X-ray measurement with the log rotated differently.

The area of the projection covered by the log is identified and only the central part is used in order to avoid changes during the storage. It is important that the same log can be recognized even after months, so that the effects of drying must not affect the fingerprint ID used.

To create a more compact information the average of each slice is computed on the area coved by the log. A database of millions of identifiers are stored and compared with new X-ray scans.

During a test, 262 logs were scanned with CT Log and separated respect to the rest of the production. Their fingerprint ID was added to the database of the sawmill containing about 200.000 logs and the logs were left in the log yard. After one week the logs were scanned with a Logeye 302 X-ray scanner for fingerprint recognition. One of the logs was broken during the transportation, one was not recognized by the system, all the other logs were correctly recognized as part of the separated batch of logs. So that 99.6% of the logs were recognized and no match was wrong.

3.10.2 Rotation recognition

Another important piece of information needed when the log arrives at the sawmill is its angular position relative to its position when it was CT scanned.

The measurement of the relative angle is performed using the same virtual projections introduced in the previous paragraph and shown in Figure 3.28, with a patented procedure [82].

The projection measured with the X-ray scanner is compared with the virtual projections at different angles. The area of the projections covered by the log is stretched in order to obtain an image having always the same size; a high pass filter is applied in order to avoid differences due to drying of the sapwood and the sum of the difference of the pixels is computed.

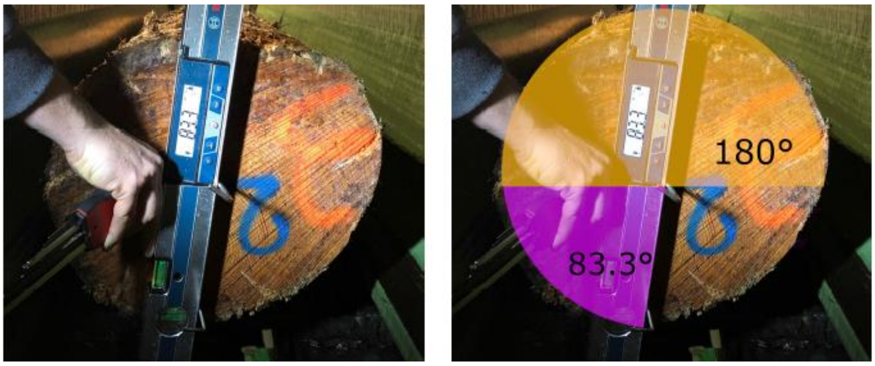

Figure 3.29 manual verification of the angle of a log during the test

To verify the precision of the system in one experiment, we used 13 logs and marked with two holes in order to have a reference angle visible also in the CT images. Two manual measurements were taken, before and after the passage of the log in the scanner, and the average was computed. As reported in Table 5, the average error was 1.8°, the standard deviation 1.4°.

scan order	fingerprint angle	manual angle 1	manual angle 2	manual angle	difference
1	320.1	314.8	319.6	317.2	2.9
2	350.3	350.2	353.7	351.9	1.6
3	207.9	208.8	208.4	208.6	0.7
4	17.8	21.7	21.2	21.4	3.6
5	348.1	349.7	349.8	349.7	1.6
6	203.9	204.1	204.8	204.5	0.6
7	237.9	239.7	239.7	239.7	1.8
8	64.5	66.9	66.1	66.5	2.0
9	175.8	175.9	176.0	175.9	0.1
10	19.8	14.9	14.3	14.6	5.3
11	1.3	1.4	0.8	1.1	0.2
12	196.3	197.4	198.2	197.8	1.5
13	13.9	15.1	15.4	15.3	1.4
			average of difference		1.8
			standard deviation		1.4

Table 5 Experiment on the precision of the angle measurement with X-ray fingerprint.

3.10.3 Movement and rotation measurement and control

As mentioned in the previous paragraph, optimizing the angle is useless if it is then impossible to position the log precisely before sawing. In order to improve this procedure, I developed a system called True Spin which measures the movement of the log during the passage in front of the cameras (Figure 3.30). Details of this research are omitted for secrecy reason.

Figure 3.30 Two views of the structure of the Microtec True Spin scanner.

log diameter (mm)	initial manual angle (°)	final manual angle (°)	manual rotation angle (°)	rotation measured with True Spin (°)	difference (°)
240	5.8	4.3	1.5	2	0.5
240	16.5	10.3	6.2	6.3	0.1
240	12.2	13.5	-1.3	-1.3	0
240	-5.4	-2.3	-3.1	-3.4	-0.3
240	3.9	3.5	0.4	-0.3	-0.7
240	10.8	8.5	2.3	2.3	0
240	24.7	20.5	4.2	4.7	0.5
240	25.2	23.2	2	1.4	-0.6
240	28.5	28.8	-0.3	-0.6	-0.3
170	21.3	14.2	7.1	7.5	0.4
170	22.8	24.4	-1.6	-2.6	-1
170	24.5	22.7	1.8	1.9	0.1
170	13.1	17.1	-4	-4.4	-0.4
170	18.1	23.3	-5.2	-5	0.2
170	29.5	12.4	17.1	17.6	0.5
170	13.9	21.4	-7.5	-7	0.5
170	-34.5	-31.5	3	3.2	0.2
				standard deviation:	0.46
				average:	-0.02

Table 6 Results of a test of the measurement of the movement of the log with True Spin. Only the rotation along the main axis is reported.

In the experiment reported in Table 6, we measured 17 logs with different diameter during the passage under the scanner on a chain conveyor. The logs were stopped and the angle of a marker line was measured manually with respect to a vertical reference. The manual angle was measured before the log entered the scan area ("initial manual angle" in the table) and after the passage ("final manual angle"). The difference of the angles was then compared with the rotation measure by the True Spin system. The standard deviation of the error was 0.46°.

3.10.4 Cant analyzer

After the rotation, the log is usually passed in a chipper-canter machine which creates four flat faces on the log producing a so-called cant. In order to optimize the further processing and tracking, it is important to have a device able to verify the real operation executed, i.e. measuring exactly how the log was sawn in terms of positioning and rotation.

A simple system I implemented is based on a 3D measurement placed just after the chipper-canter made with four lasers and four cameras. One scanner placed after the chipper-canter is able to measure the shape of each slice of the cant. Unfortunately, in that part of the production line the cant can move sideways and rotate during the measurement, so that it is not possible to collect a reliable global shape of the cant, but only independent measurement of single slices.

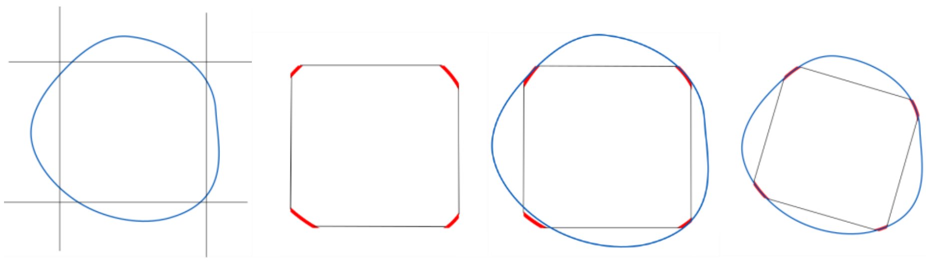

Figure 3.31 Illustration of cant analyzer principle from left to right. The log optimal sawing pattern is decided (1), the log is sawn and a cant is produces with 4 flat surfaces and 4 wanes (2), the shape of the cant is superimposed to the log shape but doesn't fit precisely (3) applying a rotation it is possible to fit precisely the shape of the cant and the log.

However, each slice contain a lot of information. As illustrated in Figure 3.31 it is possible compare on each slice the measured shape with the expected shape in function of different sawing positions and then choose the sawing pattern that better fits all slices. Applying the computed sawing pattern to the original log data it is possible to correct the model of the virtual boards accordingly, as illustrated in Figure 3.32. I developed another method to monitor and improve the procedure of sawing the logs, the approach is presented in a patent (where also other applications of the same principle are described) [83].

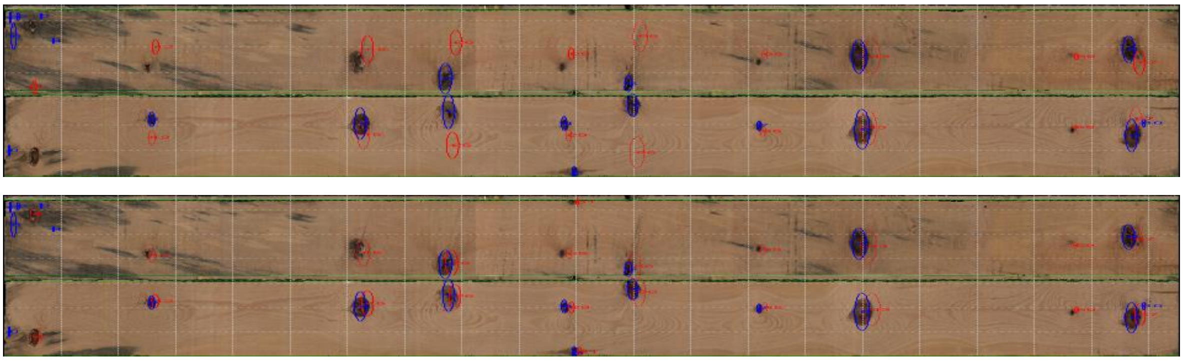

Figure 3.32 Pictures of the main sides of a board with the knots detected with a board scanner (in blue) and from CT virtual boards (in red). In the top picture the expected cutting pattern was used to create the position of the knots in the virtual board, in the bottom picture the cutting pattern was adjusted using the information of the cant analyzer.

3.10.5 Board fingerprint

The next necessary traceability step is to be able to trace each board back to the log from which it was cut and from which position. In other words, match the virtual board with the real one.

The method I developed with other colleagues [84] is based on the comparison of the position of the knot in the virtual and real board. A vector F of four features is considered for each detected node: two position coordinates x, y and two dimensions dx, dy. For each pair of knots A and B, we compute a standardized Euclidean distance as defined in (3.1) where Si is the standard deviation of the i-th feature of the feature vector F.

$$d_{AB} = \sqrt{\sum_{i=0}^{3} \frac{(F_i^A - F_i^B)^2}{Si}} \tag{3.1}$$

Then we compute a matching score according to definition (3.2)

$$M_{AB} = e^{-d_{AB}{}^2} \tag{3.2}$$

Summing the scores of all the possible knot pairs, we get an overall matching score. During an experiment, 1200 boards were scanned with a Microtec Goldeneye 900 board scanner and they were compared with the virtual boards computed with the CT Log data. 824 of them were correctly matched. Then we corrected the virtual boards with the information from the cant analyser and the number of correctly matched boards was 896, equal to 74.7%.

3.10.6 Fitting of CT data in a debarked log

In sawmills, when a short log is cut, it is important to have an accurate measurement of its external shape. The measurement is both necessary for good optimization based on external shape (which is the basis for good optimization that also considers internal quality), and for proper log handling within the cutting line.

In some sawmills configurations, the CT Log scanner measures the logs in the log yard with bark on them. The logs will be debarked and cut in sawmills at a later time.

Although algorithms have been developed to give a good estimation of the under-bark shape of the log, the optimization calculated on this estimated shape could be not sufficiently accurate.

The measurement of the debarked log allows a more accurate computation of the dimensions, which also takes into account ruptures or consumption due to handling and debarking steps that cannot certainly be evaluated on the basis of the initial tomographic image.

We therefore implemented a method to combine the knowledge of the internal quality obtained by CT with the shape measurement made before cutting, in order to optimize the log with the best information. The method was based on aligning the 3D measure at the sawmill with the over-bark and under-bark measurement taken in the log yard to get a model including both information. In this way, we create a new log model already aligned in the cutting reference system that can be optimized by exploiting the internal quality.

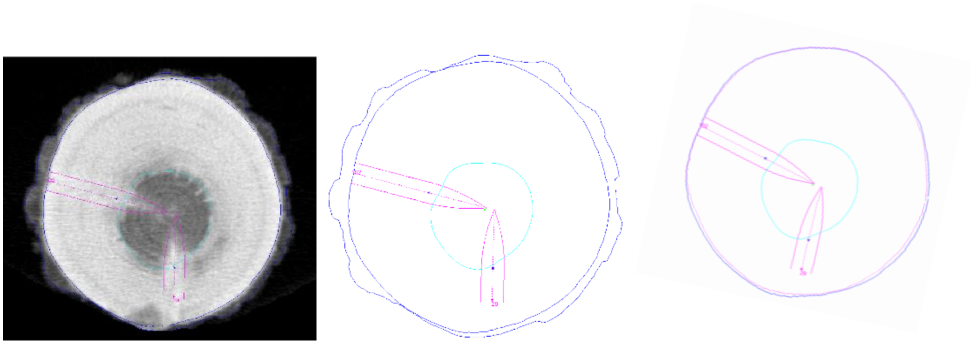

Figure 3.33 CT scan with extraction of overbark and underbark shape and internal features. With density (left), only the extracted model (middle), virtually removing bark (right).

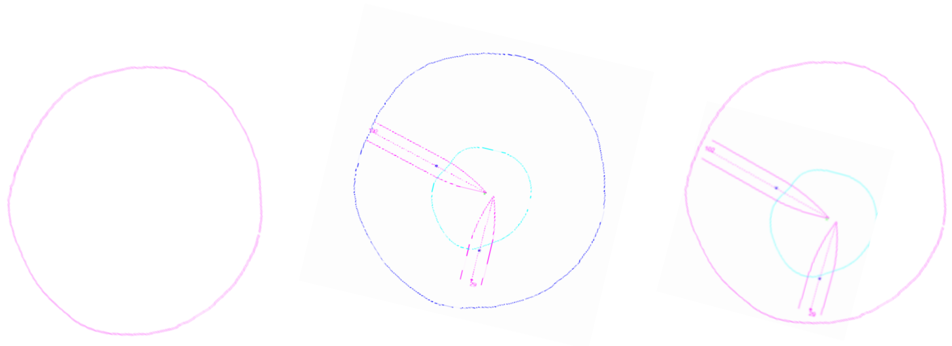

Figure 3.34 Shape acquired from a scanner with laser triangulation system (left). CT model rotated and aligned to the previous shape (middle). Final model with shape from standard scanner and CT features reported (right).

3.11 Industrial installations

CT Log has been installed in 10 sawmills in the world. . In the first plants it was mainly used for better sorting of the logs in function of the production requirements. For example the sawmill Siat-Braun in France scans long stems up to 20m long to optimize the bucking into short logs and sort the logs for the production of different products.

HIT holzindustrie Torgau, in Germany, was the first plant where maxicut pro optimization was applied. At Idaho Forest Group in USA we implemented a log fingerprint with big number of logs in memory because the logs remained in the log yard for weeks after the CT scan and before reaching the sawmill. On the opposite side, at Norra Timber (Sweden) the scanner is placed just before the sawing line. At Piveteaubois (France) we implemented a database storage of all the logs and their cutting pattern solutions in order to optimize the production schedule. In SCA (Sweden) we are implementing a complete tracking of the pieces along the production.

Figure 3.35 Some CT Log installation: from top left Siat-Braun (France) Arauco (Chile) Fiskarheden (Sweden) Piveteaubois (France).

Chapter 4

Industrial tomography for the food industry

4.1 Mito: a smaller industrial CT scanner

CT Log was a disruptive technology in the sawmill industry, winning many awards [85] and introducing the possibility of innovative organization in the process. The same technology can clearly be applied to other production sectors, particularly in those with high variability in the raw material.

Based on the experience accumulated with CT Log and experimenting alternative solutions, I started the development of an innovative tomograph with performance suitable for other industry markets. Respect to the sawmill industry, most of the industrial manufacturing plants require a slower speed of scan. On the other side, the low resolution of 10mm in longitudinal direction is meaningful when scanning wood logs where most defects are aligned in the longitudinal direction, but it would be useless in many other applications. For this reason a resolution of 0.5 mm was chosen for all directions. Furthermore, the field of view was reduced to 250 mm for the first version of the scanner. In Table 7 it is summarized the main parameters of the scanner.

Scan speed	1-40 m/minute
Operating times	24/7 continuous operation
X-ray tube voltage	80-160 kV
Field of view diameter	25 cm
Transversal resolution	0.5 mm
Longitudinal resolution	0.5 mm

Table 7: technical specification of Mito 250.

A Katsevich exact cone beam reconstruction algorithm similar to CT Log has been implemented so that it is possible to process the images of the pieces immediately after the passage in the scanner and control the production accordingly.

One of the most important aspects of this type of scanner is the flexibility. It is possible to use it in a wide range of speed, depending on the production request and the dimension of the objects. Smaller objects can be scanned at high speed while bigger objects, which would require longer exposure to X-rays in order to avoid high noise in the reconstruction, can be scanned at slower speed.

Another version with 500 mm of field of view and higher resolution has been already installed at Luleå University of Technology for scientific use (see Figure 1.2). The design of another version, able to reach 300 m/min for wood board inspection, has been started.

For industrial secrecy only few details of the structure of the scanner are given in this thesis.

Even if a couple of installation of Mito are in the wood industry, in the next paragraph I will illustrate some details of the application to the food industry. Among other possible industrial markets, the food market has been selected as ideal application because of its requirements.

4.2 Glass in glass

The detection of small pieces of glass in glass food containers is a major problem for many manufacturers. In the market there are X-ray based systems with one, two, three and even four sources to obtain images at different angles and to be able to detect the presence of foreign bodies even in the most difficult places. Obviously, even four views cannot match the capability of a CT scanner that captures hundreds of projections from all angles and produces a global image that summarises them all.

One of the first installation of Mito was at Cooperativa Latteria Vipiteno (Italy). All yogurt jars are measured at 20 m/min verifying the possible presence of foreign bodies and removing automatically all the discarded jars.

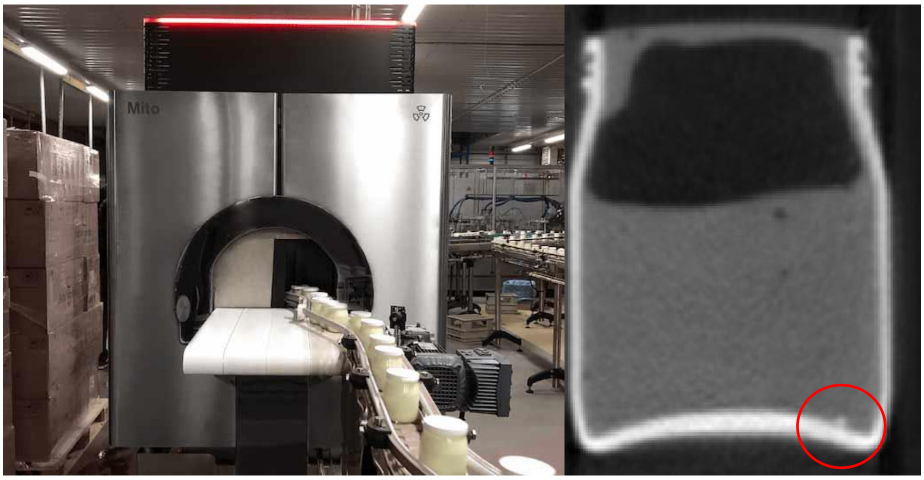

Figure 4.1 The installation of Mito at Cooperativa Latteria Vipiteno (left) scan of a jar with a small contaminant on the bottom (right)

4.3 Bread

Another installation of Mito was at the bakery Dr.Schär (Figure 4.2) where the customer was interested in the automatic measurement of the air bubbles. In some production the bubbles were too big, not acceptable for the consumers. The continuous feedback from the scanner allowed to avoid selling incorrect products and to optimize the production parameters.

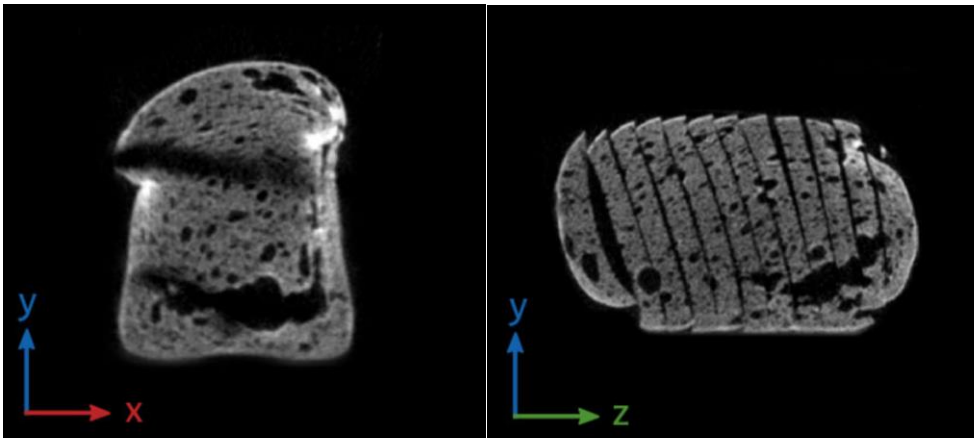

Figure 4.2 CT images of bread. An automatic detection of the air bubbles has been implemented.

4.4 Measurement of weight and volume

An interesting application of inline tomography is the possibility of measuring the volume and weight of specific parts of a product. To make an objective assessment of the accuracy of the system, samples were prepared with paper cups filled with a portion of apricot jam. Jam was chosen instead of water to take into account the fact that the complex shape makes the volume estimation more difficult using traditional methods.

Twelve samples were prepared with a quantity of jam ranging from 3.5 g to 7.7 g (Figure 4.3). Each sample was measured 10 times with Mito 250 during a run at 12m/min.

Figure 4.3 Picture of some samples of jam.

A simple segmentation algorithm of the acquired images was implemented and two types of analysis were performed: volume and weight. The volume was calculated as the number of voxels above a certain threshold multiplied by the voxel volume. The weight measurement was calculated as the sum of the density of the segmented voxels multiplied by the volume of each voxel.

As a ground-truth, the weight of the jam was measured with an electronic scale with 0.1g resolution. The volume of jam was calculated by dividing the weight by the estimated density of 1.102 g/cm3.The results are presented in Table 8, Figure 4.4 and Figure 4.5. As can be seen, the accuracies obtained are comparable with the accuracies of ground-truth measurements. A very interesting aspect is the fact that this method of measurement can be applied for the measurement of volume and weights of objects of undefined shape by means of inline tomography. Even more interesting is the fact that this measurement can be accomplished while the samples are part of a more complex product inside a packaging.

	Volume	Weight
Repeatability (stdev)	0.7%	2.3%
Difference with scale (stdev)	1.8%	2.9%
Difference with scale (stdev)	0.12cm^3	0.17g

Table 8 Precision of the measurement of the weight of a small amount of jam between 3.5 and 7.7gr. Measurements are based on scans at 12m/min with Mito250.

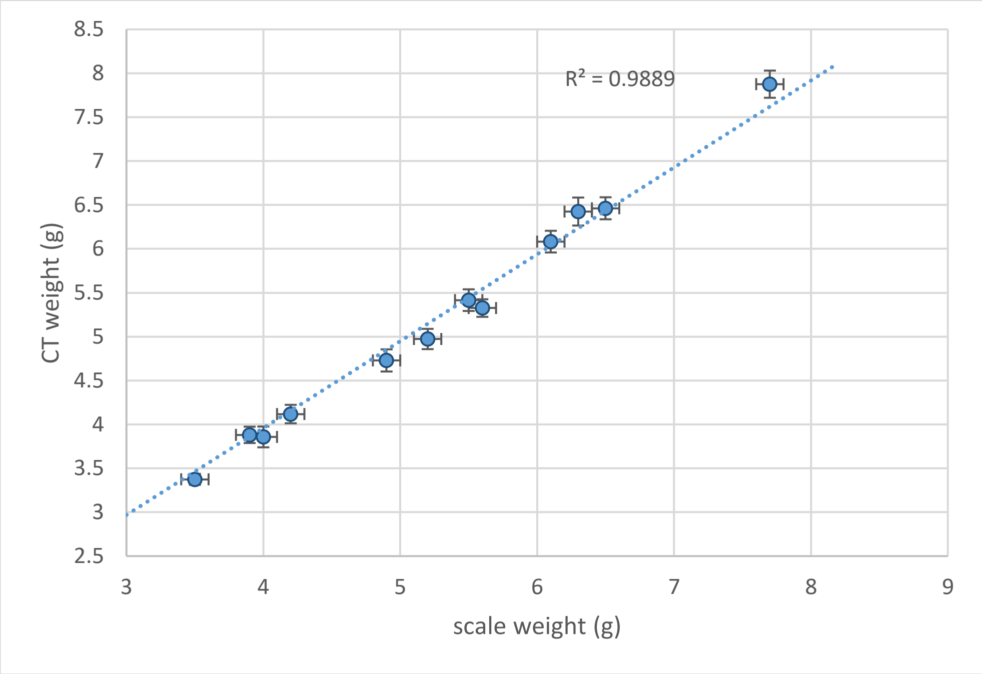

Figure 4.4 Precision of the measurement of the weight based on CT data. The horizontal error bars consider the precision of the scale, the vertical error bars indicate the standard deviation of each sample over ten measurements.

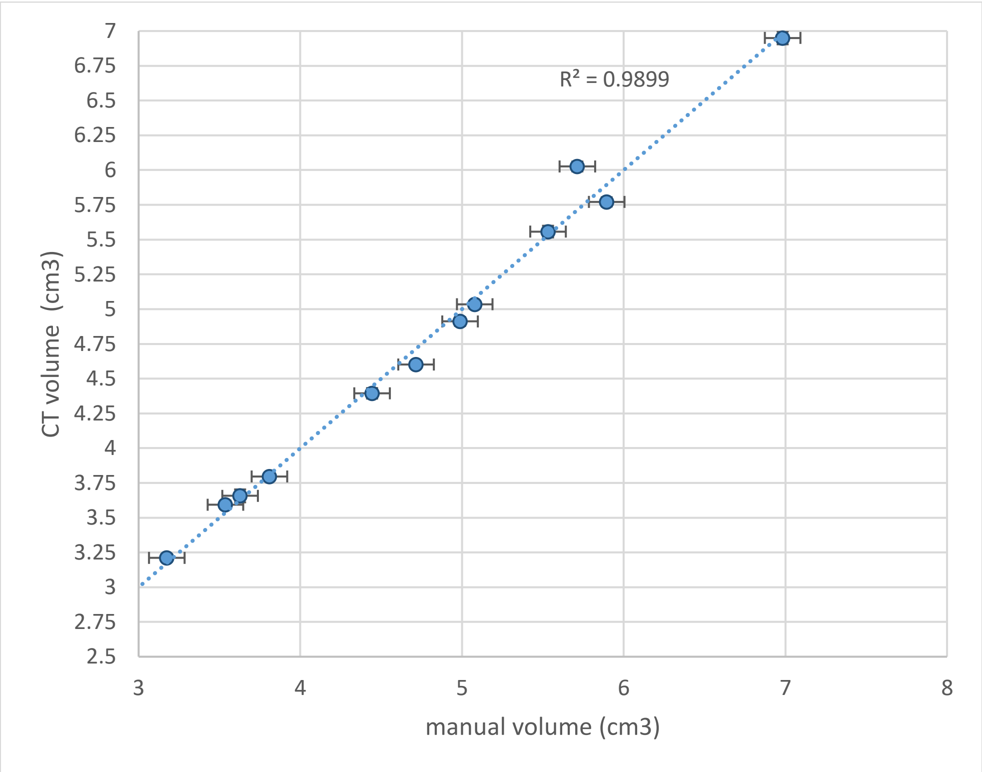

Figure 4.5 Precision of the measurement of the volume based on CT data. The horizontal error bars consider the precision of the scale, the vertical error bars indicate the standard deviation of each sample over ten measurements.

4.5 Detection of correct production

Many food products are composed of different parts that must be assembled correctly. An example is a container of chocolate ice cream in which there must be a certain number of chocolate pieces mixed with ice cream and cherries: these pieces must be of a certain size and spaced correctly. Another example is a cake which must have the right amount of cherries, sponge cake and cream positioned correctly. The same applies to pizzas, snacks and so on.

A lot of ingredients have a characteristic density that allows them to be easily identified by tomographic investigation. By means of a threshold on the density measured by the CT scanner, it is possible to identify in which areas the various components are located and their size. It is then possible to divide compliant products from non-compliant products or products to be corrected.

As well as rejecting non-compliant products, this system can generate feedback to control production, either automatically or through operator intervention. For example, if too much chocolate is put in an ice cream, you can automatically reduce the amount of chocolate in the next one or request a verification of the machinery.

In Figure 4.6 it is shown the segmentation of different parts of an ice cream to verify its compliance and give feedback to the production.

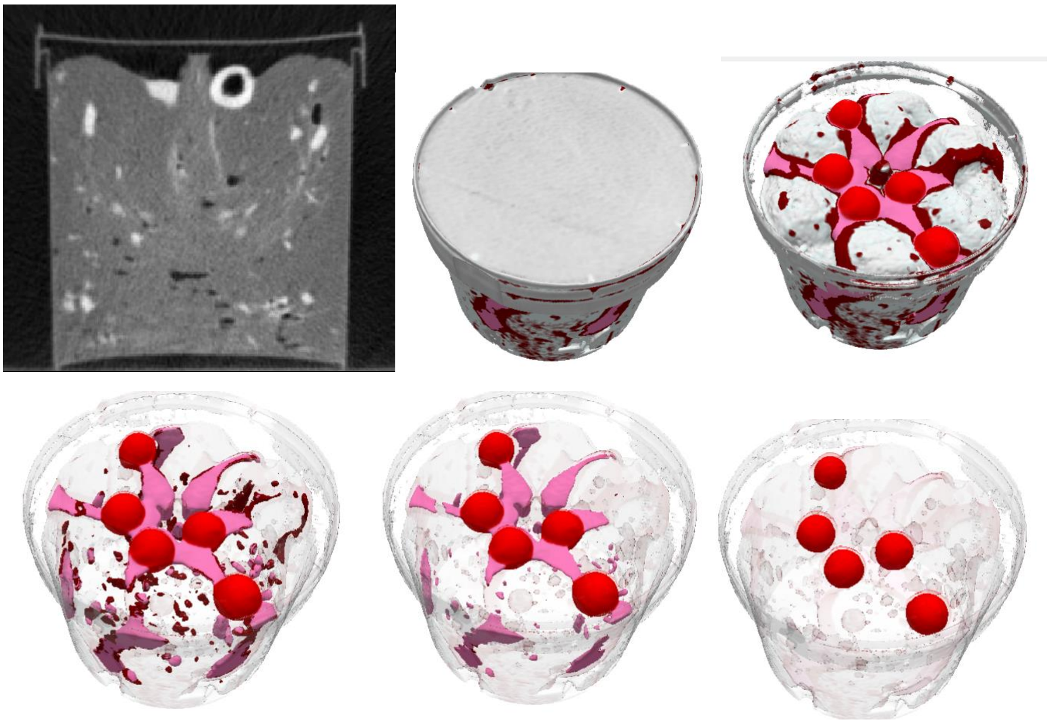

Figure 4.6 Slice of the CT scan of a cup of ice cream (top left) and render of different stages of segmentation in the different components.

Another useful application is shown in Figure 4.7 where the CT scan is used to verify the correct closure of jam jars. The advantage of CT measurements rely also on the fact that scans can be done after the packaging, verifying the products inside the cardboard package [86]. In Figure 4.7, Figure 4.8, Figure 4.9, Figure 4.10, Figure 4.11 more examples of scans for food applications can be seen.

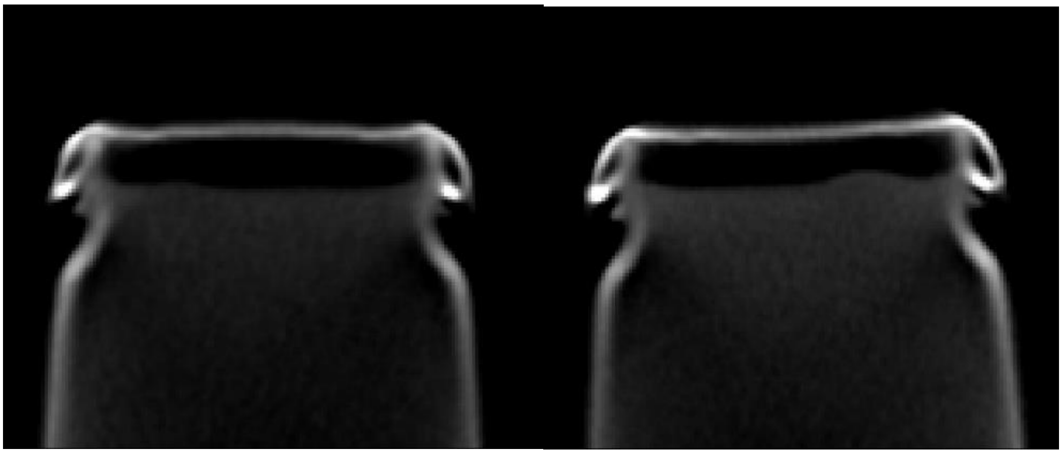

Figure 4.7 CT scan of two jam jars. In the one on the left, the shape of the cap indicates that the sealing of the cap is not correct.

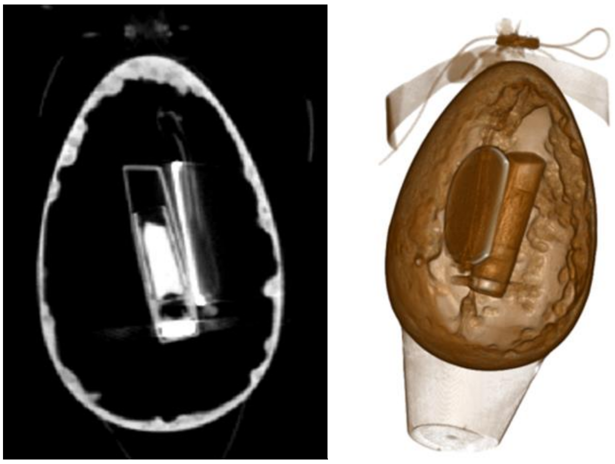

Figure 4.8 Automatic check of the content of Easter eggs. CT slice (left) and render (right).

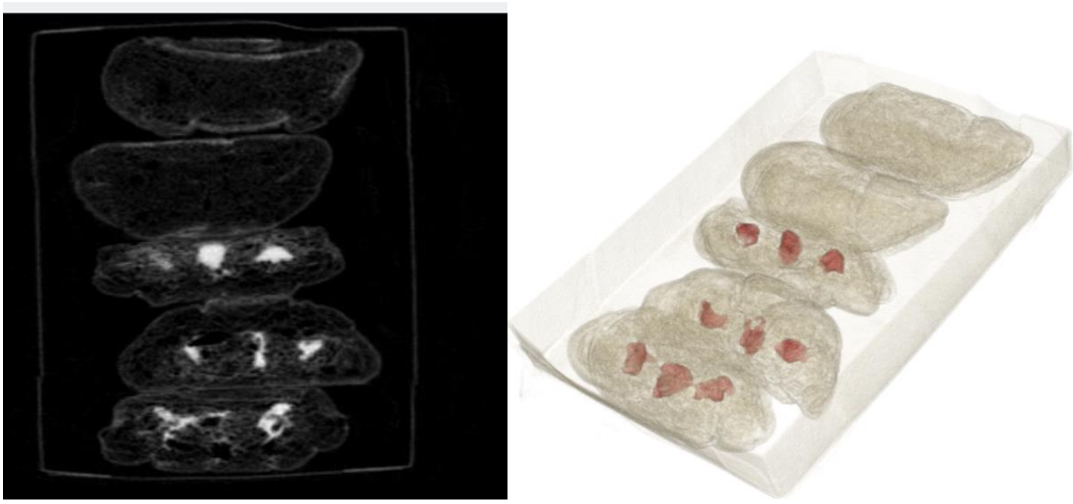

Figure 4.9 Verification of the presence of jam in croissants. CT slice (left) and render (right).

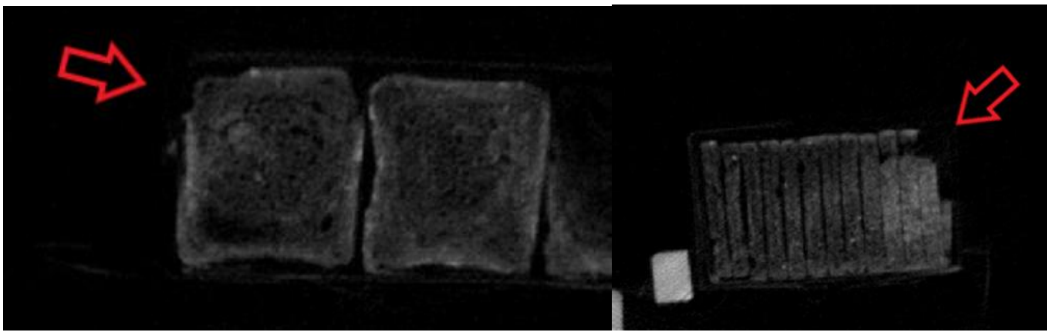

Figure 4.10 Example of detection of broken rusks inside a packet.

Figure 4.11 Rendering showing in green the automatic detection of pieces of stones in olives.

4.6 Apples

During a cooperation with Wageningen University and research, we tested the possibility of detecting the presence of codling moth larvae in apples using in-line computed tomography. Larvae at different stages were inserted in apples and the apples were scanned with a Mito 250 at the speed of 12 m/min, equivalent to a potential production of 240 fruits/min. Figure 4.12 shows the scanner during the scan of apples; Figure 4.13 show a slice of the tomographic image where the tunnels are visible because of their lower density.

Figure 4.12 Mito 250 scanning apples

A computer vision algorithm has been developed for the automatic detection of the infected apples. Applying that algorithm, all the apples infected with larvae at higher stages and most apples with larvae at the initial stage were correctly identified [87].

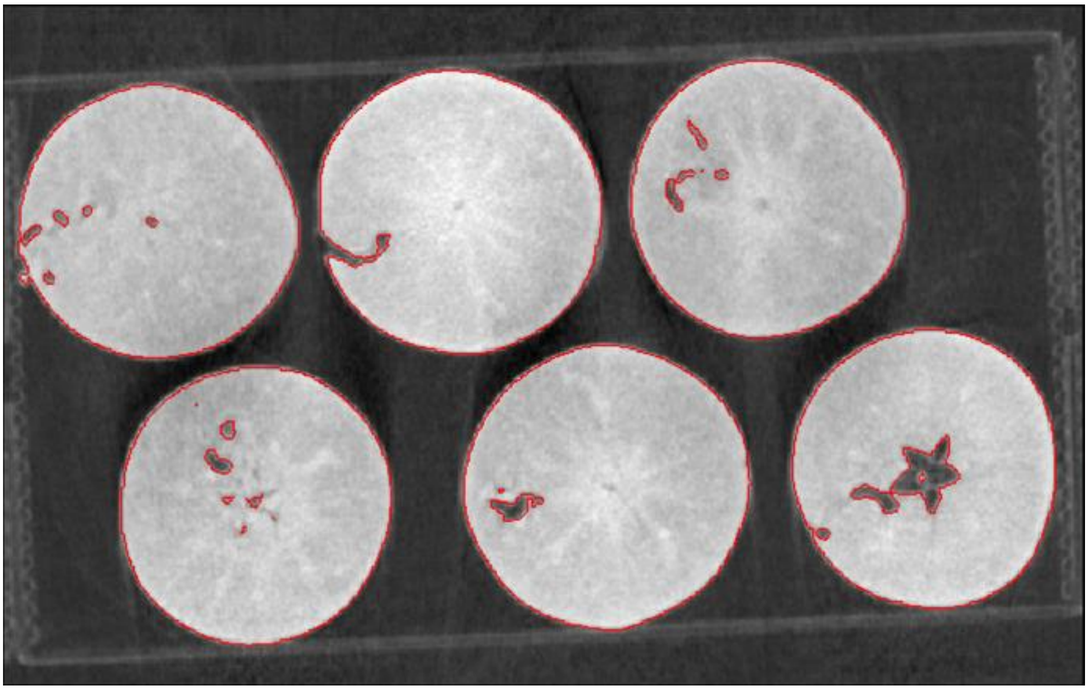

Figure 4.13 CT scans of apples with larvae. In red highlighted areas with lower density can be seen.

Chapter 5

Innovative in-line industrial X-ray scanners

In a considerable number of applications, traditional technology used to realize CT scanners is not usable. Cost, space needed, type of products suggest in some cases that the classical way is not possible. In this chapter I will introduce different solutions, some of them have already been implemented in commercial products and others are still in development.

One patented application [88], developed in cooperation with the company Sacmi Spa, used an X-ray scanner to determine accurately the density of compacted powder for the production of ceramic tiles. Measuring the density of a layer of known composition and dimension is a simple problem using X-rays, but in this kind of application a critical issue was the ripple in the high voltage generator that affected the measurements. The solution was the introduction of an additional sensor in an area where no object was interposed between the source and the sensor: that signal measured directly the ripple of the source, allowing to compensate for it and generate a precise measurement.

In other patents I proposed solutions regarding an improved X-ray shielding for CT scanners [89] and a novel type of x-ray sensor for tomographic application [90].

5.1 Q-eye XP X-ray scanner for fruit sorting

Microtec has also a fory-year-long experience in the industry of fruit sorting. Before packaging, the fruit must be individually checked and sorted according to weight, size, colour and quality to form homogeneous packages. This process is usually carried out automatically using sorting machines that place the fruit individually on conveyor systems to be analysed by non-contact measuring instruments and then sorted into packages, similar to the one in Figure 5.1. Microtec has been developing and producing systems based on multi-sensor technologies for this type of machinery since 1980.

Introducing X-ray measurement in the fruit sector was deemed interesting in order to detect and sort fruits affected by different types of defects but the influence of the shape in the measured signal made the project difficult.

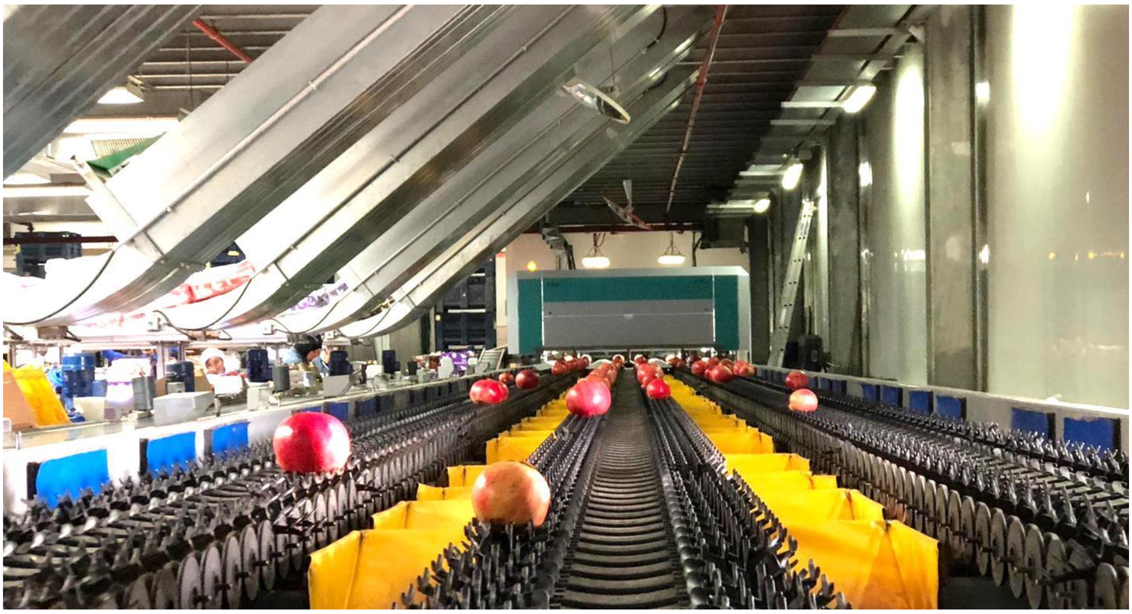

Figure 5.1Fruit sorting machine

As explained in chapter 2.3, the signal measured with a calibrated X-ray scanner is proportional to the integral of the attenuation along each beam. Different diseases and parts of fruits (e.g. the seeds) have a different density and attenuation respect to the fruit flesh, so that can be detected with X-rays. The problem is distinguishing the signal variations due to a region with different density with respect to those due to the shape of the fruit.

In order to solve the problem, as explained and protected by our international patent [91], we extrapolated the shape of the fruit from the X-ray projection and used the shape to compute the average density instead of the integral of the density.

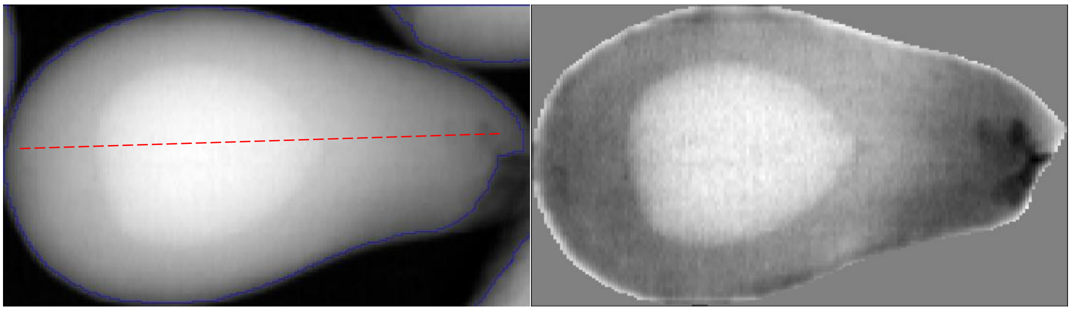

Figure 5.2 Example of X-ray projection of an avocado with the shape highlighted in blue and the axis of symmetry in red (left); the average density image estimation computed from the same projection (right)

On the left side of Figure 5.2, the X-ray projection of an avocado is shown. The blue line highlights the outer shape of the fruit in the projection extracted with a threshold. The red line indicates the axis of symmetry of the fruit projection shape. The hypothesis is that the symmetry axis in the 2D projection is the projection of the 3D axis of symmetry of the fruit. Under this hypothesis, it is possible to compute the 3D shape of the fruit; this will allow us to compute the length of the fruit crossed by each beam. Dividing the absorption by the length it is then possible to convert the projection in an image containing the average density instead of the integral of the density. An example of the result of the computation is shown in Figure 5.2 (right).

The proposed processing of the image allows to increase the contrast of the different features inside a fruit (e.g. rotten parts), the dimension of the seed or the presence of empty space between the seed and the pulp (Figure 5.3)

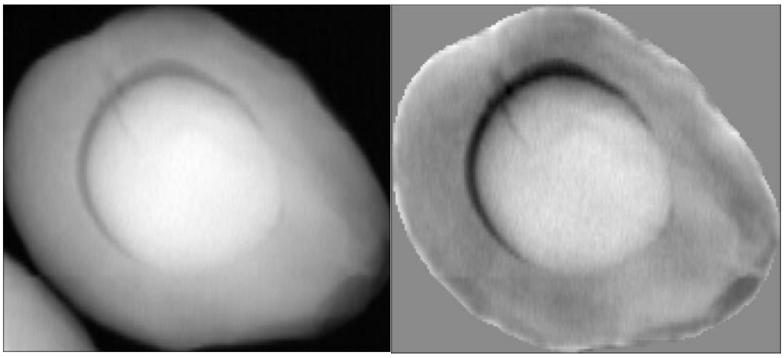

Figure 5.3 X-ray attenuation (left) and average density estimation (right) of an avocado where it is clearly visible the detachment of the pulp from the seed.

In Figure 5.4, it is visible the presentation at a trade show of the award-winning industrial X-ray scanner implementing the procedure exposed.

Figure 5.4 Q-eye XP, industrial scanner for fruit sorting presented at a trade show.

5.2 CT based on free rotation of the samples

In 5.1 I explained a solution for the in-line X-ray inspection of fruits, but a CT scanner would give much more internal information with respect to a simple X-ray. A typical medical, luggage or inline scanner has a rotating gantry where the X-ray source and the sensor rotate around the measured object. One critical part of the scanner is the dimension, the cost and the complexity of the gantry. Positioning a gantry around a conveyor for a fruit sorting machine, like the one in Figure 5.1, would be very complex and expensive.

A lot of micro-CT devices have a static source and sensor and the sample is positioned on a rotating table so that it moves with a circular or spiral trajectory around an axis. This solution is not feasible in a sorting machine because on each line are typically processed ten fruits per second. Grabbing, positioning and rotating the fruits at that rate would be very complicated.

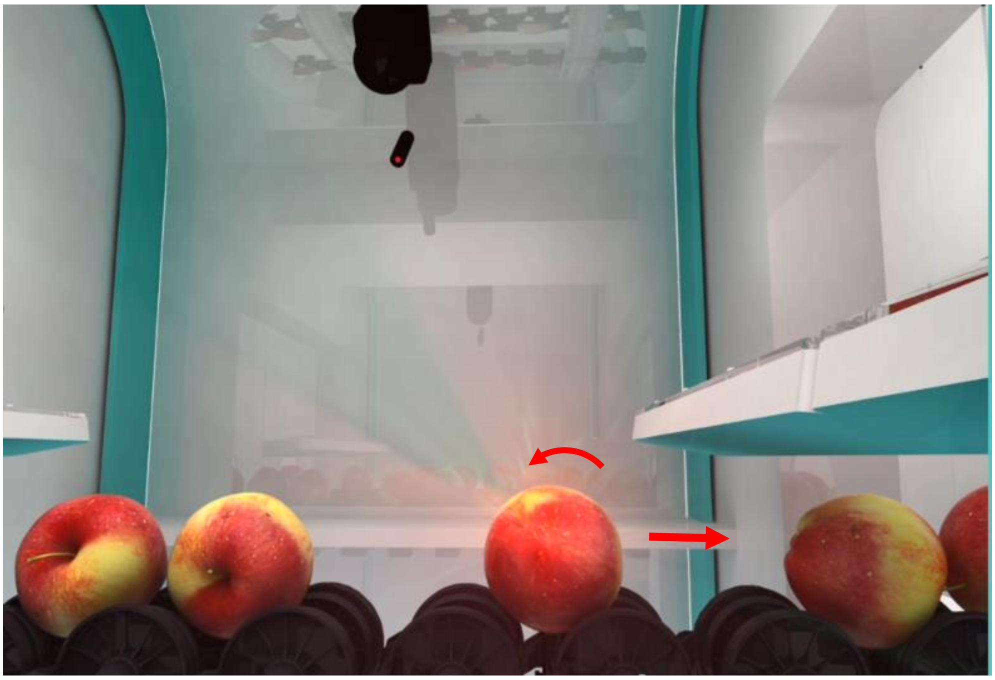

Figure 5.5 Render of the measuring area of a sorting machine. The fruits are positioned on a conveyor made of rolls to rotate them during the transportation in front of the cameras.

As visible in Figure 5.5, in most sorting machines the fruits are already rotated; the fruits pass in a measuring area where different cameras acquire pictures of the external surface. In order to be able to measure the whole surface of the fruit, they are positioned on rollers that rotate the fruits during the transportation. Typically the scan region is 50cm long and in that area the fruits have to make more or less one revolution. The problem is that the rotation is definitely not precise: it depends on the diameter and the shape of each fruit, on possible interaction of the stem with the rolls and so on.

Most commercial systems simply acquire and analyze the single pictures; if a defect is detected in any picture, then the fruit is discarded. The average color is the average of the color of the single images. We patented a system able to produce images that are representative of the surface of the fruit measuring and taking into account the real movement of each fruit [58]. The method is described in Figure 5.6: a structured light is used in order to measure a depth map on each frame (a). The optical flow is computed by comparing pictures from adjacent frames (b). Using optical flow and 3D information, the rigid body motion between each pair of pictures is computed creating a complete 3D and texture model merging all views (c and d).

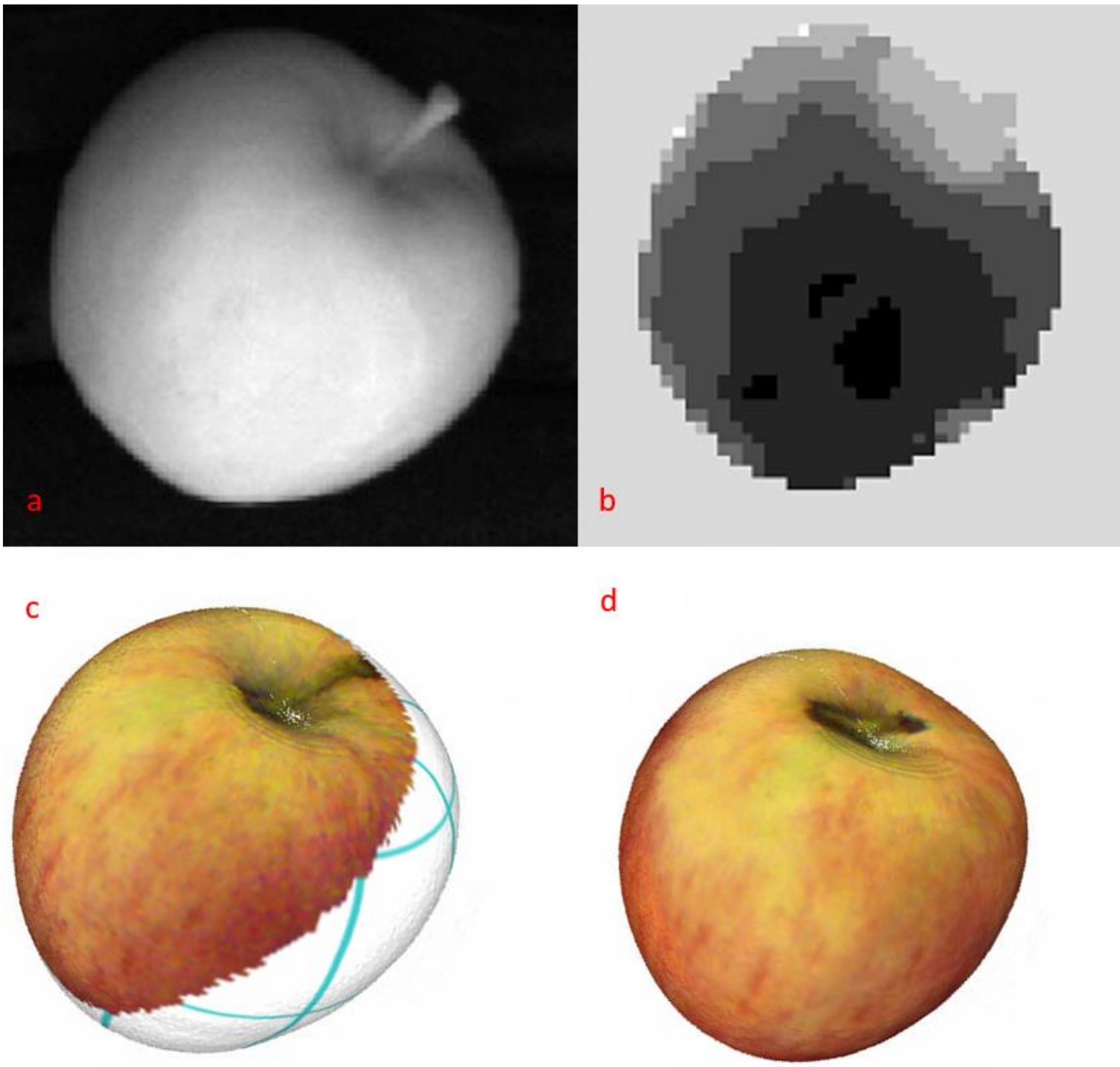

Figure 5.6 Steps for the whole fruit image reconstruction: infrared image (a), optical flow(b), single color image on merged 3D structure (c), stitched 3D texture(d).

The measurement of the motion of the fruits during the scan inspired a possible innovative type of CT scanner that I described in patent [92]. The idea is to include in the same measurement area an X-ray source and a sensor. As illustrated in Figure 5.7, the source and the sensors are stationary and the only moving parts are the fruits and the conveyor. The tomographic reconstruction in principle doesn’t require that the object has a specific trajectory with respect to the source-sensor pair. It is sufficient that the trajectory is known and some conditions are respected. For example an adapted FDK or iterative algorithm can be used for the purpose.

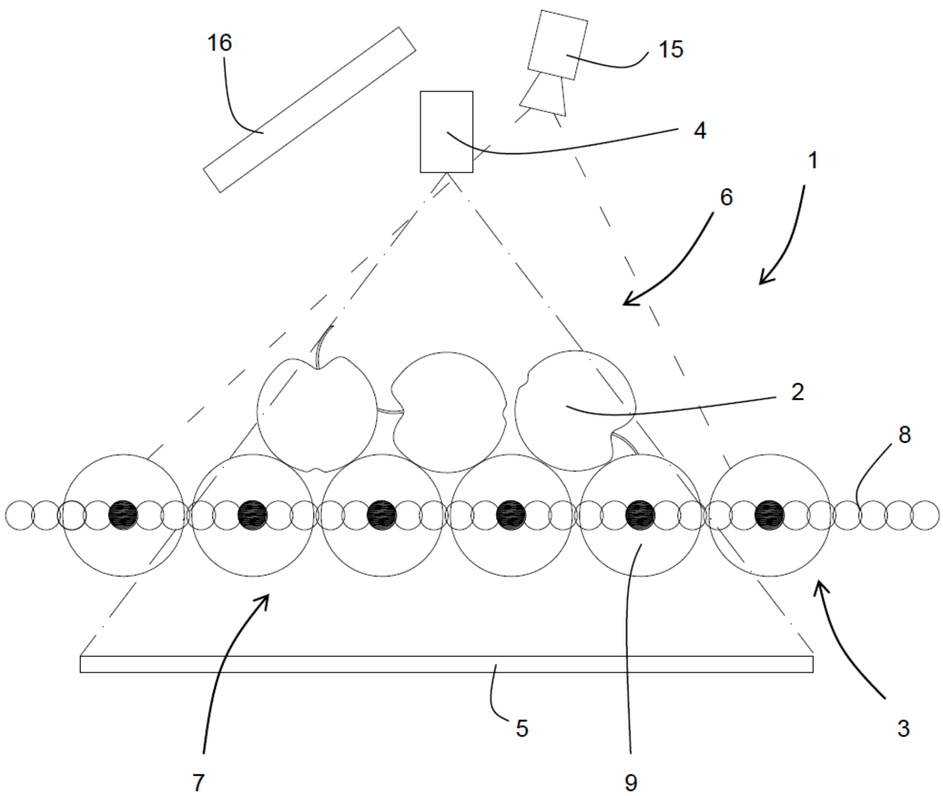

Figure 5.7 Sketch of the fruit CT scanner with uncontrolled rotation. The X-ray source (4) is mounted above the conveyor (8) and the X-ray sensor (5). The camera (15) measures the movement of the fruit (2) while it rotates on the rolls (3).

A similar application is also possible for the tomographic scans of a lot of other objects. In principle the usage of an external device for the measurement of the movement is not needed, as long as the same projections contain a lot of information. Algorithms for the detection of movement of the sample during the scan from the projections can be found in literature.

In Figure 5.8 a sawmill is shown where the boards are transported transversally. In many plants a device is installed that can rotate upside down the required boards for different purposes. In [93] I presented the idea of using the same device in order to realize a CT scanner with a static source-sensor pair and rotating object.

Figure 5.8 Device for the rotation of boards during the transversal transportation.

For other types of objects we are testing different transporting systems able to rotate the object to get a CT scan as shown in Figure 5.9 [94]. Magnetic transport systems have the advantage of allowing complex trajectories including rotation around the axis for CT scan acquisitions and passage into curved tunnels to simplify the shielding of the scattered radiation.

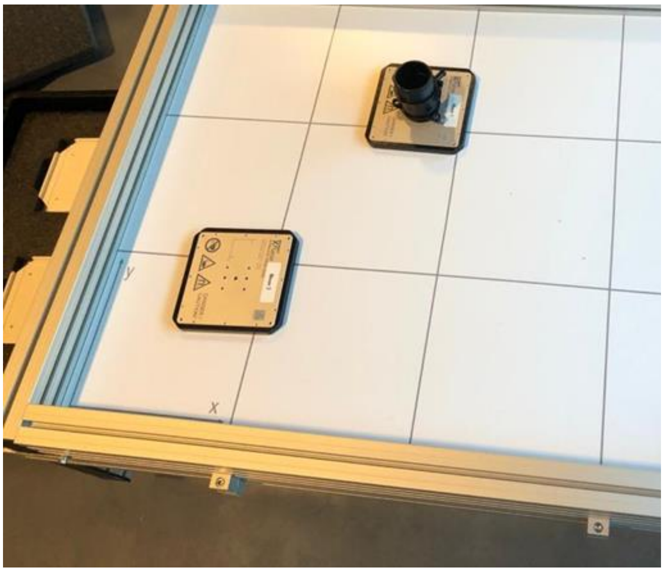

Figure 5.9Magnetic transportation for the samples to be CT scanned.

Conclusions

In recent decades, most production facilities have been equipped with automatic inspection systems for continuous monitoring of the production. Camera-based vision systems are probably the most common, but systems based on accelerometers, spectrometers, ultrasound and X-rays are increasingly present to allow as much information as possible to be obtained at all stages of the production process.

Among the technologies used for in-line inspection, tomography is practically absent due to the lack of systems capable of meeting the requirements of cost, speed and adaptability to working conditions. In this thesis I have outlined the development of the technologies required to introduce tomography into the wood and food industry.

I have also shown how tomography is able to acquire so much information about the raw material that can lead to an optimization of the entire production process in sawmills. As described in 3.10, computed tomography has proven to be an extremely powerful technology for the implementation of a sawmill in the spirit of the "smart factory", thanks to the possibility it offers to track and simulate all production steps from supplier to customer.

In order to make possible the introduction of tomography in other industries, I have also outlined some innovative ideas that may allow the production of CT scanners at a cost and performance level that can be used in an increasingly wide range of applications in the future.

Bibliography

[1] T. M. Buzug, *Computed tomography from photon statistics to modern cone-beam CT,* Soc Nuclear Med, 2009.

[2] GrandViewResearch, *Computed Tomography Market Size, Share & Trends Analysis Report 2019,* https://www.grandviewresearch.com/industry-analysis/computed-tomography-ct-market, [Online 14-march-2021].

[3] Siemens-healthineers, *Siemens SOMATOM Edge Plus brochure,* https://www.siemens-healthineers.com/it/computed-tomography/single-source-ct-scanner/somatom-edge-plus, [Online 15-february-2021].

[4] A. Mouton and T. P. Breckon, "A review of automated image understanding within 3D baggage computed tomography security screening," *Journal of X-ray science and technology,* vol. 23, p. 531–555, 2015.

[5] Rapiscan-systems, *Rapiscan 920CT brochure,* https://www.rapiscansystems.com/assets/files/BRBP-0001-920CT-181804_DIGITAL.pdf, [Online 15-February-2021].

[6] M. Wang, Industrial tomography: systems and applications, Elsevier, 2015.

[7] J. P. Kruth, M. Bartscher, S. Carmignato, R. Schmitt, L. De Chiffre and A. Weckenmann, "Computed tomography for dimensional metrology," *CIRP annals,* vol. 60, p. 821–842, 2011.

[8] A. Du Plessis, I. Yadroitsev, I. Yadroitsava and S. G. Le Roux, "X-ray microcomputed tomography in additive manufacturing: a review of the current technology and applications," *3D Printing and Additive Manufacturing*, vol. 5, p. 227–247, 2018.

[9] O. Brunke, J. Lübbehüsen, F. Hansen and F. F. Butz, "A new Concept for High-Speed atline and inlineCT for up to 100% Mass Production Process Control," in *16th International Congress of Metrology*, 2013.

[10] Waygate-technologies, *Phoenix Speedscan CT64 brochure,* https://dam.bakerhughesds.com/m/4ff8adcff6f6b733/original/Phoenix-Speedscan-CT64-EN-BHPD31346-072020-pdf.pdf, [Online 15-february-2021].

[11] S. Carmignato, W. Dewulf and R. Leach, Industrial X-ray computed tomography, Springer, 2018.

[12] H. Turbell, “Cone-beam reconstruction using filtered backprojection,” 2001.

[13] L. A. Feldkamp, L. C. Davis and J. W. Kress, “Practical cone-beam algorithm,” *Josa a,* vol. 1, p. 612–619, 1984.

[14] A. Katsevich, “Theoretically exact filtered backprojection-type inversion algorithm for spiral CT,” *SIAM Journal on Applied Mathematics,* vol. 62, p. 2012–2026, 2002.

[15] A. Katsevich, “An improved exact filtered backprojection algorithm for spiral computed tomography,” *Advances in Applied Mathematics,* vol. 32, p. 681–697, 2004.

[16] A. Katsevich and M. Kapralov, “Filtered backprojection inversion of the cone beam transform for a general class of curves,” *SIAM Journal on Applied Mathematics,* vol. 68, p. 334–353, 2007.

[17] M. Beister, D. Kolditz and W. A. Kalender, “Iterative reconstruction methods in X-ray CT,” *Physica medica,* vol. 28, p. 94–108, 2012.

[18] G. Wang, J. C. Ye and B. De Man, “Deep learning for tomographic image reconstruction,” *Nature Machine Intelligence,* vol. 2, p. 737–748, 2020.

[19] NIST, *X-Ray Mass Attenuation Coefficients for elemental media,* https://physics.nist.gov/PhysRefData/XrayMassCoef/tab3.html, [Online 15-february-2021].

[20] NIST, *X-Ray Mass Attenuation Coefficients for compounds and mixtures,* https://physics.nist.gov/PhysRefData/XrayMassCoef/tab4.html, [Online 15-february-2021].

[21] A. A. Okunade, “Parameters and computer software for the evaluation of mass attenuation and mass energy-absorption coefficients for body tissues and

substitutes," *Journal of Medical Physics/Association of Medical Physicists of India,* vol. 32, p. 124, 2007.

[22] O. M. H. Ahmed and Y. Song, "A Review of Common Beam Hardening Correction Methods for Industrial X-ray Computed Tomography," *Sains Malaysiana,* vol. 47, p. 1883–1890, 2018.

[23] E. Segal, W. A. Ellingson, Y. Segal and I. Zmora, "A linearization beam-hardening correction method for X-Ray computed tomographic imaging of structural ceramics," in *Review of Progress in Quantitative Nondestructive Evaluation,* Springer, 1987, p. 411–419.

[24] E.-P. Rührnschopf and K. Klingenbeck, "A general framework and review of scatter correction methods in x-ray cone-beam computerized tomography. Part 1: Scatter compensation approaches," *Medical physics,* vol. 38, p. 4296–4311, 2011.

[25] T. Niu and L. Zhu, "Overview of x-ray scatter in cone-beam computed tomography and its correction methods," *Current Medical Imaging,* vol. 6, p. 82–89, 2010.

[26] C. Kurz, F. Kamp, Y.-K. Park, C. Zöllner, S. Rit, D. Hansen, M. Podesta, G. C. Sharp, M. Li, M. Reiner and others, "Investigating deformable image registration and scatter correction for CBCT-based dose calculation in adaptive IMPT," *Medical physics,* vol. 43, p. 5635–5646, 2016.

[27] S. Kida, T. Nakamoto, M. Nakano, K. Nawa, A. Haga, J. Kotoku, H. Yamashita and K. Nakagawa, "Cone beam computed tomography image quality improvement using a deep convolutional neural network," *Cureus,* vol. 10, 2018.

[28] C. Kurz, M. Maspero, M. H. F. Savenije, G. Landry, F. Kamp, M. Pinto, M. Li, K. Parodi, C. Belka and C. A. T. Van den Berg, "CBCT correction using a cycle-consistent generative adversarial network and unpaired training to enable photon and proton dose calculation," *Physics in Medicine & Biology,* vol. 64, p. 225004, 2019.

[29] D. C. Hansen, G. Landry, F. Kamp, M. Li, C. Belka, K. Parodi and C. Kurz, "ScatterNet: a convolutional neural network for cone-beam CT intensity correction," *Medical physics,* vol. 45, p. 4916–4926, 2018.

[30] J. Maier, E. Eulig, T. Vöth, M. Knaup, J. Kuntz, S. Sawall and M. Kachelrieß, "Real-time scatter estimation for medical CT using the deep scatter estimation: Method and robustness analysis with respect to different anatomies, dose levels, tube voltages, and data truncation," *Medical physics,* vol. 46, p. 238–249, 2019.

[31] R. Grimmer and M. Kachelrieß, "Empirical binary tomography calibration (EBTC) for the precorrection of beam hardening and scatter for flat panel CT," *Medical physics,* vol. 38, p. 2233–2240, 2011.

[32] F. W. Taylor, F. G. Wagner, C. W. McMillin, I. L. Morgan and F. F. Hopkins, "Locating knots by industrial tomography-A feasibility study," *Forest Products Journal 34 (5): 42-46,* 1984.

[33] D. M. Benson-Cooper and R. L. Knowles, Computed tomographic scanning for the detection of defects within logs, Forest Research Institute, 1982.

[34] Q. Wei, B. Leblon and A. La Rocque, "On the use of X-ray computed tomography for determining wood properties: a review," *Canadian journal of forest research,* vol. 41, p. 2120–2140, 2011.

[35] S. Grundberg, A. Grönlund and U. Grönlund, The Swedish stem bank: a database for different silvicultural and wood properties, Luleå tekniska universitet, 1995.

[36] M. Pietikäinen, Detection of knots in logs using x-ray imaging, VTT, Technical Research Centre of Finland, 1996.

[37] S. Grundberg and A. Grönlund, "Simulated grading of logs with an x-ray log scanner-grading accuracy compared with manual grading," *Scandinavian Journal of Forest Research,* vol. 12, p. 70–76, 1997.

[38] J. Oja, B. Källsner and S. Grundberg, "Predicting the strength of sawn products by industrial X-ray scanning of Norway spruce saw logs," in *International Conference on Scanning Technology and Process Optimization for the Wood Industry: 04/11/2001-06/11/2001*, 2001.

[39] U. Nordmark, "Value recovery and production control in the forestry-wood chain using simulation technique," 2005.

[40] F. Brüchert, R. Baumgartner and U. H. Sauter, "Ring width detection for industrial purposes-use of CT and discrete scanning technology on fresh roundwood," in *Conference COST E,* 2008.

[41] F. Giudiceandrea, E. Ursella and E. Vicario, "A high speed CT scanner for the sawmill industry," in *Proceedings of the 17th international non destructive testing and evaluation of wood symposium*, 2011.

[42] E. Ursella, F. Giudiceandrea and M. Boschetti, "A Fast and Continuous CT scanner for the optimization of logs in a sawmill," in *8th Conference on Industrial Computed Tomography*, Wels,Austria, 2018.

[43] G. Lindholm, "Sågverksbranschens kostnads-och intäktsstruktur," *PhD Thesis. Sveriges lantbruksuniversitet.,* 2006.

[44] A. Katsevich, K. Taguchi and A. A. Zamyatin, "Formulation of four Katsevich algorithms in native geometry," *IEEE transactions on medical imaging,* vol. 25, p. 855–868, 2006.

[45] J. Oja, "A comparison between three different methods of measuring knot parameters in Picea abies," *Scandinavian Journal of Forest Research,* vol. 12, p. 311–315, 1997.

[46] F. Longuetaud, F. Mothe, B. Kerautret, A. Krähenbühl, L. Hory, J. M. Leban and I. Debled-Rennesson, "Automatic knot detection and measurements from X-ray CT images of wood: a review and validation of an improved algorithm on softwood samples," *Computers and Electronics in Agriculture,* vol. 85, p. 77–89, 2012.

[47] E. Johansson, D. Johansson, J. Skog and M. Fredriksson, "Automated knot detection for high speed computed tomography on Pinus sylvestris L. and Picea abies (L.) Karst. using ellipse fitting in concentric surfaces," *Computers and electronics in agriculture,* vol. 96, p. 238–245, 2013.

[48] H. Boukadida, F. Longuetaud, F. Colin, C. Freyburger, T. Constant, J. M. Leban and F. Mothe, "PithExtract: A robust algorithm for pith detection in computer tomography images of wood–Application to 125 logs from 17 tree species," *Computers and electronics in agriculture,* vol. 85, p. 90–98, 2012.

[49] S. Giovannini, D. Boschetto, E. Vicario, M. Cossi, M. Busatto, S. Ghidoni and E. Ursella, "Improving knot segmentation using Deep Learning

techniques," in *21st International Nondestructive Testing and Evaluation of Wood Symposium*, Freiburg, Baden-Württemberg, Germany, 2019.

[50] J.-P. Andreu and A. Rinnhofer, "Modeling of internal defects in logs for value optimization based on industrial CT scanning," in *Fifth International Conference on Image Processing and Scanning of Wood*, 2003.

[51] L. Breinig, F. Brüchert, R. Baumgartner and U. H. Sauter, "Measurement of knot width in CT images of Norway spruce (Picea abies [L.] Karst.)—evaluating the accuracy of an image analysis method," *Computers and electronics in agriculture,* vol. 85, p. 149–156, 2012.

[52] M. Fredriksson, J. Cool, I. Duchesne and D. Belley, "Knot detection in computed tomography images of partially dried jack pine (Pinus banksiana) and white spruce (Picea glauca) logs from a Nelder type plantation," *Canadian Journal of Forest Research,* vol. 47, p. 910–915, 2017.

[53] J. Cool, M. Fredriksson and S. Avramidis, "Knot detection in coarse resolution CT images of logs," in *23rd International Wood Machining Seminar, Warsaw, Poland, 28-31 May 2017*, 2017.

[54] J. Oja, "Evaluation of knot parameters measured automatically in CT-images of Norway spruce (Picea abies (L.) Karst.)," *Holz als Roh-und Werkstoff,* vol. 58, p. 375–379, 2000.

[55] A. Gasparetto, D. Ressi, F. Bergamasco, M. Pistellato, L. Cosmo, M. Boschetti, E. Ursella and A. Albarelli, "Cross-Dataset Data Augmentation for Convolutional Neural Networks Training . Int. Conf. on Pattern Recognition," in *Int. Conf. on Pattern Recognition, (ICPR2018)*, 2018.

[56] D. H. Ballard, "Generalizing the Hough transform to detect arbitrary shapes," *Pattern recognition,* vol. 13, p. 111–122, 1981.

[57] O. Ronneberger, P. Fischer and T. Brox, "U-net: Convolutional networks for biomedical image segmentation," in *International Conference on Medical image computing and computer-assisted intervention*, 2015.

[58] F. Giudiceandrea and E. Ursella, "Method for grading food products able to roll on their outer surface, such as certain fruits and vegetables". European Patent EP2261643B1, 2014.

[59] A. Uzunovic, T. Byrne, D.-Q. Yang and M. Gignac, Wood discolourations & their prevention: with an emphasis on bluestain, FPInnovations, 2008.

[60] R. G. Ballard, M. A. Walsh and W. E. Cole, "The penetration and growth of blue-stain fungi in the sapwood of lodgepole pine attacked by mountain pine beetle," *Canadian Journal of Botany,* vol. 62, p. 1724–1729, 1984.

[61] N. Macchioni, S. Palanti and P. Rozenberg, "Measurements of fungal wood decay on Scots pine and beech by means of X-ray microdensitometry," *Wood Science and Technology,* vol. 41, p. 417–426, 2007.

[62] E. Ursella and E. Vicario, "Method and apparatus for non-destructive inspection of a log to identify inner zones that are free of bluestain". European Patent EP3396374B1, 11 09 2019.

[63] J. T. Jennings and A. D. Austin, "Novel use of a micro-computed tomography scanner to trace larvae of wood boring insects," *Australian journal of entomology,* vol. 50, no. 2, pp. 160-163, 2011.

[64] K. Krügener, E.-M. Stübling, R. Jachim, B. Kietz, M. Koch and W. Viöl, "THz tomography for detecting damages on wood caused by insects," *Applied optics,* vol. 58, p. 6063–6066, 2019.

[65] P. Sepúlveda, D. E. Kline and J. Oja, "Prediction of fiber orientation in Norway spruce logs using an X-ray log scanner: A preliminary study," *Wood and fiber science,* vol. 35, p. 421–428, 2007.

[66] S. Skatter and B. Kucera, "The cause of the prevalent directions of the spiral grain patterns in conifers," *Trees,* vol. 12, p. 265–273, 1998.

[67] P. Gjerdrum, H. Säll and H. M. Storø, "Spiral grain in Norway spruce: constant change rate in grain angle in Scandinavian sawlogs," *Forestry,* vol. 75, p. 163–170, 2002.

[68] C. Guabello, "Deep learning for spiral grain classification in wood logs," 2021.

[69] J. M. Harris, Spiral grain and wave phenomena in wood formation, Springer Science & Business Media, 2012.

[70] A. Rais, E. Ursella, E. Vicario and F. Giudiceandrea, "The use of the first industrial X-ray CT scanner increases the lumber recovery value: case study on

visually strength-graded Douglas-fir timber," *Annals of Forest Science,* vol. 74, p. 28, 2017.

[71] A. Berglund, O. Broman, A. Grönlund and M. Fredriksson, "Improved log rotation using information from a computed tomography scanner," *Computers and electronics in agriculture,* vol. 90, p. 152–158, 2013.

[72] S. M. Stängle, F. Brüchert, A. Heikkila, T. Usenius, A. Usenius and U. H. Sauter, "Potentially increased sawmill yield from hardwoods using X-ray computed tomography for knot detection," *Annals of forest science,* vol. 72, p. 57–65, 2015.

[73] S. J. Chang and R. Gazo, "Measuring the effect of internal log defect scanning on the value of lumber produced," *Forest Products Journal,* vol. 59, p. 56–59, 2009.

[74] M. Fredriksson, "Log sawing position optimization using computed tomography scanning," *Wood Material Science & Engineering,* vol. 9, p. 110–119, 2014.

[75] L. Breinig, "CT log scanning for sawing optimization with regard to the aesthetic quality of wood," *University of Freiburg,* 2014.

[76] T. Pahlberg, O. Hagman and M. Thurley, "Recognition of boards using wood fingerprints based on a fusion of feature detection methods," *Computers and Electronics in Agriculture,* vol. 111, p. 164–173, 2015.

[77] J. Flodin, J. Oja and A. Grönlund, "Fingerprint traceability of sawn products using industrial measurement systems for x-ray log scanning and sawn timber surface scanning," *Forest products journal,* vol. 58, p. 100–105, 2008.

[78] E. Ursella, F. Giudiceandrea and M. Bacher, "Testa di lavorazione per macchina forestale". Italian requested Patent IT102020000025426, 27 10 2020.

[79] J. M. Leban, B. Kerfriden, F. Longuetaud, F. Mothe, E. Ursella, P. Jacquin , F. Giudiceandrea, P. Siat, R. Daquitaine, "La tomographie RX, des exemples d'innovations pour les scieries et pour la comptabilité du carbone forestier," in *8 ièmes journées du GDR 3544 Sciences du BoisAt: ENSTIB, Campus Bois, EPINAL,* 18-21 november 2019 Epinal Franve.

[80] L. Olofsson, C.-J. Möller, C. Wendel, J. Oja and O. Broman, “New possibilities with CT scanning in the forest value chain,” in *International Nondestructive Testing and Evaluation of Wood Symposium*, 2019.

[81] F. Giudiceandrea and E. Vicario, *Method for tracking a piece of wood,* European patent EP2410328, 2014.

[82] F. Giudiceandrea and E. Vicario, “Method for determining the rotation of a piece of wood with reference to a known lay-out”. European Patent EP 2410328 B1, 2014.

[83] E. Ursella, “Metodo e dispositivo per misurare una o più componenti di moto di un tronco”. Italian Patent IT10201700012024, 16 01 2020.

[84] E. Ursella, E. Vicario and M. Bacher, “Metodo per stabilire una corrispondenza a posteriori tra un pezzo di legno ed un tronco da cui il pezzo di legno era stato ottenuto”. Italy Patent IT102018000003506, 26 03 2020.

[85] F. Giudiceandrea, A. Katsevich and E. Ursella, “A reconstruction algorithm is a key enabling technology for a new ultrafast CT scanner,” *SIAM News*, vol. 49, p. 1–11, 2016.

[86] A. Giudiceandrea, E. Ursella and G. Zane, “Apparecchiatura tomografica industriale e metodo per controllare l’integrità di prodotti industriali”. italian requested Patent IT102020000019819, 07 08 2020.

[87] J. Peller, J. Ruizendaal, A. Mencarelli, E. Ursella, K. Winkler and H. Helsen, “Detection of Codling Moth Larvae in Apples using X-ray Computed Tomography,” *submitted to Post Harvest Biology and Technology*, 2021.

[88] K. Tschurtchentaler, E. Ursella and D. Bambi, “Metodo e apparato per la formatura di manufatti di polveri”. Italian Patent IT201600093579A1, 22 02 2019.

[89] E. Ursella, “Schermo per raggi X”. Italian Patent IT102018000004206, 20 04 2020.

[90] E. Ursella and M. Boschetti, “Tunnel CT Scanner”. European requested Patent EP3690429A1, 05 08 2020.

[91] M. Boschetti, S. Faccini, E. Ursella and G. Zane, “Method and apparatus for non-destructive inspection of fruits having an axis of rotational symmetry”. European Patent EP3521812B1, 15 07 2020.

[92] E. Ursella and F. Giudiceandrea, “Metodo e apparecchiatura per l'esecuzione di un esame tomografico di un oggetto”. Italian requested Patent IT 102019000019454, 21 10 2019.

[93] E. Ursella, “Apparecchiatura e metodo per eseguire una tomografia computerizzata di un oggetto che presenti forma allungata, in particolare tavole di legno”. Italian requested Patent IT102020000004246, 28 02 2020.

[94] T. Prenn and E. Ursella, “Tomografo computerizzato a tunnel e metodo per l’esecuzione di una tomografia computerizzata di un oggetto”. Italian requested Patent IT102020000014239, 15 06 2020.

[95] E. Ursella, “Metodo e dispositivo per misurare una o più componenti di moto di un tronco”. Italy Patent IT10201700012024, 16 01 2020.